UNIVERSIDADE
BEIRA INTERIOR

Design of a Long-Range Wing for the UAS30 Platform

Francisco Nuno Maurício Espíndola

Dissertação para obtenção do Grau de Mestre em
Engenharia Aeronáutica
(mestrado integrado)

(Versão final após defesa)

Orientador: Prof. Doutor Miguel Ângelo Rodrigues Silvestre
Co-orientador: Eng. José Renato Machado

Janeiro de 2021

Dedicated to my mother, Maria de Lurdes.

Acknowledgments

First of all, I want to express my thanks to my supervisor, Professor Miguel Ângelo Rodrigues Silvestre. He gave me all the tools necessary to carry out this work and helped me in all stages of it with total availability.

I would also like to thank my advisor at CEiiA, Engineer Renato Machado. I am grateful for the vote of confidence to carry out this work and the availability to help when necessary.

Many thanks to the CEiiA academy team and especially to Madalena Cunha for always making sure that nothing was missing during my integration with CEiiA.

I also want to thank my girlfriend, Francisca, and my friends who were the most delivered to me during this important stage in my life: Vasco, Divo, Bruno, Edgar, Otsugua, Carvalhais, Paulo, Oliveira, Zinho and Reis. A big hug to Top Down.

A big thank you to Desertuna who, in addition to giving me brothers for life, also gave me skills at a personal and associative level that will certainly help me throughout my personal and professional life.

Lastly, but more importantly, an eternal thanks to my family, but mainly to my parents, Maria de Lurdes and Esmeraldo, and my stepfather, Eduardo who always made sure that I never lacked anything and that I could focus only on my goals. I owe them everything.

Resumo

Com aplicações que podem ir desde a fotografia aérea à monitorização de campos agrícolas, passando pelo transporte de bens, permitindo manter os custos de operação e manutenção inferiores aos das aeronaves tripuladas, os veículos aéreos não tripulados (VANT) têm sido uma tecnologia com crescente interesse por parte de forças militares, empresas privadas ou até pessoas particulares. Um dos desafios no desenvolvimento deste tipo de plataformas é a capacidade para operar com bons desempenhos para diferentes tipos de missão. Neste sentido, o CEiiA desenvolveu a plataforma UAS30, que tem a capacidade de ser equipada com diferentes asas de acordo com os requisitos da missão a cumprir, de maneira a alargar a capacidade de operar com bons desempenhos, para vários tipos de missão.

Na presente dissertação, foi desenhada uma asa que visa conferir ao UAS30 bons desempenhos, especialmente no que toca ao alcance e à capacidade de voar a velocidades superiores àquelas a que esta plataforma atualmente opera. O processo de desenho iniciou-se com a determinação dos possíveis valores de corda e envergadura limitados pela cauda do UAS30. A interface XFOIL/XFLR5 foi utilizada, primeiramente para criar um novo perfil alar para as condições de baixo número de Reynolds do UAS30 e, de seguida, para executar análises de desempenho e estabilidade, o que permitiu a determinação dos restantes parâmetros de desenho da asa como a corda média aerodinâmica, a envergadura, o afilamento, torção, enflechamento, diedro e incidência, permitindo obter um compromisso entre desempenho e qualidades de voo. A utilização de flapes de cruzeiro, de modo a aumentar o desempenho da asa para condições *"off-design"* também foi avaliada. Na fase final do presente trabalho foi selecionada uma hélice apropriada e foi realizada uma estimativa de desempenho para permitir averiguar a melhoria de desempenho trazida pelo novo desenho da asa.

Como resultado, obteve-se uma asa que, não só, permite alcançar uma velocidade máxima bastante superior à alcançada pelo UAS30 com as asas originais, como permite voar com maior alcance e autonomia para toda a gama de velocidades. Concluiu-se ainda que, com a utilização de flapes de cruzeiro, não só se poderão atingir velocidades de perda inferiores às permitidas pela asa original do UAS30, bem como velocidades máximas superiores às conseguidas pelas novas asas sem flapes.

Palavras-chave

VANT, Desenvolvimento de Asas, Desenvolvimento de Perfis Alares, Baixo Número de Reynolds, Alcance, XFOIL, XFLR5.

Abstract

With applications ranging from aerial photography to agriculture fields monitoring, and passing through goods transportation, allowing operation and maintenance costs to be kept lower than those of manned aircraft, unmanned aerial vehicles (UAV) have been a technology with increasing interest from military forces, private companies or even individuals. One of the challenges in the development of this type of platform is the ability to operate with good performance for different types of mission. In this way, CEiiA developed the UAS30 platform, which has the ability to be equipped with different wings according to the requirements of the mission to be accomplished, in order to expand the ability to operate with good performances for various types of mission.

In this dissertation, a wing that aims to give UAS30 good performances, especially with regard to range and higher speeds than those which this platform currently operates, was designed. The design process started with the determination of the possible chord and span ranges limited by the existing tail of the UAS30. The XFOIL/XFLR5 tools were used, firstly to create a new airfoil for the Low Reynolds number conditions of the UAS30 and, then, to perform performance and stability analyses, which allowed the determination of the remaining design parameters such as the MAC, wingspan, taper ratio, washout, sweep, dihedral and incidence, allowing to obtain a compromise between performance and flight qualities. The use of cruise flaps in order to increase wing performance for off-design conditions was also evaluated. In the final phase of the present work, the selection of an adequate propeller and an estimate of theoretical performance to verify the performance improvement brought about by the new wing design were performed.

As a result, a wing was obtained that allows to reach a maximum speed much higher than that achieved with the original wings of the UAS30, allowing to fly with greater range and autonomy for the entire speed range. It was also concluded that, with the use of cruise flaps, not only stall speeds lower than those allowed by the original wing of the UAS30, but also maximum speeds higher than those achieved by the new wings without flaps, can also be achieved.

Keywords

UAV, Wing Design, Airfoil Design, Low Reynolds Number, Range, XFOIL, XFLR5.

Contents

List of Figures

List of Tables

Acronyms

AoA	Angle of Attack
CAD	Computer Aided Design
CEiiA	Center of Engineering and Product Development
CFD	Computational Fluid Dynamics
CG	Center of Gravity
DOF	Degree of Freedom
HALE	High-Altitude Long-Endurance
HLD	High Lift Devices
IED	Improvised Explosive Device
L.E	Leading Edge
MAC	Mean Aerodynamc Chord
MALE	Medium-Altitude Long-Endurance
MTOM	Maximum Takeoff Mass
MTOW	Maximum Takeoff Weight
NACA	National Advisory Committee for Aeronautics
NBC	Nuclear, Biological, Chemical
RPM	Revolutions per Minute
SFC	Specific Fuel Consumption
TEHLD	Trailing Edge High-Lift Devices
UAV	Unmanned Aerial Vehicle
US	United States
UAS	Unmanned Aerial System
UBI	Universidade da Beira Interior
VBA	Visual Basic
WSM	Weighted Scores Method

Nomenclature

Roman Letters

$\%_{ref}$	Chord Percentage Reference for Null Sweep
A	Aspect Ratio
A_t	Tail Aspect Ratio
b	Wingspan
b_t	Tail Span
b_{wheel}	Wheel Width
c	Chord
C	Specific Fuel Consumption
$\bar{c}$	Mean Aerodynamic Chord
$\bar{c}_t$	Tail Mean Aerodynamic Chord
C_D	Drag Coefficient
C_d	Airfoil Drag Coefficient
C_{D_0}	Parasite Drag Coefficient
$(C_{D_0})_B$	Body Parasite Drag Coefficient
C_{D_b}	Base Drag Coefficient
$C_{D_{f_b}}$	Body Parasite Drag Coefficient Exclusive of the Base
$C_{D_{G_{C_L=0}}}$	Landing Gear Parasite Drag Coefficient Based on S_G
$C_{d_{min}}$	Airfoil Minimum Drag Coefficient
C_{f_B}	Body Turbulent Flat Plate Sking Friction Coefficient
c_{new}	New Chord
$c_{original}$	Original Chord
c_r	Root Chord
c_{spar}	Spar Section Wing Chord
c_t	Tip Chord
C_L	Lift Coefficient
C_l	Airfoil Lift Coefficient
C_L/C_D	Lift to Drag Ratio
$(C_L/C_D)_{max}$	Maximum Finesse Ratio
C_l/C_d	Airfoil Finesse Ratio
$(C_l/C_d)_{max}$	Airfoil Maximum Finesse Ratio
C_{L_0}	Null Angle of Attack Lift Coefficient
C_{l_α}	C_l vs α slope
$C_{L_{design}}$	Design Lift Coefficient
$C_{l_{min}}$	Airfoil Lift Coefficient for Minimum Drag Coefficient
C_{l_2}/C_{l_1}	Airfoil Overall Performance Ratio
$C_{l_{max}}$	Airfoil Maximum Lift Coefficient

$C_{L_{max}}$	Maximum Lift Coefficient
C_m	Pitching Moment Coefficient
D	Drag
d	Body Equivalent Diameter
D_{wheel}	Wheel Diameter
$\frac{d_b}{d}$	Base Diameter to Equivalent Diameter Ratio
$\frac{dC_l}{d\alpha}$	C_l vs α slope
E	Endurance
g	Gravitational Acceleration
i_w	Wing Incidence
K	Induced Drag Coefficient
L	Lift
L/D	Lift to Drag Ratio
l_b	Body Length
l_H	Horizontal Tail Projected Lever Arm
l_V	Vertical Tail Projected Lever Arm
M	Pitching Moment
m	Mass
p	Roll Rate
$P_{max_{SL}}$	Maximum Engine Shaft Power at Sea Level
P_a	Power Available
P_o	Power Output
P_r	Power Required
q	Pitch Rate
r	Yaw Rate
R	Range
R_{WB}	Wing-Body Correlation Factor
Re	Reynolds Number
$Re\sqrt{C_L}$	Reynolds Number for Fixed Lift
RC	Rate of Climb
RC_{max}	Maximum Rate of Climb
S	Wing Area
S_{ref}	Wing Area
S_B	Body Maximum Frontal Area
$(S_S)_e$	Body Wetted Area
S_t	Tail Area
S_{Vtail}	V-Tail Area
S_G	Reference Area Used for Landing Gears
S_H	Horizontal Tail Projected Area
SM	Static Margin
S_V	Vertical Tail Projected Area
t	Time

t	Thickness
t/c	Airfoil Relative Thickness
$(t/c)_{new}$	New Airfoil Relative Thickness
$(t/c)_{original}$	Original Airfoil Relative Thickness
T_a	Thrust Available
T_r	Thrust Required
u	Fluctuation in Horizontal Speed
U_∞	Free-stream Velocity
v	Fluctuation in Lateral Speed
V	Speed
V_{cruise}	Cruise Speed
V_{max}	Maximum Speed
V_{stall}	Stall Speed
$V_{RC_{max}}$	Maximum Rate of Climb Speed
$V_{\gamma_{max}}$	Maximum Climb Angle Speed
$V_{R_{max}}$	Maximum Range Speed
$\bar{V}_H$	Tail Projected Horizontal Volume Coefficient
$\bar{V}_V$	Tail Projected Vertical Volume Coefficient
w	Fluctuation in Vertical Speed
W	Weight
W_0	Takeoff Weight
W_1	Weight Except Fuel
W_f	Fuel Weight
x_{cg}	Center of Gravity Horizontal Position
x_{np}	Neutral Point Horizontal Position
$x_{L.Eoffset}$	Leading Edge Horizontal Offset from the Origin
$\bar{x}_{cg}$	Center of Gravity Position in Percentage of MAC
$\bar{x}_{np}$	Neutral Point Position in Percentage of MAC
y_{boom}	Tail Boom y Position

Greek Letters

α	Angle of Attack
α_0	Zero Lift Angle of Attack
α_s	Stall Angle of Attack
α_t	Tip Washout Angle
γ	Climb Angle
γ_{max}	Maximum Climb Angle
Γ	Dihedral Angle
δ	Flap Deflection Angle
η_p	Propeller Efficiency
θ	Pitch Angle
λ	Taper Ratio
λ_t	Tail Taper Ratio
Λ	Sweep Angle
$\Lambda_{c/4}$	Sweep Angle About the Quarter Chord
$\Lambda_{c/4_t}$	Tail Sweep Angle About the Quarter Chord
Λ_t	Tail Sweep Angle
μ	Fluid Viscosity
ξ	Damping Ratio
π	Pi Constant
ρ	Fluid Density
ρ_0	Fluid Density at Sea Level
σ_1	Damping Constant
ϕ	Roll Angle
ω_1	Mode Undamped Natural Circular Frequency
ω_n	Mode Natural Frequency

Chapter 1

Introduction

1.1 Motivation

1.1.1 UAVs

Since the first guidance and navigation rockets, researchers' interest in unmanned aerial vehicles has increased exponentially in recent years.

Historically, UAVs have evolved largely in the military. This is because they have always been seen as tools capable of replacing humans on missions that would bring too much risk to them. Such missions include reconnaissance and surveillance on enemy ground.

Nowadays, UAVs are starting to be sought after for civilian applications, allowing for example the capture of aerial images by any ordinary person, something that a few years ago would have been virtually impossible. In addition, UAVs have started to be used to perform tasks such as surveillance of agricultural fields or electrical networks, where these tasks performed by manned aircraft can jeopardize the safety of crew members due to low operating altitudes.

In Portugal, wildfires are a problem that affects citizens' lives every year, causing deaths and stealing property from people. Investment in forest surveillance UAVs, capable of detecting wildfires in early stages, has been heralded as a promising prevention tactic, highlighting the general importance of UAVs [1]. Also, in relation to the recent COVID-19 pandemic, drones are being used to spray disinfectant on some surfaces, facilitating the work of disinfecting public spaces, necessary to contain the pandemic [2]. In addition, they are also being used to monitor public spaces in order to avoid gathering of people [3].

That said, the possibility of helping in the development of a product that can perform missions that can save human lives, as well as contributing to the technological development of this type of devices, even more so within a reference engineering center in Portugal, gave the motto for carrying out this work.

1.1.2 CEiiA

CEiiA is a Portuguese center of engineering and product development that designs, implements and operates innovative products and systems with worldwide partners in the automotive, mobility, aeronautics, naval and space industries.

Figure 1.1: CEiiA headquarters, Matosinhos.

Regarding aeronautics, the activity of CEiiA is centered in product development and structural testing. They work in collaboration with various international companies such as Embraer, Leonardo, Finmeccanica and Daher. In addition to these partnerships, CEiiA also develops its own products, such as UAS30 or the autonomous submarine vehicle, the Medusa Deep Sea.

CEiiA is a key partner in the entire development cycle of the KC-390, the largest aircraft ever produced by Embraer and considered the first big aeronautic engineering program in Portugal. The participation of CEiiA in this program is focused on the elevator, central fuselage and sponson of the aircraft. Regarding these structures, the activities performed by CEiiA are in design, stress analysis, weight reduction, manufacturing support, among others. CEiiA's participation in this program has more than 450 thousand engineering hours.

This company has also participated in different phases of development of six Leonardo helicopters including design, stress analysis and weight reduction.

Recently it has been announced that CEiiA, in partner with Desaer, will develop a new light transportation aircraft, ATL-100. This aircraft will be the first complete aeronautical program that includes the development, industrialization and operation of the aircraft to be made in Portugal [4].

Among other development projects, their recent product Atena stands out. Atena is a mechanical ventilator developed in record time of 45 days as a response to the lack of

Figure 1.2: Embraer KC-390.

such devices, which are very necessary in the fight against the recent Covid-19 pandemic in hospitals.

1.2 UAS30 Characterization

The UAS30 is a unmanned aerial system developed by CEiiA that is operated together with the Portuguese Air Force. It was designed to perform in the fields of agriculture, environment monitoring, territory inspection, sea operation, electric lines surveillance among others.

This platform stands out by being able to achieve a minimum operating speed of 13.89 m/s, really low when compared to similar devices, allowing the UAS30 to be especially good at low speed missions such as image capturing.

Figure 1.3: UAS30 UAV [5].

In terms of propulsion system, the UAS30 is equipped with a piston propeller engine installed in a pusher configuration. In this case, this type of engine configuration allows the airplane to fly in undisturbed air improving its aerodynamic efficiency.

The vehicle also uses an inverted V-tail configuration connected to the wings through two tail booms. This tail configuration allows the reduction of the interference drag and it reduces the tendency to spin [6]. In Figure 1.4 the V-Tail and respective booms can be observed.

Figure 1.4: UAS30 UAV in flight view [5].

The available information about the performance of the UAS30 is summarized in Table 1.1, while the wing geometrical parameters can be seen in Table 1.2. The data concerning the tail of the UAS30 can also be consulted in Table 1.3. Note that the dimensional parameters presented were obtained from the UAS30 original XFLR5 [7] model, while the performance parameters are the ones published by CEiiA.

Table 1.1: UAS30 available performance parameters [5].

Parameter	**Value**
MTOM [kg]	35
E [h]	5
V_{cruise} [m/s]	20
Minimum operating speed [m/s]	13.89
V_{stall} [m/s]	10.5
RC [m/s]	12.1
Turn radius [m]	30
Minimum take off distance [m]	30

Table 1.2: UAS30 wings dimensional parameters.

Parameter	Value
b [m]	4.29
$\bar{c}$ [m]	0.55
S [m]	2.281
A	8.07
Wing Incidence [deg]	1.893
Tip Washout [deg]	-3
λ	0.512
$\Lambda_{c/4}$ [deg]	-0.01
Γ [deg]	1.9

Table 1.3: UAS30 tail dimensional parameters.

Parameter	Value
b_t [m]	1.99
$\bar{c}_t$ [m]	0.33
S_t [m]	0.66
A_t	6.04
Tail Incidence [deg]	0
Tip Washout [deg]	0
λ_t	1
$\Lambda_{c/4_t}$ [deg]	0
Γ_t [deg]	-38.7

1.3 Objectives

The main objective of this thesis is the design of a new wing for the UAS30 that could achieve longer range at higher speed than the UAS30 currently operates. As stated in Section 1.2, the UAS30 shows an unusual ability to operate at very low speeds. This is very useful for missions like image capture, but makes it impossible to carry out missions that require higher cruising speeds.

Since the UAS30 is developed to be a very versatile platform, CEiiA made it modular so that different wings can be used depending on the required mission conditions. This allows the efficient execution of different types of missions, as long as the different wings are developed taking into account the type of mission for which they will be used.

The wing to be designed in this work must provide higher ranges at higher speeds than the wing currently equipped on the UAS30. This can be obtained by ensuring that the lift to drag ratio (C_L/C_D) provided by the new wing is greater for higher speeds than the provided by the original UAS30 wing. This relation between the lift to drag ratio and range can be understood with the help of Section 2.1.6.

During the execution of the proposed work, it is also important to understand the steps involved in the design of a wing, as well as to become familiar with the tools used to achieve the objectives.

1.4 Requirements

The requirements imposed by CEiiA for the new wing design solution were as follows:

1. The new wing must be designed taking into account the original fuselage and tail of the UAS30;
2. The wing's skin will be a sandwich composite, made of carbon and glass fibers, airex foam core, liquid resin and a gel coating. It is a low density composite which offers good strength at low weight;
3. The new wing must be designed to be compatible with the original UAS30 spar. For that, the wing thickness must be equal or higher than the original wing in the sections where the spar is located.
4. The new wing should enable longer ranges at higher speeds than the original UAS30 wing.

1.5 Thesis Outline

This thesis is divided in five chapters. The description of each chapter is mapped as follows:

Chapter 1 introduces the theme of the study and the motivation that led to its choice. In this chapter, the requirements and objectives of the study are also defined. A characterization of the UAS30 is made and a brief presentation of CEiiA, the company who developed it, is also given.

Chapter 2 provides a literature review of the topics covered in the work. This includes the theoretical foundations needed to understand the steps of the work and a contextualization of the UAS30 in the framework of equivalent vehicles.

Chapter 3 presents the methodology adopted to achieve the proposed objectives, as well as a presentation of the tools utilized throughout the work.

Chapter 4 contains the results obtained after carrying out the referred methodology. It also contains the discussion related to those results that support the conclusions and the adopted new wing design solution.

Chapter 5 presents the conclusions of the work, as well as the achievements obtained. Open topics and future work recommendations are also provided.

Chapter 2

Literature Review

2.1 Theoretical Foundations

2.1.1 Airfoils

The airfoil is the second most important parameter of a wing, right after the planform area [8]. Its selection, which occurs in the conceptual phase of design, has to take in account various factors such as operation conditions and mission profile. It influences performance features such as take off and landing distances, cruise speed, stall speed and handling qualities.

All in all, an airfoil is a two-dimensional representation of a wing's cross section. It is this two-dimensional shape that mostly influences the behavior of the flow responsible for generating lift.

When the flow approaches the leading edge (see Subsection 2.1.1.1, Figure 2.1) of the airfoil, it splits up between its upper and lower surfaces. Due to the positive curvature of the upper surface, a pressure decrease takes place. On the lower surface the opposite happens, this causes the static pressure on the upper surface to be lower than the ambient pressure generating a suction force there and, on the lower surface to be higher than the ambient pressure creating there an over pressure. This difference of pressures is what generates lift. This force has greater intensity the higher the angle of the chord line relative to the freestream (called angle of attack, α) until a critical angle, α_s, where the upper surface flow separates, greatly disturbing the flow conditions. A symmetrical airfoil, which has no camber, when exposed to a flow with $\alpha = 0$ produces no lift [9].

The airfoil should behave according to the specific mission requirements of a given aircraft. Therefore, there is no ultimate airfoil that perfectly suits all possible operation conditions. For this reason, the selection of an airfoil should be performed having all the specific mission requirements of the in-design aircraft. There are two possible approaches to selecting an airfoil for a given aircraft:

- Comparing the features of different airfoils obtained in multiple existing airfoil data bases;
- Designing an airfoil specially for a given application.

Although the first approach is usually less time consuming and requires less experience from the aircraft designer, the airfoil designing approach can provide better results since the airfoil is being specifically designed to work under the desired conditions.

2.1.1.1 Geometrical Parameters

The geometrical parameters can be seen in Figure 2.1. Reference [9] gives the following definitions to each parameter:

- The **leading edge** is the most forward extreme point of the airfoil which is first subject to the freestream if α = 0;
- The **trailing edge** is the extreme point of the airfoil where the flow leaves it;
- The **chord** is the straight line that connects the leading edge to the trailing edge;
- The **mean camber line** is the mean line between the upper and lower surfaces;
- The **maximum camber** is the maximum deviation of the camber line with respect to the chord line;
- The **thickness** is the maximum distance between the upper and lower surfaces. Usually, the airfoil thickness and camber (maximum) are represented in chord percentage.

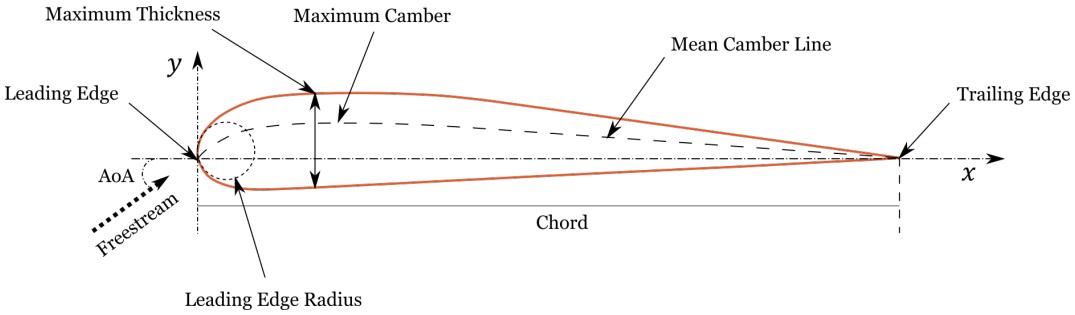

Figure 2.1: Airfoil geometrical parameters.

2.1.1.2 Airfoil Aerodynamic Coefficients

The aerodynamic coefficients used to define the aerodynamic behavior of an airfoil are its lift coefficient, C_l, drag coefficient, C_d, and pitching moment coefficient, C_m. For any airfoil, the previous parameters are functions of the angle of attack, α, Reynolds, Re, and Mach number, M_∞ (although for M_∞ > 0,3, the influence of Mach is negligible). These coefficients can be obtained using Equations 2.1, 2.2 and 2.3 and they relate the aerodynamic forces (lift, drag, pitching moment) with the dynamic pressure $\left(\frac{1}{2}\,\rho\,U_\infty\right)$ and the chord of a given airfoil.

$$C_l = \frac{l}{1/2\,\rho\,U_\infty^2\,c} \quad (2.1)$$

$$C_d = \frac{d}{1/2\,\rho\,U_\infty^2\,c} \quad (2.2)$$

$$C_m = \frac{m}{1/2\,\rho\,U_\infty^2\,c} \quad (2.3)$$

2.1.1.3 Thickness and camber

The thickness ratio is an important parameter to have in mind when selecting an airfoil because it has major impact on the weight of the wing's structure. The higher the thickness of the wing section, the lighter the structure can be. Therefore, the selection of the airfoil should be a compromise between good aerodynamic behavior and thickness ratio values that do not compromise the structural weight of the wing. The thickness also plays its part in the aerodynamic characteristics of the airfoil [10]. In Figure 2.2 it is possible to notice small gains in lift coefficient with the increase in thickness, but also unwanted gains in pitching moment coefficient, drag coefficient and, hence, loss of aerodynamic efficiency.

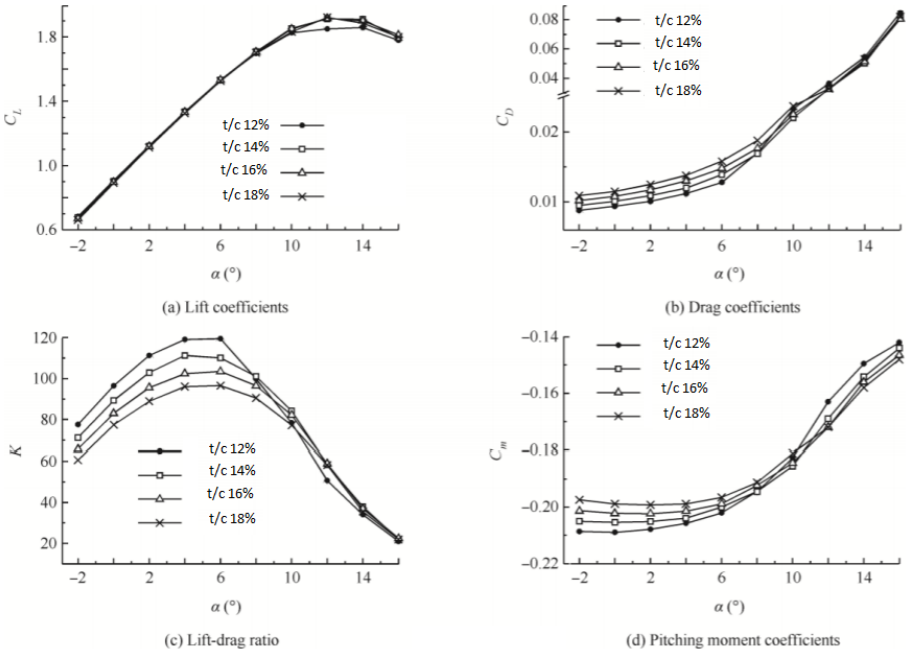

Figure 2.2: Thickness ratio influence on the aerodynamics of an airfoil ([10]).

Related to the thickness ratio is the leading edge radius. If the leading edge radius value is large, the flow can stay attached at higher angles of attack, providing superior stall angles (see Figure 2.2), which gives more lift for take off, landing or the capacity to carry high

payloads for a prescribed stall speed. However, a thick leading edge also produces more drag and pitching moment, which is detrimental for the overall performance of the airfoil [6, 10].

The camber of an airfoil gives it the capacity to generate lift at $\alpha = 0$ and also allows it to achieve higher values of maximum lift coefficient [11], although, it can also be responsible for increasing unwanted effects such as drag and pitching moment coefficients. Airfoils designed to operate in low speed or to carry heavy payloads typically have higher camber values.

2.1.1.4 Reynolds Number

To study any flow, such as the flow on an airfoil, it is necessary to know its nature and the behavior it will present under certain conditions. Flows can be laminar, having an organized and linear behavior, or turbulent, distinguished by having a really non linear behavior being very hard to predict. What helps to understand the tendency that a certain flow has to be laminar or turbulent is its Reynolds number: a non dimensional parameter that relates the order of magnitude of inertial forces with the viscous ones in a flow. By Equation 2.4 it is possible to conclude that for different freestream speeds and chord lengths (for airfoils) Reynolds numbers may vary a lot. Typically, a flow tends to be laminar in a smooth wall without adverse pressure gradient until a Reynolds of near 10^6. That is when small disturbances affecting it start to be sufficient to turn it into turbulent [9].

$$Re = \frac{\rho U_\infty c}{\mu} \quad (2.4)$$

When selecting an airfoil for any aircraft it is really of prime importance to know the Reynolds number of operation of the given wing. This parameter has a huge influence on the performance of an airfoil because it gives information about the nature of the flow, and it influences where the flow separation on the airfoil occurs and the amount of parasite drag coefficient it will produce. For these reasons, an airfoil designed to operate at a certain Re range, most certainly will not show a good performance on an aircraft operating outside of that range.

Different types of aircraft operate at different Re values. In Figure 2.3 it is possible to distinguish the different types of flying entities with respect to their operation Reynolds number. In the upper Reynolds regime (high Reynolds), sensibly above $Re = 10^6$, it is where the most efficient vehicles, such as transport airplanes, operate (see Figure 2.3). This regime provides good performance to aircraft due to the boundary layer transition from laminar to turbulent without flow separation and reattachment, which avoids a drag coefficient increase due to laminar separation bubbles [12].

In case of Low Reynolds operating aircraft such as small UAVs, model sailplanes, or other aircraft with relatively small wing chords and low speeds operation, the conditions are quite the opposite. In this regime of Reynolds (between 10^4 and 10^6) there is the phenomenon of laminar separation of the boundary layer close to the trailing edge caused by the inability of the laminar boundary layer to withstand intense adverse pressure gradients. This happens due to the dominance of diffuse effects on laminar flows. When the separation occurs, at moderately Low Reynolds, the separated flow can become turbulent, recovering from the separation and reattaching [13]. This reattachment creates a laminar circulation bubble, which although is effect of a phenomenon that prevents turbulent separation, is also responsible to produce negative effects such as higher drag coefficients. Hence, it is possible to state that the principal cause of lack of performance on airfoils at low Reynolds operation comparing with high Reynolds operation is the increase on drag due to the laminar separation bubbles [12].

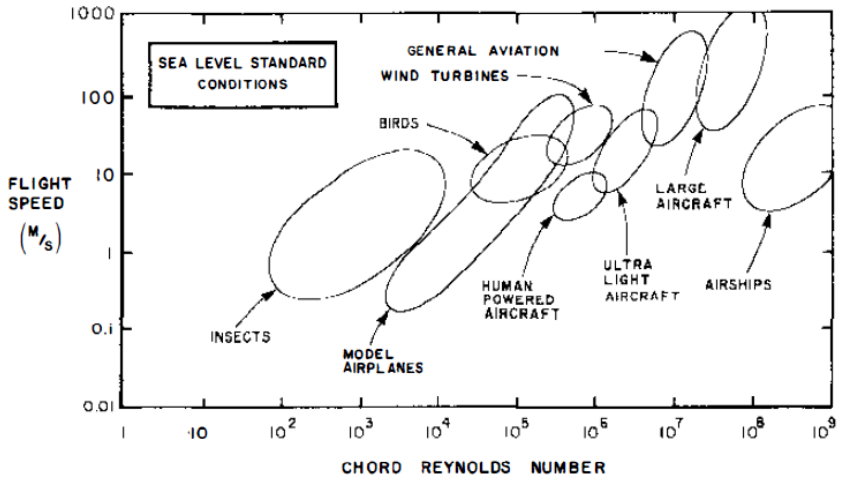

Figure 2.3: Flight Reynolds-number spectrum [13].

2.1.1.5 Airfoil Analysis

Airfoils behavior can be predicted by numerical methods. Presently there are computer codes capable of easily performing quite accurately subsonic airfoil analysis, such as XFOIL [14], developed by Prof. Mark Drela.

When analyzing an airfoil, there are four important graphs to look at, being those the lift coefficient *vs* angle of attack, the aerodynamic efficiency (C_l/C_d) *vs* lift coefficient, the pitching moment coefficient *vs* AoA and the lift coefficient *vs* drag coefficient [8].

In Figure 2.4 it is possible to observe the characteristic graph that shows the relationship between the lift coefficient and the angle of attack of an airfoil, along with some highlighted features that are necessary to understand when observing the graph. The $C_{l_{max}}$ point corresponds to the maximum lift coefficient of the airfoil. This is an important parameter because it allows the designer to understand if the airfoil will achieve lift coeffi-

cient values that may provide safe stall speeds or capacity to carry heavy loads for a given wing area. The higher the value of $C_{l_{max}}$ of the airfoil, the smaller the wings have to be in order to achieve certain stall speeds or take off weights. Directly related to $C_{l_{max}}$ is the α_s parameter. This is called stall angle and corresponds to the angle of attack at which the maximum lift of the airfoil will occur. After this point, increasing the angle of attack will cause the airfoil to lose lift and stall. It can be preferable to have higher values of this parameter since it will confer the ability of flying at a higher range of angles of attack without causing wing stall and possibly entering a spin.

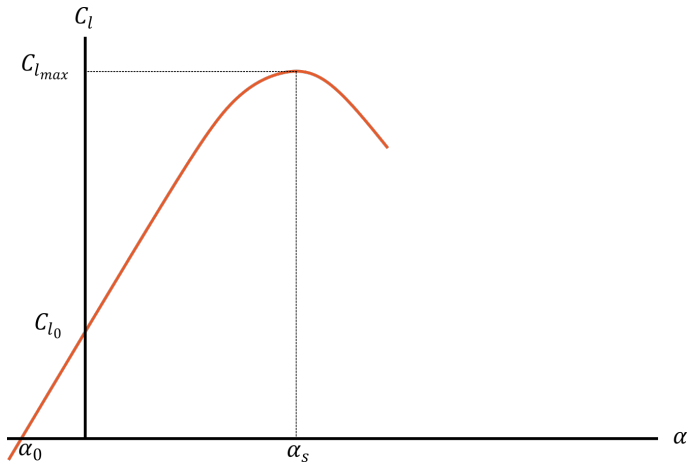

Figure 2.4: Airfoil lift coefficient variation with the angle of attack

Other parameters that can be seen in the graph of C_l *vs* α are the zero lift angle of attack, α_0 , that corresponds to the angle of attack at which the airfoil starts to generate lift and the zero-alpha lift coefficient, C_{l_0} , which allows the designer to know what is the lift coefficient for zero angle of attack. This value is zero for symmetrical airfoils. The lift curve slope, C_{l_α} or $\frac{dC_l}{d\alpha}$, is expressed in rad^{-1} or deg^{-1}, and it is an indicator of how quickly lift coefficient increases with angle of attack. A high value of this parameter can be more desirable, since it means that with small changes in the angle of attack, larger changes of lift coefficient values can be achieved. Another important feature to have in mind when analyzing this graph is the shape of the curve after stall. Stall can be gradual or abrupt (see Figure 2.5). A gradual stall is defined by a small slope after stall, while an abrupt stall is characterized by a really tilted curve. A gradual stall is typically pursued, since it allows the aircraft an easier recovery from it. An abrupt stall of the airfoil can be fixed with wing geometry such as higher taper ratio (wing tip to root chord ratio) or washout.

In the graph that relates the lift coefficient *vs* drag coefficient, also known as drag polar, more features with major importance for the designer are shown in Figure 2.6. The point labeled as $C_{d_{min}}$ corresponds to the minimum drag coefficient of the airfoil. Since drag is an undesirable effect for the performance of an airfoil, the lower this value the better for higher speed operation and fuel costs. The lift coefficient corresponding to $C_{d_{min}}$ is identified as $C_{l_{min}}$. Another feature of interest is the $(C_l/C_d)_{max}$, given by the intersection of a straight line passing through the origin and tangent to the C_l *vs* C_d curve, that shows the point of maximum aerodynamic efficiency. The drag polar is usually simplified as a

parabolic shape, although when an airfoil is designed to maintain laminar flow, the drag polar can exhibit what is called a laminar bucket due to drag coefficient reduction near the design lift coefficient region. Figure 2.7 depicts the two representations.

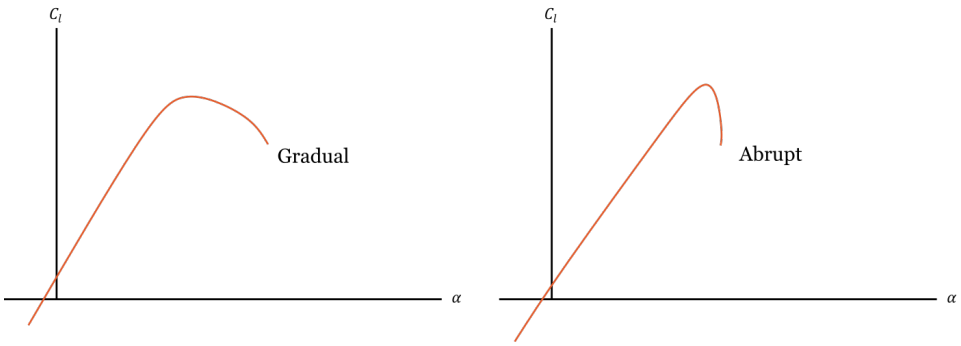

Figure 2.5: Gradual and abrupt stall comparison.

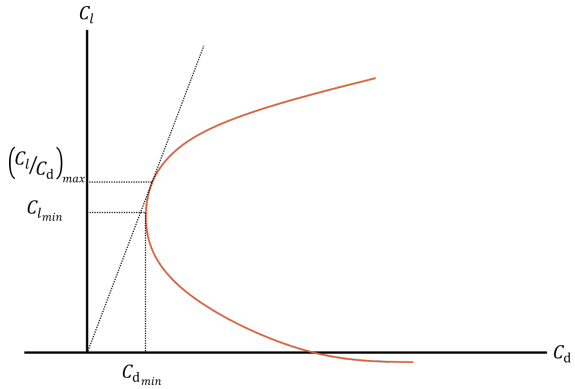

Figure 2.6: Airfoil drag coefficient variation with the lift coefficient.

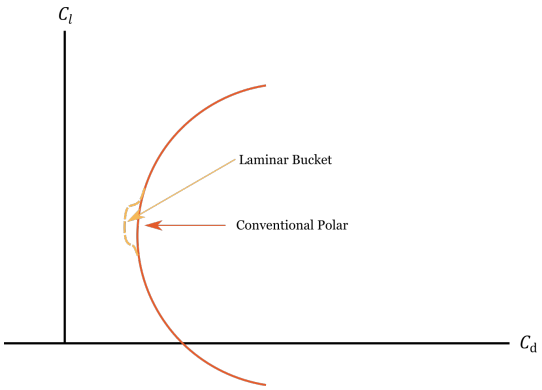

Figure 2.7: Laminar bucket on the drag polar (adapted from [6]).

The pitching moment *vs* angle of attack graph shows the designer how the airfoil, by itself, can stabilize the airplane when hit by some gust. Typically, a negative slope for this curve is pursued since it means that for positive angles of attack the pitching moment produced by the airfoil counteracts the gust downwards while for negative angles of attack the produced pitching moment will act upwards, guaranteeing stabilization for both situations.

In addition to that, the magnitude of the C_m values should be as low as possible, since higher values usually mean larger tail coefficients. In Figure 2.8 a typical pitching moment *vs* angle of attack curve for a subsonic airfoil is represented .

The graph that contains the aerodynamic efficiency curve in terms of the lift coefficient can be seen in Figure 2.9. This graph can be considered the most important to take into account, since it shows the designer how well the airfoil behaves for the whole range of lift coefficients. Airfoils that exhibit higher values of C_l/C_d are always preferable, since this parameter is the main indicator of performance. The highlight points for this graph are the $(C_l/C_d)_{max}$ and its corresponding lift coefficient. It is important to have an high $(C_l/C_d)_{max}$ value near the region of the design lift coefficient, $C_{L_{design}}$, since for a propeller driven aircraft, for the maximum aerodynamic efficiency value, the range will also be maximum [15]. Nevertheless, it is still preferable, for most cases, to have a wider envelope of moderate to high C_l/C_d values than to have a really high $(C_l/C_d)_{max}$ value over a reduced range of lift coefficients, neglecting the C_l values outside that range thus limiting the good performance of the airplane to a very specific condition.

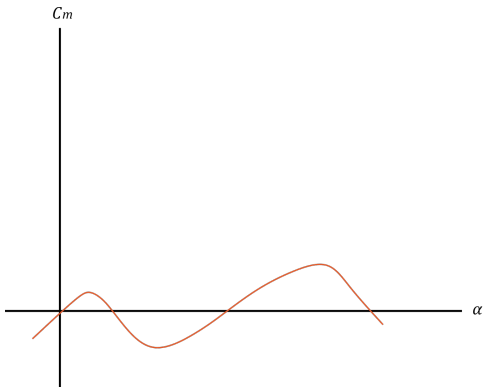

Figure 2.8: Airfoil pitching moment coefficient variation with the angle of attack [8].

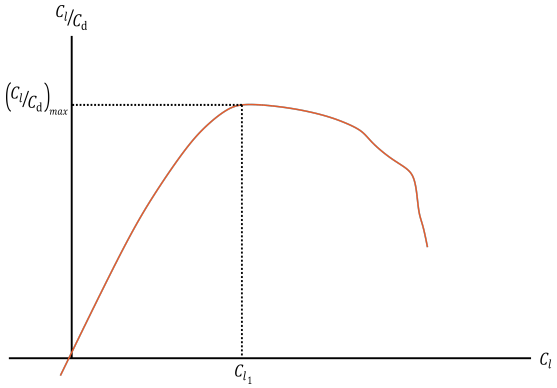

Figure 2.9: Airfoil aerodynamic efficiency variation with the lift coefficient.

2.1.1.6 Low Reynolds Number Airfoils

Recently, some researchers have been performing studies on how to design and optimize airfoils for ranges of Reynolds numbers, where laminar separation bubbles occur. One

example of that is reference [16], that gives a clear understanding of the problems that laminar separation bubbles raise when trying to design an airfoil for low Reynolds operation. [16] also shows the effects of changing the airfoil's shape in order to control the laminar bubble sizes, changing the flow's behavior. These changes can be made in the shape of the velocity distribution in order to control the intensity of the adverse gradients and, therefore, decrease the size of the separation bubble.

In Figure 2.10 it is possible to observe two airfoil geometries and their respective inviscid velocity distributions along the chord for a C_l of 0.55. The SD6060 airfoil is a redesign of the E374 airfoil where the geometry was corrected only in order to improve the inviscid velocity distribution that, because of the bulge located at around 40% of the chord, had a too strong adverse pressure gradient, which caused a large separation bubble that severely deteriorated the E374 airfoil at low Reynolds conditions by increasing it's drag. So, as it is possible to see in Figure 2.11, only by correcting that bulge, creating a lighter pressure recovery gradient, the effects on the drag polar are more visible the smaller the number of Reynolds of operation [16].

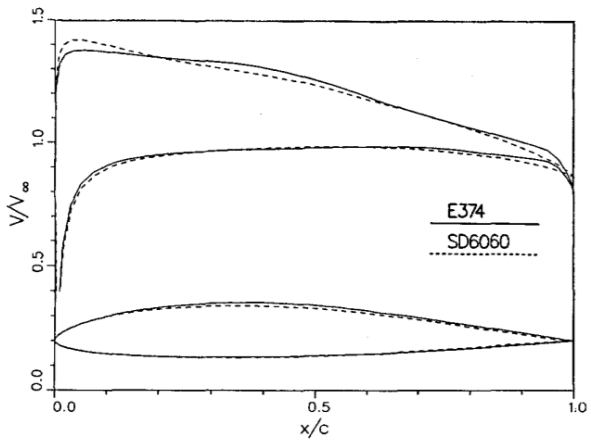

Figure 2.10: Inviscid Velocity distribution along the chord [16].

Other important concept to mention when speaking of airfoil design and optimization is the transition curves. These curves are plots that relate the x position in percentage of the chord, where the transition from laminar to turbulent takes place, for each C_l or α value for both the upper and lower surfaces of the airfoil (see Figure 2.12). Some studies consider the manipulation of the these curves for a given condition of constant Re and C_l as a good approach in order to minimize the drag effects due to separation bubbles on an airfoil [17]. Constant $Re\sqrt{C_l}$ type polars are often used to analyze airfoils because they correspond to straight level flight conditions, considering that all the parameters are constant except for the speed. This allows an understanding of the airfoil qualities for a range of speeds considering straight level flight.

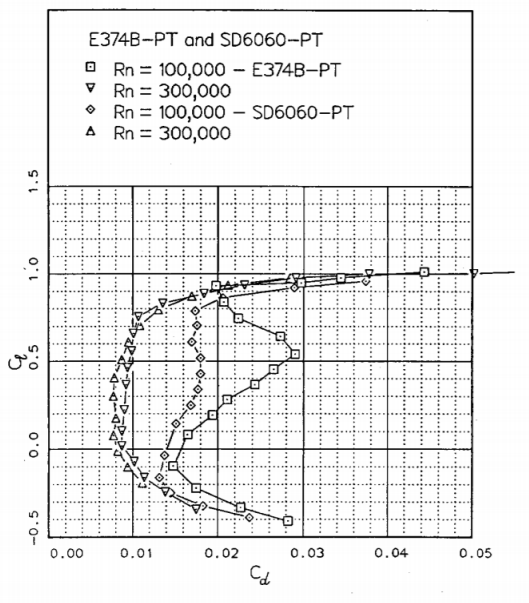

Figure 2.11: Comparison polars: E374B-PT and SD6060-PT at two Reynolds numbers [16].

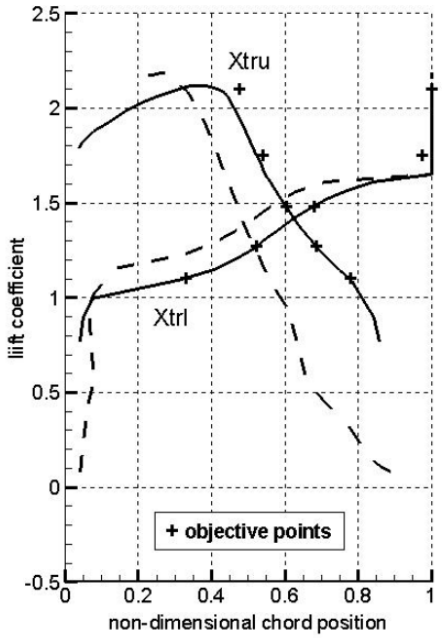

Figure 2.12: Upper and lower surfaces transition curves example [17].

2.1.2 Stability and Control

In order to fly properly, any aircraft has to be both stable and controllable. All in all, the stability of an aircraft can be defined as its capacity to, by itself, return to its original state of equilibrium when disturbed [6].

In the conceptual stage of the design, the stability starts to be concerned when sizing the tail. A concept called tail volume coefficient allows the designer to estimate the tail size having in mind a relation between a destabilizing volume related to the wing and the sta-

bilizing volume of the tail and typical values for this relation [6]. All in all, the higher the tail volume coefficient, the greater the tail influence in stabilizing effect will be. Although this concept is a necessary condition for an airplane to achieve stability, it does not allow the designer to certainly conclude that the airplane will be stable. There are further concepts that must be studied in the preliminary stages of the design in order to verify if the airplane will, in fact, be stable.

There are two important types of stability to study in the preliminary stage when designing an airplane: the static stability and the dynamic stability.

An airplane is statically stable if the forces actuating on it, while it is in a disturbed state, make it recover towards its original state. The dynamic stability of an airplane refers to the way in which the airplane goes back to its original equilibrium state after being disturbed, *i.e*, all the changes in state variables that allow the airplane to stabilize [6].

When an airplane is statically stable it does not necessarily mean that the airplane is also dynamically stable. This may happen when the forces that allow the airplane to return to its original state have too high magnitude, causing the airplane to oscillate around the equilibrium state in a divergent way, causing it to enter an uncontrollable state. Figure 2.13 depicts the different types of stability.

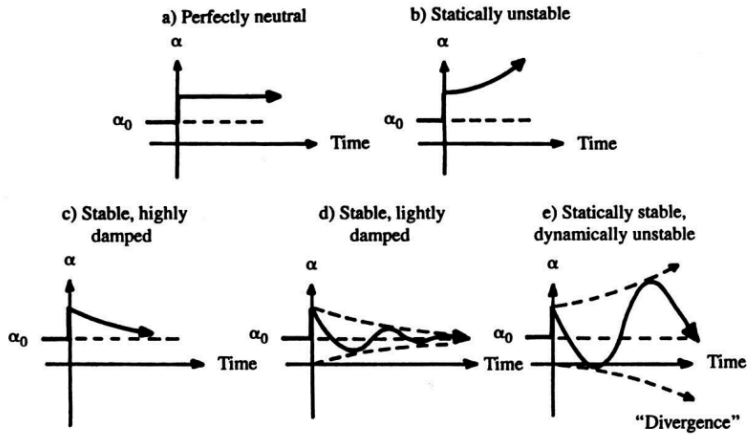

Figure 2.13: Static and dynamic stability [6].

In addition to static and dynamic, the airplane stability can also be divided into longitudinal and latero-directional stability, being the first related to pitching motion and the second to the rolling and yawing motions.

In terms of longitudinal static stability, among the various contributors to the pitching moment about the center of gravity (CG) of the airplane are: the lift through the wing aerodynamic center and the wing moment about the aerodynamic center, the moment arm of the tail times its lift and the distance of the thrust line of the engine to the CG. In order for an airplane to be statically stable, every time it experiences a change in the angle of attack, it must generate moments that oppose that change. For that to happen, the pitching moment *vs* angle of attack of the airplane must have a negative slope and the

pitching moment for zero lift must be positive.

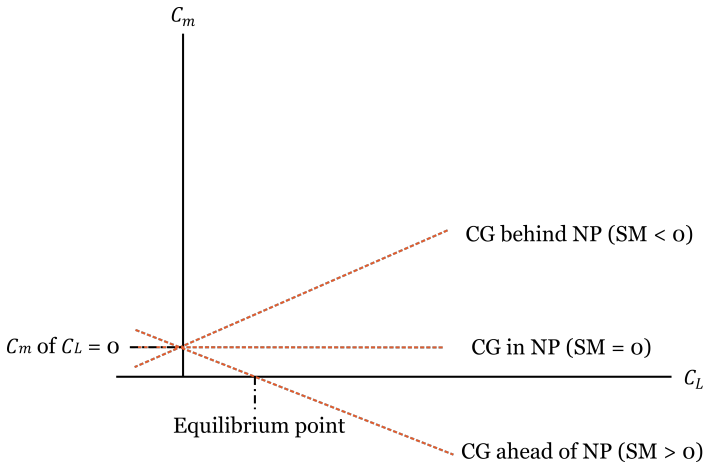

Figure 2.14: Effect of CG position relative to the NP on a C_m *vs* C_L curve.

The most important parameter when it comes to longitudinal stability of an airplane is its static margin (SM) [6]. This parameter gives the distance, in terms of mean aerodynamic chord (MAC) percentage, between the neutral point, x_{np}, - CG location where the pitching moment is independent of the angle of attack - and the center of gravity, x_{cg}. Negative static margin values mean that the center of gravity is behind the neutral point, which means that the airplane is necessarily statically unstable. Typical values of static margin vary between 5% and 10% for transport aircraft and can be higher for general aviation aircraft [6]. Equation 2.5 can be used to calculate this variable for any airplane, being $\bar{x}_{np}$ and $\bar{x}_{cg}$ respectively the positions of the neutral point and the center of gravity in terms of the wing's MAC percentage. Figure 2.14 shows the influence of the CG position relative to the neutral point on a C_m *vs* C_L curve of an airplane. As it is possible to observe, only a positive static margin ensures the existence of an equilibrium point. The higher the static margin, the more negative the slope of the curve, meaning higher longitudinal static stability. It is also possible to estimate the neutral point position in a C_m *vs* C_L graph. Varying the CG position, the neutral point is found when the curve is a straight line parallel to the C_L axis (see Figure 2.14).

$$\text{SM} = \bar{x}_{np} - \bar{x}_{cg} \quad (2.5)$$

When it comes to the static lateral-directional stability, the discussed concepts are close to the ones referred to in the longitudinal stability explanation, but instead of pitching moment, the moments studied are the yaw and rolling moments. It is possible to calculate a lateral neutral point and to perform similar assumptions to those made for longitudinal stability, but it is not commonly determined since the usual process is to determine the CG position with the longitudinal study and then iterate the vertical tail area so that the yaw stability is achieved. In general, since dynamic analysis are frequently needed to obtain

good results to really verify the latero-directional stability of an airplane, the static lateral stability is usually ignored in the conceptual stage of the design and methods like the tail volume coefficient are considered to decide weather latero-directional stability is, a priori, achieved [6].

In terms of dynamic stability, it is important to make sure that the airplane, apart from being capable to return to its equilibrium state after being perturbed, it does so that the returning motion is safe and that does not diverge endangering the aircraft.

In order to check the dynamic stability characteristics of an airplane, it is possible to resort to empirical calculations, numerical flow simulations, wind tunnels or flight testing. In the preliminary design stage, the most advantageous approach is the empirical calculation through dynamic system simulation. When it comes to empirical calculation, multiple solving approaches can also be chosen in order to solve the complex equations of motion of an airplane. The most simple is through the one-DOF (Degree Of Freedom) dynamic equations, a method that although is capable to provide initial references for the dynamic stability of an aircraft, it does not provide correct results for most flight conditions, since in real aircraft motions there are always more than one degree of freedom involved [6]. A more accurate approach for studying the dynamic stability of an aircraft is through six-DOF simulations.

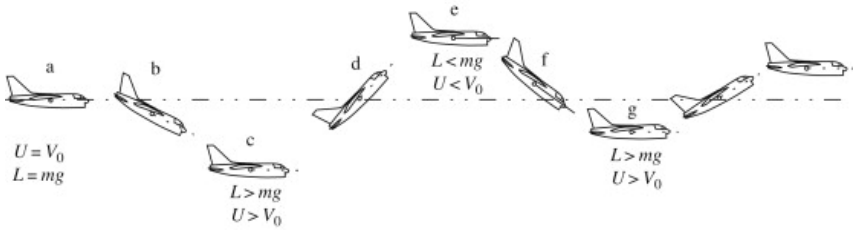

Figure 2.15: Mechanism of a stable phugoid [18].

In this approach, the equations of motion in six-DOF of the in-design airplane can be linearized through the small disturbance theory around the trim flight condition [19] . These equations use data obtained from empirical sources or numerical flow simulation such as the stability and control derivatives and output parameters such as the linear velocities along the three axis, the angular velocities about those axis, and pitch and bank attitude *vs* time.

The solutions for the equations of motion are oscillatory modes, two longitudinal and three lateral. Longitudinally, the oscillatory modes possible to verify are the phugoid mode and the short period mode. The phugoid is a long-period lightly damped mode, characterized by slow pitch, airspeed and altitude oscillations. In this mode, in the initial stage the airplane is trimmed at level flight, until it suffers a perturbation that reduces its speed. When the speed is reduced, the lift is also reduced. This causes the airplane to then accelerate downwards and build up airspeed and lift again. When the airplane starts to climb its speed starts to decrease, repeating this cycle. Figure 2.15 depicts this mechanism in a damped condition due to drag reducing the magnitude of the motion, making it

converge until stabilization [20].

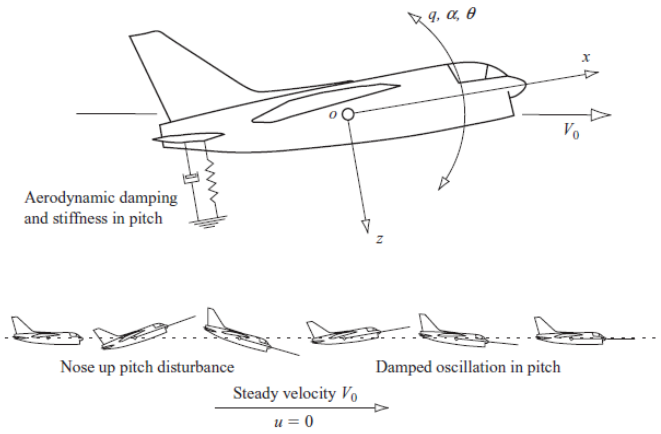

Figure 2.16: Mechanism of a stable short period pitching oscillation [18].

The short period mode is an heavily damped mode that appears when there is pitch disturbances. In this mode, when the pitch is disturbed from trim equilibrium, an aerodynamic spring effect gives rise to an oscillation in pitch and angle of attack that also through the aerodynamics of the system will be damped. It is important to notice that the spring effect is mainly caused by the natural tendency of the airplane to align with the equilibrium AoA, while the damping effect is caused by the oscillatory motion of the airplane. Figure 2.16 illustrates the behavior of this mode [20].

Latero-directionally, as stated previously, there are three different modes responding to perturbations: the roll subsidence or roll mode, the dutch roll and the spiral mode. The roll subsidence mode (or simply roll mode) is a non-oscillatory mode that is responsible to balance the bank of the airplane after it has been disturbed. In Figure 2.17 it is possible to observe the mechanism of the mode. As it is possible to see, after suffering a disturbance by a rolling moment, the airplane begins to roll with an angular acceleration. When rolling, there is a small increase in the angle of attack (AoA) of the down-going wing and a small decrease in the incidence of the other wing. This differential in the AoA and therefore lift produces a restoring moment, responsible to return the roll to its equilibrium state [20].

The dutch roll mode is a short-period oscillatory mode characterized by a waddle from side to side with a coupling between yaw and roll. If this mode is little damped, and therefore excessively oscillatory, it can be really very harmful to flight quality. With the help of Figure 2.18 it is possible to understand the mechanism of this mode: After a disturbance in yaw, the starboard wing yaws aft and its tip rolls up. Then, while the aircraft is rolling until the wings return to a level position, the maximum aft yaw angle is achieved. After this, the starboard wing now yaws forward with its tip low until the maximum forward yaw angle is achieved and the aircraft rolls until the wings are again level. This cycle repeats until it converges to the stable state if the damping is positive. The damping of this mode is mainly determined by the size of the vertical tail, being one of the driving criteria for its

sizing. It is mainly caused by dihedral effect and can be aggravated by flexibility effects at high speeds [20].

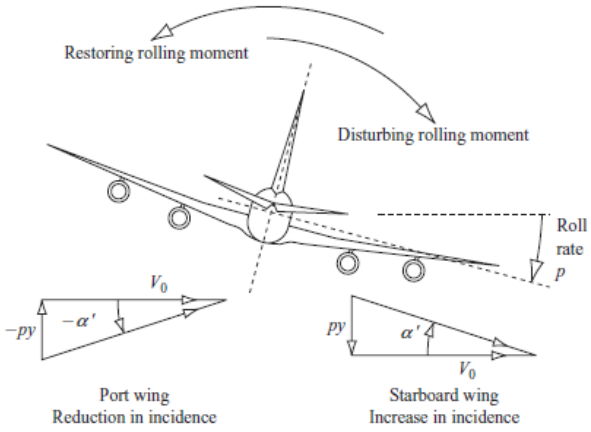

Figure 2.17: Mechanism of roll subsidence mode [18].

The remaining lateral mode is the spiral mode. This mode, as the roll subsidence, is a non-oscillatory mode. It is characterized as being slow and generally unstable. It is usually excited by a disturbance in sideslip and consequently in roll, causing a wing to go low. This condition creates a positive angle of attack on the fin, tendentiously causing an increase of yawing moment. Figure 2.19 can give a better understanding of this mechanism. Although this mode is typically divergent, its time to diverge is so long that corrections can be easily performed to avoid spiral divergence [20].

The behavior of each mode can be mathematically defined by some parameters: The natural oscillatory modes such as the phugoid, the short period and the dutch roll modes are defined by an eigenvector, a natural frequency and a damping factor, while the non-oscillatory modes can be defined simply by an eigenvector and a damping factor. The eigenvector contains the information of the flight variables that describe the mode.

Longitudinally, the behavior is described by four variables: axial speed variation about the steady state u, vertical speed variation about the steady state w, pitch rate q and pitch angle θ. In terms of lateral behavior, its descriptive variables are: the lateral speed variation about the steady state v, roll rate p, yaw rate r and roll angle ϕ.

The damping factor or damping ratio, ξ, is a non-dimensional coefficient that gives information about the degree of damping of a mode. If this value is negative, it means that the mode is not damped at all, corresponding to a divergent behavior. If the damping ratio is positive but lower than 1 the mode is under-damped and if the value is higher than 1 the mode is over-damped. If this parameter equals 1, the mode is said to be critically damped, meaning it is a non-oscillating mode that returns to steady state as fast as possible.

An eigenvalue of a mode is a property that contains information about its frequency and damping. It has the format shown by Equation 2.6, where σ_1 is the damping constant, given by Equation 2.7, where ω_1 is the undamped natural circular frequency given by

Equation 2.8 and ω_N is the natural frequency.

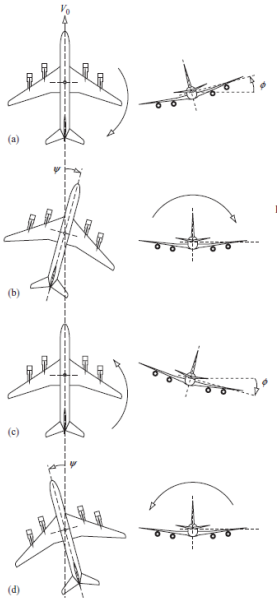

Figure 2.18: Mechanism of dutch roll mode [18].

$$\lambda = \sigma_1 + i\omega_N \quad (2.6)$$

$$\sigma_1 = -\omega_\xi \quad (2.7)$$

$$\omega_1 = \sqrt{\sigma_1^2 + \omega_N^2} \quad (2.8)$$

A commonly used tool to evaluate the stability of a mode through its eigenvalues is the root locus graph. In Figure 2.20 it is possible to see a typical root locus representation of a mode eigenvalue. In the x axis the real part is represented, corresponding to the damping of the mode. In the y axis is represented the complex part, relative to the frequency of the mode. As it is possible to see in Figure 2.20, the further up in y, the higher the frequency of the mode, and the further to the left, the higher its damping. For the mode to be stable, the value in x must be negative.

The time response of each state variable for each mode should also be graphically analyzed. In a time response graph, the response to a mode of each state variable is plotted. This way, it is possible to be aware of the magnitude of the damping and to check if the modes are, for some reason, coupled, which is a condition to avoid since it can produce instability issues.

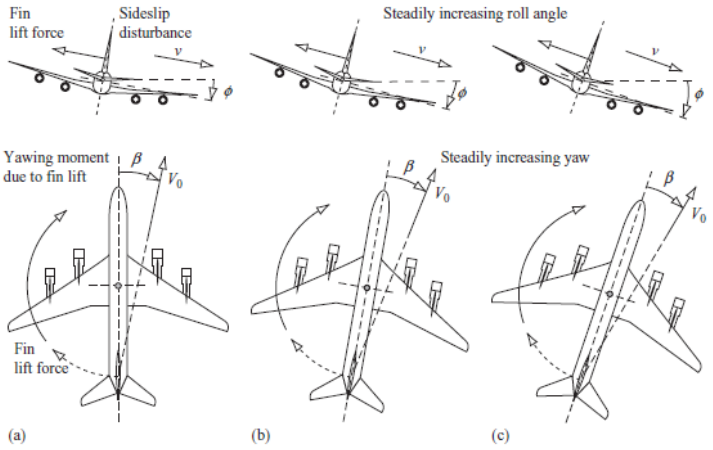

Figure 2.19: Mechanism of spiral mode [18].

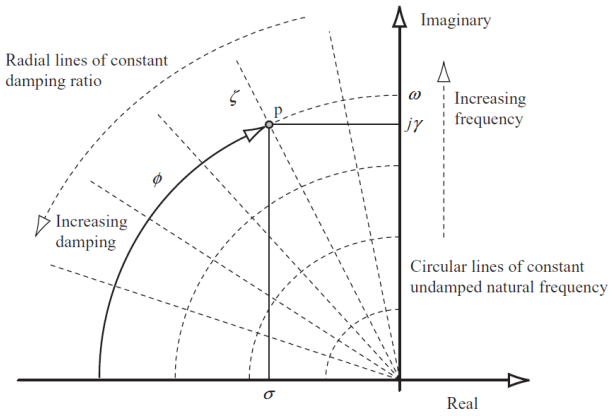

Figure 2.20: Typical root locus representation [18].

2.1.3 Wing Geometry

In addition to the airfoil, the geometry of a wing is also defined by other parameters such as its MAC, aspect ratio, taper ratio, sweep, twist, dihedral, incidence, vertical location and number of wings. Each one of these parameters has significant roles on the wing's aerodynamic performance, stability, weight and ease of manufacturing. In the next subsections some of these parameters and their effects on the overall wing performance are presented. Figure 2.21 gives a representation of the overall wing geometry planform. The most basic parameters of the wing geometry are the reference area, S, the aspect ratio, A, the taper ratio, λ, and the span, b.

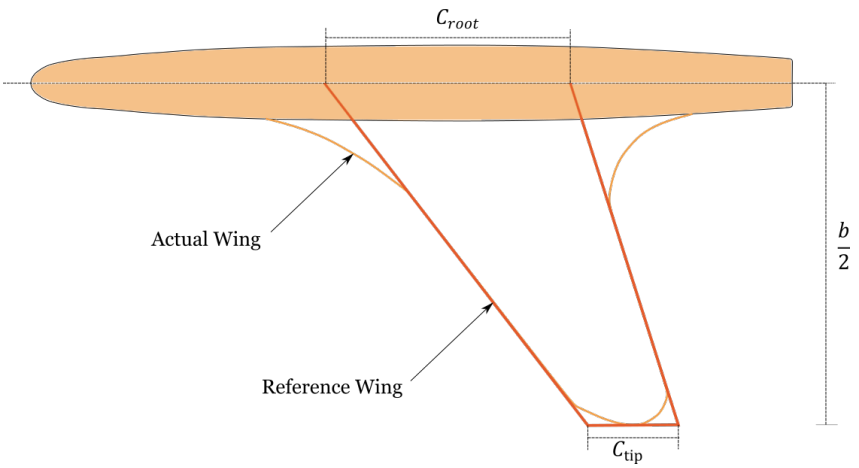

Figure 2.21: Wing geometry.

2.1.3.1 Aspect Ratio

The aspect ratio of a wing is defined as being the ratio between its span squared divided by its surface. This feature has a major importance on the aerodynamic performance and weight of the wing. It can be calculated through Equation 2.9.

$$A = \frac{b^2}{S} \quad (2.9)$$

The wing tip vortex is an effect present in tridimensional wings, and it is described as being caused by the airflow escaping from the lower surface to the upper surface around the wing tip (see Figure 2.22) due to pressure differential, and can represent an huge deterioration on the aerodynamic performance of the wing [6]. The higher the aspect ratio, the further away the tips are from each other, decreasing the influence of this effect on the overall performance of the wing. Although the induced drag is directly dependent on the wing span and not the aspect ratio, once the wing area is usually kept constant, the span will be inversely proportional to the square of the aspect ratio. In this situation, it is possible to state that the aspect ratio actually influences the induced drag [6]. Another negative effect of the wing tip vortex is the decrease in pressure difference between the lower and upper surfaces, which leads to a reduction of the lift near the tip.

Aerodynamically, increasing the aspect ratio of a wing, approximates its features with the ones of the airfoil [6], meaning it will achieve higher C_l values (see Figure 2.23). From the weight and ease of construction point of view, a high aspect ratio may not be the best solution, since that due to the higher bending moment applied on the wing root, more resistant materials it will have in order to withstand the caused stresses.

In addition to aerodynamic performance or weight, there are other features like manoeuvrability, stability, fuel storage capacity, production costs, among others that must be con-

sidered when selecting the aspect ratio of a wing [8]. This way, it is important to mention that there is not an aspect ratio that is adequate for all applications. Hence, it is necessary to take into consideration all the mission requirements in order to perform a wise choice of this parameter.

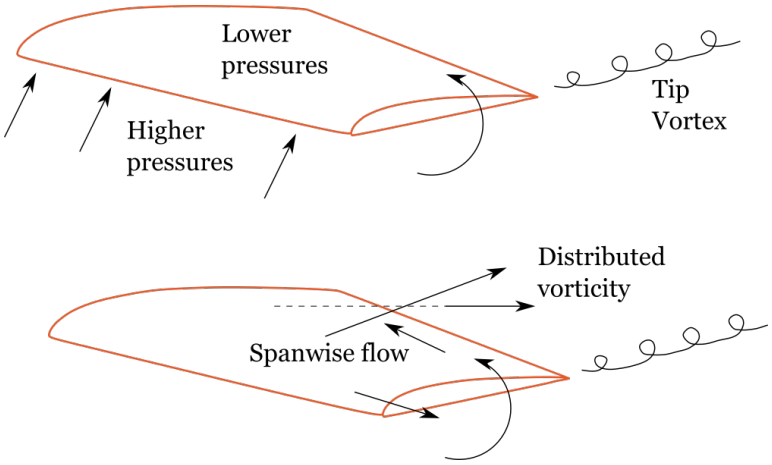

Figure 2.22: Wing tip vortex mechanism (adapted from [6]).

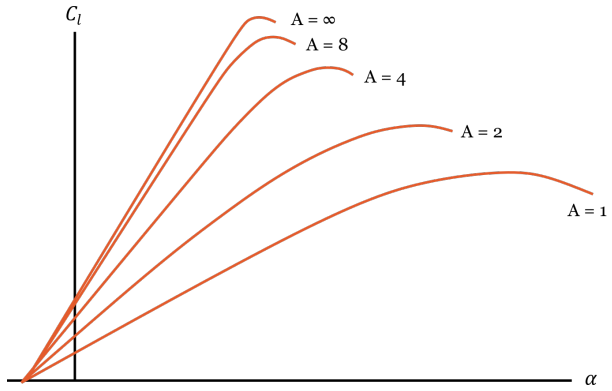

Figure 2.23: Effect of aspect ratio on lift (adapted from[6]).

2.1.3.2 Taper Ratio

The taper ratio is the quotient between the tip chord and the root chord of a simple trapezoidal wing. Its value is given by Equation 2.10 and it influences the lift distribution along the span of a wing. There are three common types of wing planforms when specifying the taper ratio: Rectangular (or untapered), trapezoidal and delta. Typically, a trapezoidal wing has a taper ratio with a value between 0 and 1, the rectangular wing taper ratio is equal to 1 and a delta wing has a taper ratio value of 0 [8].

$$\lambda = \frac{C_t}{C_r}, \qquad 0 < \lambda \leqslant 1 \quad (2.10)$$

The best lift distribution for a planar wing in terms of aerodynamic performance is the

one with an elliptical shape. This shape is visible on wings with an elliptical planform (if planar, untwisted and unswept), and it is preferable because it minimizes induced drag [6, 8]. Since an elliptical wing may be really expensive and hard to manufacture and a rectangular wing provides the farthest distribution from the elliptical, a good solution to minimize induced drag is by tapering a rectangular wing. By doing so, the lift distribution can become very close to the elliptical. Figure 2.24 shows the different lift distributions corresponding to different taper ratios.

Although a tapered wing may provide induced drag reduction due to the lift distribution, it also has a few disadvantages when compared to a rectangular wing. In addition to cost increments and harder manufacturing, the tapered wing also presents inferior stall qualities. This is due to the lower downwash angle of the tip, causing the stall to be nearer the tip in contrast to a rectangular wing, which is harmful for flight safety. This effect can be compensated by a moderate taper together with a washout.

The taper ratio also influences other features such as the weight and control qualities. A tapered wing is typically lighter than a rectangular one because of the lower bending moment which requires not so heavy spars. The delta wing improves aircraft control, once it creates a smaller moment of inertia along the x axis in comparison with the other options.

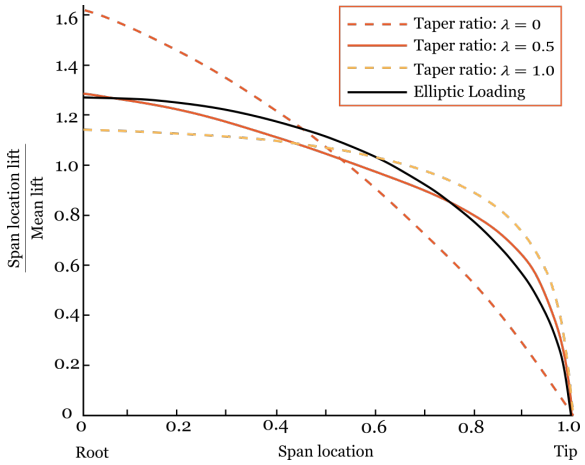

Figure 2.24: Effect of taper on lift distribution (adapted from [6]).

2.1.3.3 Wing Sweep

The sweep angle, typically represented by Λ, can be understood with the help of Figure 2.25. A wing with a positive sweep angle is simply called swept wing, if it presents a negative sweep angle, it is referred as forward swept wing. The sweep angle can also be both a leading edge sweep and trailing edge sweep. This feature is most commonly observed in aircraft with transonic or supersonic operations since, typically, its main function is to reduce wave drag.

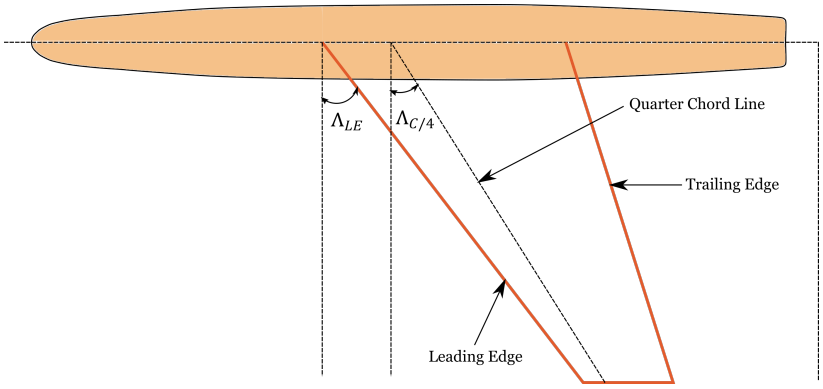

Figure 2.25: Wing sweep.

In subsonic application, the advantages of swept wings are [8]:

- Improving static lateral stability;
- Adjusting the aircraft center of gravity;
- Impacting longitudinal and directional control and stability.

Although effectively there are advantages of using swept wings, they are rarely used in subsonic aircraft, since it doesn't always justify the increase in costs and manufacturing complexity with the performance improvement [8]. Wing sweep can be responsible for weight increases since it increases the structural span of the wing.

2.1.3.4 Incidence

The wing incidence , i_w, for an untwisted wing is simply the angle between the aircraft fuselage and the wing's chordline (see Figure 2.26). The incidence angle is usually chosen in the design stages in order to maximize the aerodynamic performance of the aircraft and the flight quality. There are typical values according to the type of aircraft to be designed, but each case should be analyzed individually. Generally, the requirements used to determine an adequate incidence angle are the following [8]:

- To achieve the desired lift coefficient during cruise flight;
- To minimize the fuselage drag during cruise flight;
- To have a wing with an incidence that allows a safe variation of the angle of attack.

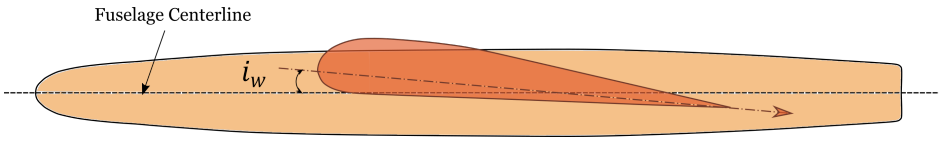

Figure 2.26: Wing incidence angle.

2.1.3.5 Twist

Wing twist is a parameter used to avoid tip stall and to bring the lift distribution closer to the elliptical. It is measured in degrees and typically has a negative value, which means that the wing is twisted downwards from the root to the tip of the wing (see Figure 2.27), also called washout. When the twist has a positive value it is also called washin.

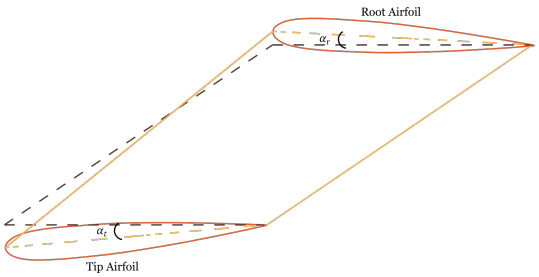

Figure 2.27: Geometric twist.

The twist can be of two types: geometric (Figure 2.27) and aerodynamic (Figure 2.28). In the first one, the wing uses the same airfoil along its span, changing only the incidence in certain sections. For a washout, the incidence decreases from the root to the tip. If the twist is linear, the incidence changes at constant rate along the different sections of the wing. In the aerodynamic twist different airfoils are used along the span in order to achieve the desired washout. In this case, the twist value is measured from the difference between an airfoil's zero lift angle and the root airfoil zero lift angle. A wing can have both of the referred twists. If it happens, the total twist is the sum of the geometric twist with the aerodynamic twist [6]. Both of the twists have advantages and disadvantages. The geometric twist brings problems in manufacturing, since because of the different incidences along the span, it implies that the main spar of the wing has also to be twisted [8].

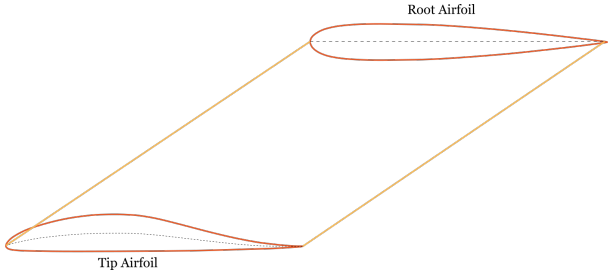

Figure 2.28: Aerodynamic twist .

2.1.4 High-Lift Devices

High lift devices can be a solution for the problem that exists when designing an aircraft requiring large amounts of lift for take off and landing, but not so much when in cruise flight, since it can deteriorate the airplane's performance because of the flap gap. This way, high lift devices are usually used to change the airfoil's camber during flight in order to enable achieving higher values of $C_{L_{max}}$ during take-off and landing. There are two main groups of high lift devices: leading edge high lift devices (LEHLD) and trailing edge high lift devices (TEHLD). Figure 2.29 shows some examples of trailing edge high-lift devices.

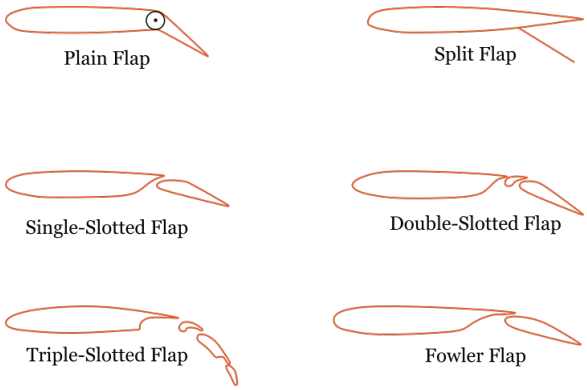

Figure 2.29: Types of TEHLD [6].

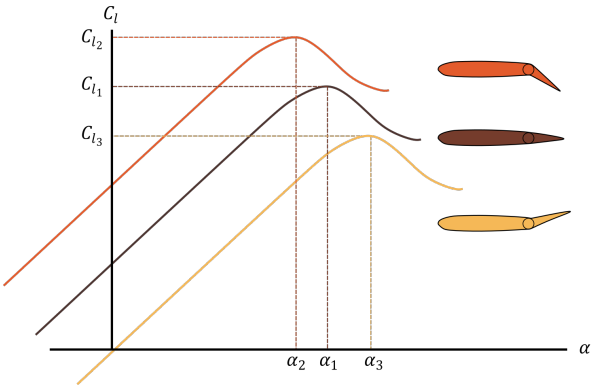

Figure 2.30: Cruise flap effect on C_l *vs* α plot

The most simple HLD is the plain flap. It works by being hinged to the wing in order to be able to be deflected. Deflecting the flap downwards will change the effective camber of the airfoil producing more lift. The more deflected it is, the higher the increase on the maximum lift coefficient, until a maximum deflection angle from which the lift coefficient stops increasing. It is the cheapest and easiest to build, but it is also the less effective increasing the lift coefficient [8].

The plain flap can also be used as a cruise flap. The difference between a regular plain flap and a cruise flap is that the cruise flap can be deflected both upwards and downwards. This provides the ability of not only increase lift coefficient when needed (downwards deflection), but also to help improving the drag polar in cruise by deflecting upwards [21]. Figures 2.30-2.31 show the effects of cruise flaps deflection effects on the lift coefficient

and angle of attack and on the drag polar respectively. It is visible that a downwards deflection of the flaps increases the value of $C_{l_{max}}$ but it also decreases the value of α_s . The upwards deflection of the flap does the exact opposite on the C_l *vs* α plot, but on the drag polar it helps minimizing the drag by providing lower $C_{d_{min}}$ values for off-design lift coefficients.

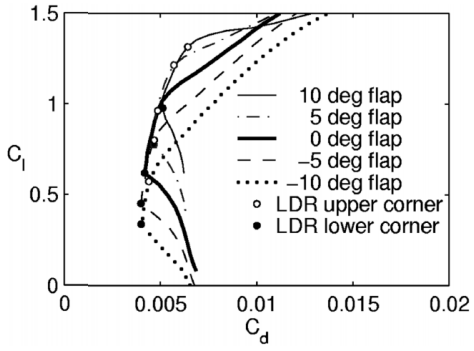

Figure 2.31: Cruise flap effect on C_d *vs* C_l plot [22].

2.1.5 Wing Manufacturing

According to the requirements set in Section 1.4, the wing's skin of UAS30 will be manufactured using the hand lay-up technique. This technique is a composite material lamination process that consists in applying layers of resin and reinforcement to an open mold and let it cure [23]. The number of layers is determined by the desired thickness of the final part and, as the name of the process suggests, it is a manual technique.

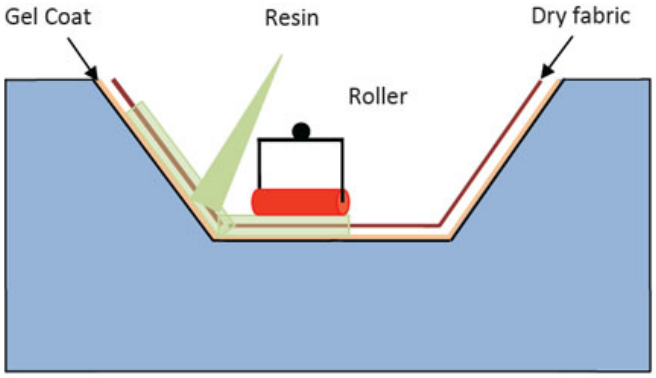

Figure 2.32: Hand lay up [24].

The process can be divided in 5 main steps. First, the open mold is cleaned and sprayed with an anti-adhesive agent responsible to ease the release of the component from the mould. Next, the dry fibers are placed inside the open mold and covered with the resin matrix with a brush (see Figure 2.32). The more layers applied, the thicker the final component will be. If wanted, an initial gel coating layer can also be applied before the fibers and resin layers. In the third step, the wet composite resulting from the layers of fabric and resin is rolled with hand rollers in order to maximize the bond between the fibers and

the resin. After that, the part is subjected to a curing process, with controlled temperature and relative humidity, to harden. The final and fifth step is the removal of the part from the mold and its trimming and cleaning.

Due to the low cost and design flexibility of the molds, and also the possibility of reproducing complex parts, hand lay-up is well suited for parts with low quantity production such as UAV wing's skin, boat hulls, among others. It is also a process that can use a wide range of resins and fibers to produce the composite with the best features for a specific application, and does not require expensive tooling for the cure of the resins, since they usually are room-temperature.

Despite the above advantages, this technique also has a few disadvantages. These include the demand of high skilled craftsman in order to have a quality final product, the possibility of voids in laminates due to lack of uniform distribution of resin, contents diluting possibility and the inability of working with high viscous resins due to the complexity of hand working them.

2.1.6 Aircraft Performance

For propeller-driven aircraft in straight-level flight, performance is determined by parameters such as range, endurance, ceiling, maximum speed and cruise flight conditions [25]. It is the designers' task to find a trade-off between these parameters in order to develop the aircraft with better overall performance for its specific mission profile.

2.1.6.1 Range

The range of an aircraft is defined as the distance it can fly from take-off to landing, without refueling. It is an important indicator of performance for aircraft with missions which consist of flying from a point to another, like civil transportation aircraft for instance.

For constant lift coefficient cruising flight, range can be determined by Equation 2.11 [25].

$$R = \frac{\eta_P}{C}\frac{L}{D}\ln\left(\frac{W_0}{W_1}\right) \quad (2.11)$$

where η_P is the propeller efficiency, C is the specific fuel consumption, $\frac{L}{D}$ is the lift to drag ratio, W_0 is the take off weight and W_1 is equal to $W_0 - W_f$, where W_f is the fuel weight.

In Equation 2.11 the lift to drag ratio can also be written as C_L/C_D. This equation shows that to increase the range at these conditions, propeller efficiency, fuel-weight fraction and lift to drag ratio must be increased, whereas the specific fuel consumption must be

decreased. With that said, keeping fuel fraction, specific fuel consumption and propeller efficiency constant, the maximum range is obtained for $(C_L/C_D)_{max}$ condition.

2.1.6.2 Endurance

Endurance is also a very important parameter when referring to aircraft performance. It is the amount of time that an aircraft can remain airborne from take-off to landing with a given quantity of fuel. It is a major parameter when referring, for instance, to reconnaissance aircraft.

For constant-altitude, constant-lift-coefficient flight, endurance is given by Equation 2.12 [25].

$$E = \frac{\eta_P}{C}\sqrt{2\rho S}\frac{C_L^{\frac{3}{2}}}{C_D}\left[\frac{1}{\sqrt{W_1}} - \frac{1}{\sqrt{W_0}}\right] \quad (2.12)$$

where ρ is the air specific mass.

Equation 2.12 shows that by holding the engine specifications, wing area, altitude (hence air density) and fuel fraction constant, endurance is proportional and dependent on the $C_L^{3/2}/C_D$.

2.1.6.3 Maximum Speed

Maximum speed is one of the specific speeds in straight and level flight. It is an important performance indicator since it dictates the speed which an aircraft can reach with the engine at full throttle. Typically, having a higher maximum speed means having an overall higher cruise speed since it allows the engine to perform well at higher speeds without being at full throttle.

This parameter depends upon many variables such as the engine's power, flight altitude, aircraft geometrical parameters and weight. For piston propeller aircraft, its value is determined by Equation 2.13 [25].

$$P_{max_{SL}}\eta_P\left(\frac{\rho}{\rho_0}\right)^{0.9} = \frac{1}{2}\rho V_{max}^3 S C_{D_0} + \frac{2K(mg)^2}{\rho V_{max} S} \quad (2.13)$$

where $P_{max_{SL}}$ is the maximum engine shaft power at sea level, ρ_0 is the air specific mass

at sea level, C_{D_0} is the zero-lift (or parasite) drag coefficient factor. K is the induced drag coefficient, m the aircraft mass and g the gravitational acceleration.

Also, for an operation where altitude and weight are held constant, maximum speed is dependent (and inversely proportional) to the drag coefficients.

It is then possible to mention that in order to improve a propeller driven aircraft performance with regard to maximizing range, endurance and maximum speed, the values of C_L/C_D and $C_L^{3/2}/C_D$ should be as high as possible, whereas C_{D_0} and K should be as low as possible.

2.1.6.4 Rate of Climb and Climb Angle

In addition to presenting good flight qualities in level flight, an airplane must have good climbing qualities. This allows the airplane to being able to rapidly avoid obstacles by flying up or, for instance, to climb away from turbulence or bad weather conditions fast.

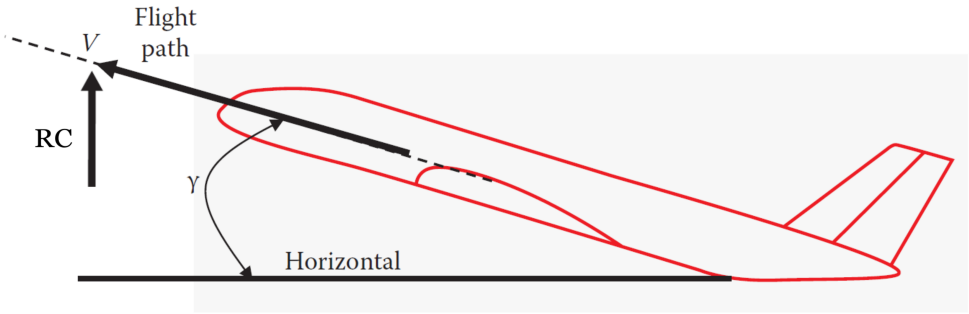

Figure 2.33: Climbing flight parameters (adapted from [25]).

The most important parameter to take into account when defining the climbing performance of an airplane is the rate of climb (RC) [25]. This parameter is the rate of change of altitude per unit of time and it is the vertical component of the velocity vector of the airplane. It can be seen in Figure 2.33. All in all, the higher the rate of climb, the faster the airplane can climb for a given condition. The value of this parameter, for an unaccelerated flight, is obtained using Equation 2.14, where T_a is the available thrust and D is the drag of the airplane or the required thrust. Since power equals $T \times V$, the rate of climb can be defined as the excess power divided by the weight of the airplane.

$$RC = \frac{T_a V - DV}{W} \quad (2.14)$$

Directly related to the rate of climb is the climb angle, γ. This parameter is defined as the angle between the direction of the relative wind and the horizontal (see Figure 2.33). It's

important to distinguish the climb angle from the pitch angle (θ) and the angle of attack (α). All in all, the climb angle is the difference between the pitch angle and the angle of attack. The angle of climb is related to the rate of climb through Equation 2.15.

$$V \sin(\gamma) = RC \quad (2.15)$$

2.1.6.5 Graphical Analysis

Some of the performance parameters referred in this section can be easily estimated recurring to graphical analysis. Those include both the minimum and maximum speeds, the speed of RC_{max} ($V_{RC_{max}}$) and its respective value, as well as the corresponding climb angle. It is also possible to determine the speeds corresponding to the maximum range and maximum climb angle for constant η_p and C.

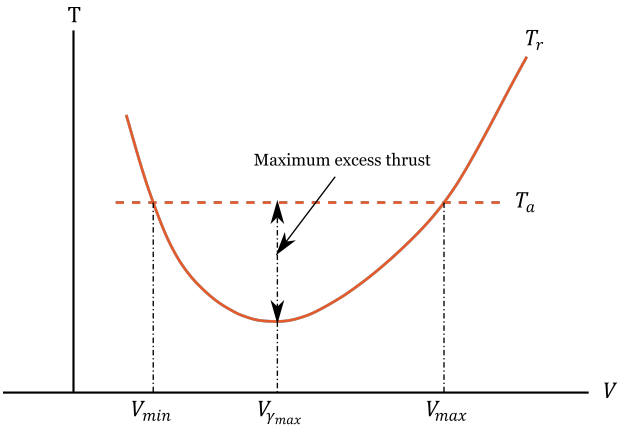

Figure 2.34: Performance parameters on a T *vs* V graph.

In a thrust *vs* speed graph (see Figure 2.34), where the curves corresponding to the required thrust (T_r) of the plane and to the available thrust (T_a) of the propulsive system are represented, some of the referred parameters can be determined. The two intersections between the two curves correspond to the conditions of minimum and maximum speeds (respectively V_{min} and V_{max}), being the minimum speed corresponding to the leftmost intersection and the maximum speed corresponding to the rightmost intersection. Another parameter possible to determine recurring to this graph is the speed for maximum climb angle ($V_{\gamma_{max}}$). This condition corresponds to the speed where the excess thrust is higher, *i.e*, where the difference between T_a and T_r curves is highest.

The power *vs* speed graph (see Figure 2.35) of a propeller driven airplane contains the curves of both the required power (P_r) and the available power (P_a). In a similar way to the T *vs* V graph, having these curves on the same graph, it is possible to define some of the referred performance parameters. The minimum speed (V_{min}), is the leftmost inter-

section between the two curves while the maximum speed is the rightmost intersection. The $V_{RC_{max}}$ is located where the difference between the two curves is highest, meaning the excess power is also highest. Drawing a line through the origin and tangent to the P_r curve also defines the speed for the maximum range ($V_{R_{max}}$).

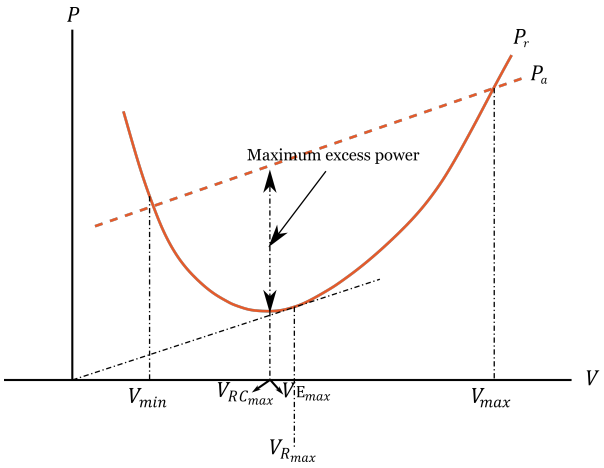

Figure 2.35: Performance parameters on a P *vs* V graph.

2.2 State of the art

2.2.1 Unmanned Aerial Vehicles

An unmaned aerial vehicle (UAV) is, by definition, "... any aircraft operating or designed to operate autonomously or to be piloted remotely without a pilot on board" [26]. These vehicles are subsystems of other systems designated by UAS, short for unmanned aerial systems. UAS consist of the UAVs and the necessary equipment to remotely control them. This equipment includes all of the instruments, software, mechanisms, apparatus, appurtenance or accessories that aren't on board of the UAV, but are necessary to its safe operation.

2.2.1.1 Brief history

The UAVs have been, since their early days, used mainly for military purposes. The first UAV use reports date back to 1894, when the Austrians sent non-piloted balloons loaded with timed explosives above Venice as a military attack [27]. Since then, UAVs have been evolving to more complex and automation directed systems.

Years 1900 - Sperry Aerial Torpedo

Right at the beginning of World War I, funded by the U.S. Navy, Elmer Sperry began developing a type of aircraft whose mission was to deliver warheads near enough to enemy warships in order to inflict damage on them. Another restriction imposed by the U.S. Navy was that the airplane would have to be self flown when sent on mission [28]. This way he, together with Dr. Peter Cooper developed the first aerial torpedo, converting the Curtiss-N9 trainer aircraft into Sperry Aerial Torpedo, the first remote controlled UAV. Although this UAV was never used in real fight conditions, it has performed multiple successful tests.

Years 1930 to 2000

After World War I, there was a sudden world wide decrease of interest in developing unmanned aircraft. That was until the 1930's when new UAVs started to be developed. One big example is the DH.82B Queen Bee, the first returnable and reusable UAV . They were used by Royal Air Force and Royal Navy as target drones and were developed as an adaptation from the training piloted aircraft De Havilland Tiger Moth, to which floats and radio control equipment have been added [29]. Their range could go up to 480 km at a speed of 180 km/h [30]. They were retired in 1947.

During World War II, Germany developed the said to be the most important UAV of its time: the V1. Also known as "flying bomb", "buzz bomb" or "doodlebug", it was known for being the first ever cruise guided missile [31], it had a wingspan of 5.5 m, carried a warhead with 850 kg, could go to speeds up to 580 km/h and had range of 240 km[32]. It was propelled by a pulsejet engine which, at the time, was also by itself a remarkable revolution in engine technology [33].

Since Sperry and until the end of World War II, it is clear that the goal of developing UAVs was mainly to create aircraft that could fly by itself inflicting damage to a target as a weapon or as training target drones. This mindset would be changed by the arrival of the Cold War. The Cold War, as the name suggests, was known for being an almost "fighting free" war, where the armed conflict was no longer the focus of the conflict, but instead the tension of the powers in question caused by not knowing what enemy's next step would be. For that reason, reconnaissance and decoy UAVs started to be developed until the current days, where they have the biggest share of UAV market, being used on military operations, environment monitoring and other areas [34].

The first reconnaissance UAVs were merely adaptations of target drones with cameras and decoy equipment installed. The biggest example is the BQM-34A "Firebee" drone, a modified "Firebee" target drone with cameras installed. This UAV was made through the "Red Wagon" project, a program contracted by U.S. Air Force to Ryan Aeronautical

Company in 1960. As stealth mechanisms they have been equipped with a non conductive paint, wire screen on the nozzle and radar absorbing pads. Although this UAV did perform well, only two of it were built because of cuts on military research and engineering budget [18].

Ryan Aeronautical Company developed the ”Red Wagon” project, thus ”kick-starting” modern era UAV. Until the 90’s many projects of UAVs have been developed. Always motivated mainly by wars, the military forces have always pursued forms of being stronger than the opponents. This bore to developing new military UAVs, both combat and reconnaissance or decoy. Some examples of it are ”Lighting bug” and ”Buffalo Hunter” - Vietnam War; Samson air launched UAVs - Israel / Lebanon Conflict (1982); RQ-2A Pioneer - Operation Desert Storm and Operation Desert Shield (Persian Gulf Operations - 1990-1991); RQ-4 Global Hawk and RQ-1 Predator - Operation Enduring Freedom and Operation Iraqi Freedom (2001-2006) and Ababil II - Israel / Lebanon Conflict (2006) [18].

2.2.1.2 UAV Applications

Nowadays UAVs are much more than military war machines. It is possible to find almost infinite applications for unmanned aircraft. Those applications can go from, as already seen, military to civil, passing through law enforcement.

With regard to military applications, UAVs can perform all types of tasks, not only in terms of use on the battlefield, but also in peace making, coast monitoring among others. Reference [35] enumerates the following UAV roles within military operations:

Army

UAVs used for army operations, due to the range of conditions that they face, must be versatile. Those operations are:

- Covert Reconnaissance and Surveillance;
- Fall-of-shot Plotting;
- Target Designation by Laser;
- NBC Contamination Monitoring;
- IED and Landmine Detection and Destruction;
- Electronic Intelligence;
- Teaming of Manned and Unmanned Systems;

- System Mobility;
- Persistent Urban Surveillance.

Navy

As far as the operation of UAVs for the navy is concerned, it can be divided into three types, being them off-shore operation, off-board operation and long-range support from airfields. For each one of these types of operation there are certain restrictions and specifications that the UAVs must have. Having this in mind, the specific roles that Navy's UAVs perform are:

- Fleet Detection and Shadowing;
- Radar Confusion;
- Missile Decoy;
- Anti-submarine Warfare;
- Radio Relay;
- Port Protection;
- Over-beach Reconnaissance;
- Fisheries Protection;
- Detection of Illegal Imports;
- Electronic Intelligence;
- Maritime Surveillance.

Air Force

In the air force, the UAVs operation goes through:

- Long-range Reconnaissance and Strike;
- Airborne Early Warning;
- Electronic Intelligence;
- Pre-strike Radar and Anti-aircraft Systems Counter;
- Interception;

- Airfield Security.

Because of the large number of applications, it is possible to conclude that unmanned aerial vehicles, regarding military applications, can be very versatile and perform multiple tasks that can avoid manned crews to get into situations that involve risk.

Civil

Widely used by military services, UAVs are also now more often being used for civil proposes, given the capacity of carrying payloads useful for civil applications such as photographic sensors.

Once again, [35] gives some examples of civil UAVs applications that are seen these days:

- Aerial Photography;
- Crop Sowing and Spraying;
- Meteorological Services;
- Police Authorities.

In addition to those referred applications, there are currently other known applications for UAVs, such as suntry borders monitoring, pollution monitoring, power-lines inspection, fire monitoring and combat, prevention of illegal fishing, such as crop monitoring, coast traffic monitoring, ports and traffic monitoring and assistance, terrain mapping, among others.

2.2.1.3 UAV Classification

UAVs have several ways of being categorized or classified. Some of those may be by its function, size, range, configuration, among others.

Configuration wise, UAVs can be fit in four categories:

1. Fixed-wing;
2. Rotary-wing;
3. Flapping wing;
4. Blimp.

Fixed-wing UAVs are used more often on missions that require higher horizontal speeds, range or endurance. They take-off from runways or catapults and land on runways, by parachute or are caught in mid-air. Rotary-wing UAVs, on the other hand, are typically used for missions that require very low horizontal speeds or stationary flight. Their take off and landing are typically vertical and they produce lift and thrust using their rotors. Flapping-wing and blimps are less used. The first are UAVs whose wings perform movements that produce lift and thrust at the same time. This configuration has been studied in recent years. Blimp UAVs are vehicles that have extreme endurance and use lighter-than-air gases to fly, just like unmanned Zeppelins or hot-air balloons.

Another way of classifying UAVs is by its type of control. This classification can be made by three distinct types of controlling methods:

1. Autonomous;
2. Semi-autonomous;
3. Ground-control or remote piloting.

There is also a classification based on the UAV's weight and range. This classification can be summarized with the types and typical uses, in Table 2.1

Table 2.1: UAV classification according to weight and range [36, 35].

Type	Mass	Maximum Range	Category	Typical Use
Nano	$\leq$ 200 g	5 km	Fixed wing, multirotor	Reconnaissance, surveillance, inspection
Micro	200 g - 2 kg	25 km	Fixed wing, multirotor	Surveillance, data gathering
Mini	2 kg - 20 kg	40 km	Fixed wing, multirotor	Surveillance, data gathering
Light	20 kg - 50 kg	70 km	Fixed wing, multirotor	Surveillance, data gathering
Small	50 kg - 150 kg	150 km	Fixed wing	Surveillance, data gathering
Tactical	150 kg - 600 kg	150 km	Fixed wing	Surveillance, data gathering
MALE	600 kg - 1000 kg	200 km	Fixed wing	Surveillance, cargo transportation
HALE	600 kg - 1000 kg	250 km	Fixed wing	Surveillance, data gathering, signal relay
Heavy	1000 kg - 2000 kg	1000 km	Fixed wing	Surveillance, data gathering, signal relay
Super Heavy	$\geq$ 2000 kg	1500 km	Fixed wing	Surveillance, data gathering, signal relay

2.2.2 Market study

In this section, a market study to identify the characteristics of UAVs similar to the UAS30 is presented. The goal of this study is to fit the UAS30 in a set of UAVs with similar characteristics in order to check discrepancies and set realistic performance improvements to achieve with this dissertation.

Although the UAS30 range is not known, its classification according to Table 2.1 can still be made in terms of the maximum take-off mass. With 35 kg of maximum take-off mass, the UAS30 can be defined as a Light UAV. Light UAVs are unmanned aerial vehicles with masses between 20 kg and 50 kg, with ranges typically around 70 km and are commonly used for surveillance and data gathering.

In order to fit the UAS30 in a set of similar characteristics, a data gathering of UAVs with MTOM between 20 kg and 50 kg was performed. The collected data can be seen in Table 2.2. The available parameters of the CEiiA UAS30 were also included in the table in order to facilitate comparison.

It is possible to observe in Table 2.2, that the considered UAVs show an average maximum take-off mass of 29 kg, acceptably close to the 35 kg of the UAS30 and 7.2 kg of payload. The average span is 3.5 m, while the average endurance is 11.6 h and range is 604 km. In terms of speed, the data show an average stall speed of 15.6 m/s, cruise speed of 26.8 m/s and maximum speed of 39 m/s.

Table 2.2: UAV comparative table.

Model	**MTOM** [kg]	$\mathbf{m_{pay}}$ [kg]	**b** [m]	**E** [hr]	**R** [km]	$\mathbf{V_{stall}}$ [m/s]	$\mathbf{V_{cruise}}$ [m/s]	$\mathbf{V_{max}}$ [m/s]
Aerodreams Strix	48	-	3.6	-	750	-	33.3	44.4
Aerosonde MK 4.7	36.4	9.1	3.7	14	140	-	23.15	38.6
EAGLE PLUS	21.3	10.3	3.5	5	-	24	28	32
F330	23.7	8	3.3	8	-	-	22.2	33.3
Flamingo MK3	25	5.5	4.1	18	-	13.3	25 - 29.17	33.3
Fulmar X	20	8	3	12	800	-	27.8	
IA17	25	2.5	2.8	5	80	-	-	44.4
LUNA	40	-	4.17	6	100	-	19.4	-
Neptune	36.3	9	2.13	4	148	-	30.9	43.21
Notromo Yarará	30	7	3.98	6	50	12.5	31.9	40.3
Orbiter 3	30	5.5	4.4	-	150	-	-	36
Penguin B	21.5	10	3.3	20	1800	13	22	36
Penguin C	23	-	3.3	20	100	-	19 - 22	32
Ptero G1	20	5	3.13	8	800	13.89	23.6	34.7
Raybird-3	21	7	2.985	20	2500	18	33.3	44.4
Redkite	21.5	-	3.3	6	100	-	-	-
ScanEagle	22	3.4	3.1	24	1800	-	25 - 30	41.2
ScanEagle2	26.5	5	3.11	18	-	-	25 - 30	41.2
ScanEagle3	36.3	9.1	4	18	-	-	20.6 - 25.7	41.2
Sea Cavalry (SD40)	40	6	3.7	6	-	-	40	50
Skylark 3	40	-	4.7	6	100	-	-	-
Sparrow	45	12	2.44	6	-	-	30.9	51.44
TEKEVER AR3	22	8	3.2	10	1200	-	33.3	-
Thunder B	32	4	4	24	150	16.7	-	37.2
Viper M10G	20	11	3	8	100	11.3	22.2	34.7
ZALA 421-16E5	29.5	5	5.3	6	100	18	-	30.56
Average	**29**	**7.16**	**3.5**	**11.58**	**603.78**	**15.63**	**26.83**	**39**
CEiiA UAS30	35	5	4.29	5	-	10.5	20	-

After summarizing the information in Table 2.2, scatter plots for three different parameters in terms of the maximum take-off mass were created: span, cruise speed and endurance.

In Figure 2.36 it is possible to observe the scatter plot of the span values in terms of MTOM. As it is possible to conclude through the trend line, despite some outliers, the span tends to be higher the higher the MTOM. The UAS30 stays well above the trend line, meaning it has a significantly wider span than it would be expected for a UAV with its mass, which can help achieve lower speeds and future increases of MTOM.

In terms of cruise speed *vs* MTOM, the comparison between the UAS30 and the other considered UAVs can be seen in Figure 2.37. As it is possible to observe, higher MTOM values tend to produce higher cruise speeds. The UAS30 is a complete outlier in terms of

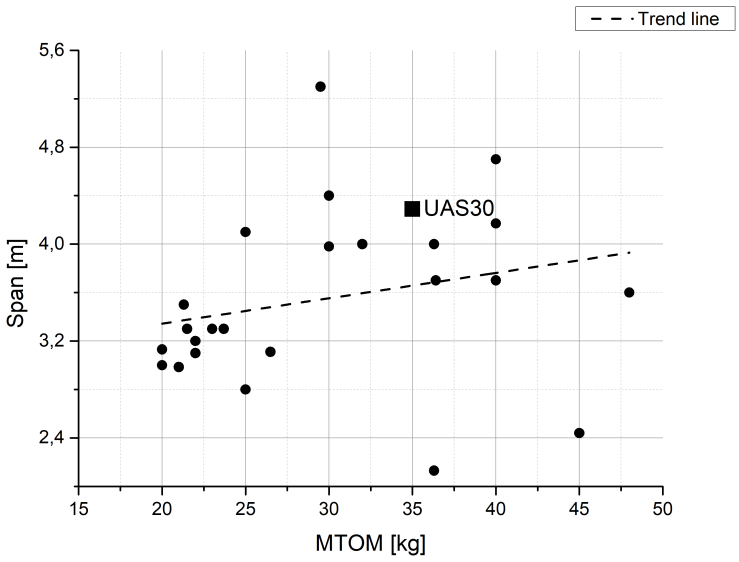

Figure 2.36: Scatter plot of span *vs* MTOM of the UAVs present in Table 2.2.

this parameter, with a cruise speed way below the trend line. Although low cruise speeds can be beneficial to specific missions such as photo or video collection since it allows the aircraft to slowly fly above the target to collect the data with higher precision, for missions that require wide operation ranges or in windy environments it is a highly harmful feature. The main focus of this dissertation will be designing a wing that can provide higher cruise speeds.

The graph that contains the data regarding endurance *vs* MTOM can be seen in Figure 2.38. Since there are too many outliers, the trend line does not allow much conclusions in terms of tendency. Despite that, it is still possible to observe that the endurance of the UAS30 is considerably lower than the other UAVs with similar MTOM values. Although the main focus of the dissertation is not to design a high endurance set of wings, it is still interesting to try and improve this parameter.

The market study allowed to understand where the UAS30 fits in terms of some important parameters when compared to similar UAVs. It is clear that the UAS30 was developed to operate at low speeds unlike most of the UAVs of its class. The goal is to design a wing that could allow the UAS30 to be above or at least closer to the cruise speed average of its class.

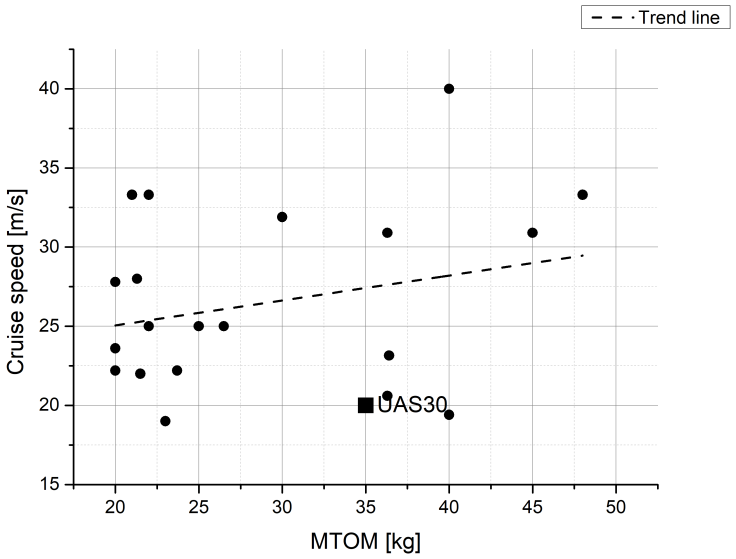

Figure 2.37: Scatter plot of MTOM *vs* cruise speed of the UAVs present in Table 2.2.

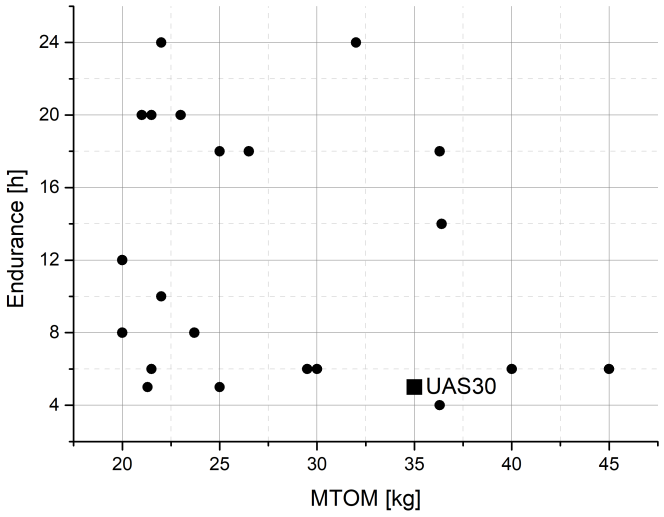

Figure 2.38: Scatter plot of MTOM *vs* Endurance of the UAVs present in Table 2.2.

Chapter 3

Methodology

In this chapter the adopted methodology for the design of the new wing solution for the UAS30 considering the proposed requirements is presented in detail. An identification and brief description of the tools utilized throughout the referred methodology is also made.

The summarized stages involved in solving the proposed problem of this dissertation were the following:

1. Identification of the requirements of the new UAS30 wing and the objectives of the dissertation;
2. Definition of the problem solving strategy;
3. Literature review stage - In this stage the theoretical foundations needed for the present dissertation were reviewed, a market study and a framework of the UAS30 in relation with similar UAVs were performed so that it was possible to visualize where the UAS30 could be improved;
4. Chord and span limit values determination based on the existing UAS30 tail, using the tail volume coefficient concept. Consequently, the reference Reynolds number and design lift coefficient were determined in order to obtain a starting point for the new wing design;
5. Selection of the reference airfoil for the new wings through a sample comparison process using XFOIL [14] analysis module within XFLR5 [7];
6. New airfoil design based on the reference airfoil and through transition curves manipulation [37] using XFLR5's inverse airfoil design module;
7. Cruise flap implementation study;
8. Mean aerodynamic chord and span values selection through performance indicators comparison, taking into account the limits imposed by the span and chord limitation study;
9. Taper ratio, sweep angle, dihedral and incidence values determination through performance indicators comparison of arbitrarily considered parameter values, using the original UAS30 wing's values as starting points.

10. Stability analysis and comparison;

11. Final wing performance estimation and comparison of the UAS30 with the new design and the existing wings;

12. Dissertation conclusions and future works definition.

3.1 Utilized Tools

XFLR5/XFOIL

XFOIL [14] is a program developed by Prof. Mark Drela which uses a potential flow panel method along with an integral boundary layer formulation in order to analyze flows around airfoils, thus predicting their performance at low Reynolds numbers. The code iterates the outer and inner flow solutions on the boundary layer displacement thickness until achieving convergence. This way, XFOIL calculates the viscous pressure distribution, including the influence of laminar separation bubbles and trailing edge separation. In order to calculate transition, the program uses an approximate e^N envelope method, where N is the amplification factor. This method consists in following only the most amplified frequency at a given point of the airfoil after the instability point to obtain the amplitude of that disturbance. When this amplitude achieves an empirically determined value, the transition is assumed. The N value was kept as the predefined value of 9 throughout the utilization of the program in this work. Several studies to validate the good capability of the program in predicting subsonic airfoil performance when compared with CFD or experimental methods have been carried throughout the years (per example [38]), what makes it a reliable choice for the needs of the current dissertation.

XFLR5 is an open source software created by André Deperrois and it was initially developed to serve as an user-friendly version of the XFOIL program. Currently, beyond airfoil analysis and design using the XFOIL code, XFLR5 also allows the aerodynamic and stability analysis of finite wings and small airplanes such as sailplanes and small UAVs. The theoretical foundations and limitations behind the wing and airplane aerodynamic estimations can be consulted in [7].

Microsoft Excel

Microsoft Excel is the most used spreadsheet software in the world. All calculations, comparisons and decision tables made throughout the dissertation were made using this software. Excel also presents a programming language of its own, VBA, which allows the automation of several repeated calculations.

Prop Selector

Prop Selector [39] is a program created by Brian R. Gyles that allows the performance estimation of small aircraft propellers with two, three or four blades. The program utilizes as inputs the air speed, RPM (revolutions per minute), number of blades, blade pitch and propeller diameter and outputs the thrust generated by the propeller, the output power, the absorbed power and the propeller efficiency. The calculations performed by the program are based on propeller data from NACA [40]. In this dissertation Prop Selector was utilized in order to select an adequate propeller for the UAS30 and to obtain thrust information for the final wing performance estimation.

3.2 Span and Chord Limits Determination

In order to design a new set of wings for the UAS30, it was necessary to fulfill the stability requirements imposed by the existing tail. The relationship between the tail size and the wing's span and chord is given by the tail volume coefficients. This concept allows the determination of values of span and chords for the new wing that do not negatively affect the vehicle's longitudinal stability by knowing the parameters of the original aircraft tail. The chord and span limit values are of extreme importance, since they give a starting point for both the operational Reynolds number determination, required for the airfoil selection, and for the geometrical parameters definition.

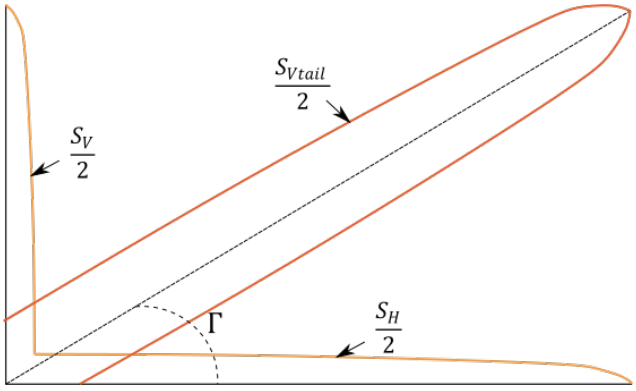

Figure 3.1: Projected areas method parameters.

In order to find the values that limit both the span and the chord sizes for the new wing, the tail volume coefficient concept was used. The original UAS30 tail dimensions were used as the starting point for this study.

Since the UAS30 uses a V-Tail configuration and the tail volume coefficient relates the wing chord with the horizontal tail area and the wing span with the vertical tail area, the first step for the use of this method was to convert the parameters of the V-tail into conventional tail's parameters.

The conversion of the V-Tail parameters into equivalent conventional tail ones was made

by using the projected areas method. An illustration of the v-tail area and respective projections can be seen in Figure 3.1.

In Figure 3.1 S_{Vtail} is the V-Tail area, S_H the projected horizontal area, S_V the projected vertical area and Γ is the dihedral angle of tail surface.

Having a value of $S_{Vtail} = 0.657$ m² and $\Gamma = 38.7°$, it was possible to determine the projected areas.

Using trigonometry, the determination of S_H and S_V was given respectively by Equations 3.1 and 3.2.

$$\cos\Gamma = \frac{S_H}{S_{Vtail}} \quad (3.1)$$

$$\sin\Gamma = \frac{S_V}{S_{Vtail}} \quad (3.2)$$

The obtained values of the horizontal and vertical projected areas were:

$$S_H = 0.513\,\text{m}$$

$$S_V = 0.41\,\text{m}$$

Having obtained these values, the following step was to define intervals of acceptable values of tail volume coefficients for both of the projected areas. These intervals were defined by comparing the values of the original UAS30 tail volume coefficients, obtained by Equations 3.3 and 3.4, and the typical intervals, given by [41].

$$\bar{V}_H = \frac{l_H S_H}{\bar{c} S} \quad (3.3)$$

$$\bar{V}_V = \frac{l_V S_V}{b S} \quad (3.4)$$

In Equations 3.3 and 3.4, l_H and l_V represent the distances from the vehicle CG to the respective aerodynamic centers of both of the tail projections, and $\bar{c}$ the wing's mean aerodynamic chord.

The obtained values of the original tail volume coefficients of the UAS30 are the following:

$$\bar{V}_H = 0.497$$

$$\bar{V}_V = 0.051$$

And the typical intervals given by [41] are:

$$0.35 \leqslant \bar{V}_H \leqslant 0.5$$

$$0.03 \leqslant \bar{V}_V \leqslant 0.06$$

As so, the UAS30 tail volume coefficients are both within the acceptable values. For that reason, the intervals used for limiting the tail volume coefficient were the ones given by [41]. Having the intervals defined, the following step was to rearrange Equations 3.3 and 3.4 so that it was possible to find a relation between the chord and span and the tail volume coefficients. The obtained equations were:

$$b\bar{c}^2 = \frac{l_H S_H}{\bar{V}_H} \quad (3.5)$$

$$b^2\bar{c} = \frac{l_V S_V}{\bar{V}_V} \quad (3.6)$$

Replacing the known values in Equations 3.5 and 3.6, *i.e*, the projected areas dimensions and the limit volume coefficients, and solving the equations with respect to span, four functions were found: two related to the horizontal tail volume coefficient limits and two related to the vertical tail volume coefficient limits. The functions are the following:

$$F1 : b = \frac{1.847}{\bar{c}^2}$$

$$F2 : b = \frac{1.29}{\bar{c}^2}$$

$$F3 : b = \sqrt{\frac{17.26}{\bar{c}}}$$

$$F4 : b = \sqrt{\frac{8.631}{\bar{c}}}$$

Plotting the four functions allowed to check their intersection points. Those points limit the possible combinations of span and mean aerodynamic chords that comply with the stability pre-requirements of the UAS30 tail.

3.3 New Wing Reference Airfoil Selection

As stated in Subsection 2.1.1, the airfoil plays one of the most important parts in the aerodynamic performance of an aircraft with a medium or high aspect ratio ($A > 6$). For that reason, it is necessary to perform a conscious choice of the airfoil or set of airfoils to use in the wing.

3.3.1 Reynolds Number Determination

The selection of the airfoil must be performed taking in account the conditions in which the in design aircraft will operate. The first parameter to define in order to perform an accurate selection of an airfoil for a given operation is the reference Reynolds number. In this case, instead of defining the Re value, the $Re\sqrt{C_L}$ was computed. This constant is a better indicator of a fixed wing aircraft operation at level flight, since it classifies its behavior for the whole range of speeds for constant aircraft mass and flying altitude [7].

For the determination of the Reynolds number, the first step was to compute the maximum lift coefficient of the original UAS30. For that, Equation 3.7, with the known MTOW and stall speed (obtained from the original XFLR5 project of the UAS30) was used.

$$C_{L_{max}} = \frac{2W}{\rho V_{Stall}^2 S} \quad (3.7)$$

Having the $C_{L_{max}}$ calculated, the theoretical value of $C_{l_{max}}$ of the airfoil was calculated using Equation 3.8 taking into account the UAS30 wing's aspect ratio [42].

$$C_{l_{max}} = \frac{(A+2)\, C_{L_{max}}}{A} \quad (3.8)$$

With the intersection points found in the span and chord limitation study together with the airfoil's theoretical $C_{l_{max}}$, it was possible to compute values of theoretical $C_{L_{max}}$ for each one of the span and chord pairs. That was possible using Equation 3.8 subject to $C_{L_{max}}$ and computing the resultant aspect ratios of the coordinate pairs.

After that, it was then possible to calculate values of $Re\sqrt{C_L}$ corresponding to the different chord and span conditions. For each pair, two $Re\sqrt{C_L}$ values must be calculated. One corresponding to sea level operation, and the other to 3000 m operation. Table 3.1 shows a summary of the data used to compute the $Re\sqrt{C_L}$ for both altitudes, as well as their values.

Table 3.1: $Re\sqrt{C_l}$ calculation parameters.

MAC [m]	**Span [m]**	S **[m²]**	A	$C_{L_{Max}}$	$V_{Stall_{SL}}$ **[m/s]**	$V_{Stall_{3000m}}$ **[m/s]**	$Re\sqrt{C_L}_{SL}$	$Re\sqrt{C_L}_{3000}$
0.583	5.44	3.17	9.34	1.49	10.89	12.64	530176	393465
0.734	3.43	2.52	4.67	1.27	13.25	15.39	749731	556406
0.459	6.14	2.81	13.38	1.57	11.25	13.06	443077	328825
0.578	3.87	2.23	6.69	1.39	13.42	15.58	626565	464999

For each one of the altitudes, an average value of $Re\sqrt{C_L}$ was calculated, and after that, the average of the averages was computed in order to obtain the final reference $Re\sqrt{C_L}$. In this case, the final obtained value was the following: $\left(Re\sqrt{C_L}\right)_{ref} = 5,12 \times 10^5$.

3.3.2 Design Lift Coefficient Determination

Another crucial parameter for the course of the design of the new wings is the design lift coefficient. This parameter corresponds to the lift coefficient around which all the design parameters of the wing will be chosen. In this case, it was considered that it was most advantageous to design the wings taking into account primarily the cruise flight. As so, the design lift coefficient was calculated regarding level-flight conditions, *i.e*, the lift was considered to be equal to the weight of the aircraft. The design lift coefficient was calculated using Equation 3.9. The considered weight corresponds to the MTOW of the original UAS30 (343.23 N), V_{cruise} was the average value obtained in the market study (26.8 m/s), the wing area is the original UAS30's area (2.281 m²) and the air related parameters are considered at sea-level conditions.

$$C_{L_{design}} = \frac{W}{1/2\rho V_{cruise}^2 S} \quad (3.9)$$

After computing the values in Equation 3.9, the output value was $C_{L_{design}} = 0.33$

3.3.3 Airfoil Pre-Selection

With the $\left(Re\sqrt{C_L}\right)_{ref}$ and the calculated design lift coefficient for the operation conditions of the UAS30, the following step was to find a sample of airfoils that would serve as comparison with the original one. There are plenty of airfoil coordinates available in literature. For this study, the existing airfoils in [43], were the considered sample.

The database has a total of 1578 airfoils. As so, a pre-selection had to be performed in order to avoid spending extra time analyzing in depth inadequate airfoils that, *a priori*, would not fulfill the specific goals of this work.

Having all the 1578 airfoil coordinate files, it was necessary to adjust them so they could

be properly analyzed and hence compared. The adjustments made were the following:

- Normalize all the airfoils (convert each airfoil's chord value to 1);
- Refine all airfoil coordinates to 160 points.

Since the number of airfoils was too large to be possible to perform such adjustments individually, a Python script for XFOIL software was used. The script automatically opened each one of the airfoil files present in a directory and used XFOIL commands to both normalize and refine the airfoils.

When all the airfoils were ready for analysis, *i.e*, normalized and refined, XFLR5 software was used to perform the analysis. The analysis made to the airfoils with XFLR5 was, in this case, the "XFOIL direct analysis". This type of analysis uses the XFOIL algorithm to simulate the airfoils' behavior in the considered conditions. After this type of analysis is performed, the outputs are the graphs referred in Subsection 2.1.1.5, as well as the operational points used to map those graphs. The necessary inputs to perform the analysis were:

- Airfoil coordinates;
- Type of analysis (in this case Type 2 (Fixed Lift));
- A range or list of $Re\sqrt{C_L}$ values;
- The wanted AoA range to analyze;
- The maximum number of iterations to be performed before skipping to the next point calculation.

The strategy adopted to analyze all the 1578 airfoils was to perform the analysis in groups of 15 airfoils, deleting the airfoils that induced the software to crash or that presented results that were visibly far from the expected reality. This considerably reduced the airfoil sample that would be present in the following screening stage. After this process, the airfoil quantity has dropped down to 581 airfoils.

Having the 581 airfoil analysis performed and all the operational points exported into text files, the following step was to perform the data analysis of the operational points of each airfoil. For that, a Python script together with Excel were utilized. The Python script task was to import the results of each analysis that were stored in text files into an Excel worksheet, then, a VBA script organized each worksheet and, given some parameters created a comparison table and outputs the 15 best airfoils to the given criteria.

The method used to compare the airfoils and score them is presented in [44]. The weighted score method is a way to compare a given number of airfoils to the desired operation. This

method can be adopted when pre-selecting the airfoils because although it does not perform an in-depth comparison of the airfoils at the actual conditions, it is a good way to filter a large amount of airfoils so that the in-depth analysis can be performed more accurately in a smaller number of airfoils that, in a general level, will be suitable for the requirements of the mission.

This method requires the following set of inputs for each airfoil:

- The parameters of the analysis;
- The criteria used to classify those parameters;
- The weight of each parameter;
- The score of each parameter;

After executing the method, the results were calculated by multiplying the scores of the parameters with their respective weights. Table 3.2 shows the criteria and weights used for this specific study.

Table 3.2: Weighted score method parameters. (Adapted from [44]).

Parameter	Evaluation criteria	Selected weight score
C_{l_0}	Closest to $C_{L_{design}}$ is the best	0.15
$C_{l_{max}}$	Highest is the best	0.1
α_{stall}	Highest is the best	0.1
$C_{d_{min}}$	Lowest is the best	0.15
C_l of $C_{d_{min}}$	Closest to $C_{L_{design}}$ is the best	0.1
$(C_l/C_d)_{max}$	Highest is the best	0.1
C_l of $(C_l/C_d)_{max}$	Lowest is the best	0.25
C_m	Closest to zero is the best	0.05

The weights were chosen taking into account the requirements of the UAS30 new wing design. As so, highest weights were given to the parameters which ensure better performances at higher speeds, such as low drag coefficients and lift coefficients corresponding to the $(C_l/C_d)_{max}$ as low as possible. The parameters related to maximization of range were taken as more important than the parameters related to endurance, given the dissertation objectives. The stability related parameter (C_m), was also not given a weight, since the focus of this airfoil selection was more on the performance side of the design.

3.3.4 Airfoil Comparison

As stated previously, the weighted score method is a good method to filter a large amount of airfoils, but not a great way to define the airfoil that absolutely represents the best compromise in order to fulfill the specific requirements of the in-design aircraft among a given sample.

To carry out the final selection of an airfoil for the UAS30 new wing, a more detailed analysis was performed. The first step was to create an XFLR5 project with the 15 pre-selected airfoils, as well as the original UAS30 airfoil. With those airfoils, an XFOIL direct analysis with the same inputs as before was carried out to all of them.

With the analysis performed, the most important polar graph in this case is the one that relates the C_l/C_d with the C_l. This polar is an indicator of the performance of the airfoil for the whole range of the aircraft operation. To quantify the quality of each airfoil, a reference C_l/C_d that would ensure a good performance of the aircraft was considered and then, a ratio between the highest and lowest C_l, corresponding to that considered C_l/C_d value, for each airfoil - C_{l_2}/C_{l_1} - was computed. The higher the ratio, the better the performance of the airfoil for a wider range of conditions. In this case, the considered reference C_l/C_d value was 60.

After that comparison made, the following step was to simulate the airfoils when included in the wing of the original UAS30. For that, XFLR5 wing and plane (airplane) design was used. In this feature of XFLR5, a representation of the UAS30 wings and tail could be made, and then an analysis to simulate the flight conditions of the aircraft could be executed. In order to perform this analysis, an XFOIL direct analysis was performed to a large range of Reynolds numbers for each one of the airfoils in order to acquire data for the wing and airplane analysis. Note that this analysis was performed simply to have a comparison term between the two airfoils in in-airplane conditions. As so, the results of this analysis were not considered for performance classification of the airplane since not all the conditions like extra drag contributions or inertial parameters were strictly considered.

One of the requirements for the new set of wings of the UAS30 is that they must be compatible with the spar of the original UAS30. As so, the absolute thickness of the wing section has to be equal or higher than the absolute thickness provided by the original section. For this specific stage, in order to analyze the airplanes with the different airfoils, Equation 3.10 was used so that all the wings had the same absolute thickness. The span was held the same as the original UAS30. Again, this step was performed solely taking into account the performance comparison of the airfoils, and was not used in any way to select any other wing parameter.

$$c_{new} = c_{original} \times \frac{(t/c)_{original}}{(t/c)_{new}} \quad (3.10)$$

With the span and chord for each one of the airfoils to be analyzed, the wings were created in XFLR5. The tail parameters were the same present in the original UAS30 for all the analysis. The taper ratio, dihedral, incidence angle and sweep were also held the same as the original UAS30 for this stage.

Having the wing geometry defined for all the airfoils, the airplane analysis could then be performed. The results of the analysis are polar graphs. The most important aspect to take into account in this case was the graph that relates the required thrust (T_r) with the speed (V) and the one that relates C_L/C_D also with the speed. In the first graph, an arbitrary value of constant available thrust was considered and then, the maximum speeds of the aircraft were visualized and compared. The stall speed, considering the $C_{L_{max}}$ value of each wing were also compared. It is important that the wings provide a good maximum speed but do not sacrifice the stall speed. In the second graph, C_L/C_D for the range of speeds of the different wings were compared in order to see which one could perform better for a larger maximum speed.

3.4 Airfoil Improvement

The selection of the reference airfoil for the mission of the UAS30 performed in the previous section allowed the attainment of the best airfoil among a given sample of airfoils. That does not mean that the obtained airfoil was the absolute best choice for the given requirements. This made it possible to try and improve the airfoil geometry so it could present an even better performance under the selected conditions.

Since the airfoil holds a major importance when it comes to an aircraft's performance, several ways of designing increasingly better airfoils have been studied by the designers throughout the years. In this approach, the method utilized for improving the previously selected reference airfoil is presented in [17]. Briefly, the method consists of improving a given airfoil by manipulating its lower and upper surfaces, so it improves the drag polar of the airfoil, hence improving the overall performance.

In order to apply the referred method, XFLR5 has an airfoil inverse design function that was used. This function allows the user to manipulate the airfoil's speed distribution along the upper and lower surfaces of an airfoil for any given C_l or angle of attack condition to obtain the desired shape.

Having the airfoil polars already calculated, the graphs considered for comparison were: the drag polar, the transition curves (of both upper and lower surfaces) in terms of C_l and the graph that relates the C_l/C_d *vs* C_l.

With the graphs prepared, the first step was to observe the transition curves and try to relate their shape with the drag polar and the C_l/C_d *vs* C_l graph , *i.e*, to check points where the airfoil was showing higher values of drag coefficient or where the performance was harmed and relate them with the transition curves. Typically, curves with too steep slopes and transition points located too early witness lack of performance due to larger drag coefficients. Having this done, the following step was entering the inverse design module of XFLR5 and observing the speed distributions for both surfaces of the airfoil. The process

was to find the transition points and try to delay them further aft without inducing turbulent separation. The transition points could be identified by the discontinuities between the inviscid and viscous speed distributions. The upper or lower surface were changed at a time, so the changes could be controlled and less abrupt. After modifying the distribution as desired, the following step was to store the modified airfoil, analyze it and check the changes in the previously referred graphs.

The improvement of airfoils through this method is an iterative and time consuming process since sometimes small changes can induce a deterioration of performance on the airfoil instead of improving it because of real viscous flow unpredictability. The goal was to repeat the process until an adequate overall improvement of the airfoil parameters was achieved. That improvement could be finally checked with the method used in the airfoil selection section: considering a reasonable value of C_l/C_d and computing a ratio between the highest and lowest C_l values for both the reference airfoil and the generated airfoil. An increase in the ratio constitutes an increase in the overall airfoil score.

3.5 Cruise Flap Implementation Study

Since the UAS30 is an unmanned aircraft, it can have certain automatic flight control mechanisms. These may include the possibility of implementing cruise flaps along the whole span and to have a system to set them at different angles for different operating conditions. This can help to reduce the airfoil drag at certain C_L values or to achieve higher lift coefficients for specific flight phases such as take-off and landing [21]. With a system like this installed, the main indicator of the performance of the airfoil is no longer the efficiency curves of the original airfoil, but instead, the outer perimeter of the overlay of the efficiency curves of the different flap setting angles. An increase in the overall performance of the aircraft can be achieved in this way.

In order to verify the benefits of the flap implementation in the UAS30, the first step was to choose the type of flaps to implement. For this case, primarily because of the reduced complexity, it is beneficial to use trailing edge plain flaps. The percentage of the chord that the flap would occupy was also an important parameter to take in account. Since the hinge x/c position is directly related to the flap length, different hinge x/c positions mean different flap behaviors [45].

XFLR5 has a feature that allows the simulation of the effects of flaps in a given airfoil. Apart from the x/c position where the flap hinge will be placed, the y location of the hinge in terms of thickness percentage must also be selected. For this case $y = 0$ (lower surface) was chosen since the flaps, if used, will also serve as ailerons. The other parameter to select is the flap deflection angles to analyze. In XFLR5, each deflection angle is applied to the airfoil and the flapped airfoil saved, so that XFOIL analysis can be performed to each flap deflection angle.

The selection of the flap hinge x/c position was made by selecting a set of possible values and analyzing the effects in a set of flap deflection angles for each considered x/c value. After that, the different performance parameters were compared. The chord percentage that showed the most advantageous parameters was held as the selected position for the x/c position of the flap hinge.

After selecting the flap's percentage chord, the following step was to verify if there was an improvement in performance for any C_l values for a set of flap deflection angles. For that, a range of flap deflection angles were considered to be analyzed. With the analysis performed, the polars of the different angled flapped foils were overlapped and the outer perimeter of those curves was carefully observed in order to check for improvements in the overall performance of the airfoil in comparison with the polar of the unflapped airfoil.

3.6 UAS30 Plane Analysis

So far, the presented methodology focused only on the selection of the most appropriate airfoil for the requirements of the new UAS30 wing. From now on, the methodology used to choose the remaining geometric parameters of the wing is presented. For this, the first step was to remake a UAS30 model with an acceptable degree of accuracy within the possibilities of the XFRL5 and to perform the necessary analysis regarding its performance in order to have a start point for selecting the remaining parameters.

In order to perform the airplane analysis in XFLR5, firstly it was equally necessary to create a mesh of polars for the airfoils used in the aerodynamic surfaces. To create this mesh, the coordinates of the airfoils that will be used in the airplane were imported to XFLR5. With the coordinates imported, an XFOIL batch analysis was performed. This type of analysis allows performing XFOIL analysis to multiple airfoils for multiple Reynolds numbers and multiple angles of attack. The Reynolds numbers range to be analyzed must be enough so that all the possible flow conditions are within this range. In order to ensure that, a large range was selected. In this case, a range between Re =1.0$\times$10^5 and Re =1.0$\times$10^7 was chosen.

The increment between Re values within this range was chosen in such a way that a sufficient amount of polars was generated so that XFLR5 could interpolate the missing data between the analyzed points with reasonable precision to perform the airplanes analysis without having to calculate too many operating points, increasing significantly the computation time. A good way to achieve that, is to use different increments according to the magnitude of the Reynolds sub-ranges, *i.e*, between Re =1.0$\times$10^5 and Re =5.0$\times$10^5 an increment of 1.0$\times$ 10^5 can be used, between Re =7.5$\times$10^5 and Re = 2.0$\times$10^6 , an increment of 2.5$\times$ 10^5 and between Re =3.0$\times$10^6 and Re =1.0$\times$10^7 an increment of 1.0$\times$ 10^6 can be selected. This provides an adapted mesh, since the effects of altering the Reynolds number are more visible in the lowest Re region.

With the mesh of polar points for both airfoils generated, the following step was to enter the Wing and Plane Design module of XFLR5. In this module there is a tool to generate a new plane (airplane). Entering this tool, a menu with the needed parameters to generate a new airplane is shown. The parameters needed to be defined in the case of the UAS30 were:

- Airplane inertia;
- Main wing;
- Elevator.

In the airplane inertia section, all the known mass points of the airplane were added, as well as their respective coordinates and, as an output, the total mass of the airplane and the coordinates of the center of gravity were displayed. The mass and positions of all UAS30 components can be seen in Table 3.3. Note that the referential is in the position of the leading edge of the root of the wing, where the positive direction for x is towards the tail and for z is upwards.

Table 3.3: Mass and position of the UAS30 components.

Component	**Mass [kg]**	x **position [mm]**	z **position [mm]**
Ballast	3	-750	0
Avionics	2	-150	0
Payload	5	-150	0
Batteries	2.8	-150	0
Fuselage	4.4	192	-132
Fuel system	0.5	243	0
Fuel	3.5	243	0
Wing	7	281.01	49.83
Engine	1.6	700	0
Left boom	1	1112.5	0
Right boom	1	1112.5	0
Tail	3.2	1414	310.97
Total	**35**	**226.69**	**21.8**

The main wing definition requires the input of its offset from the predefined reference position and of the wing incidence. In this case, the offset was null (x = 0 mm and z=0 mm) and the wing incidence was 1.893 º. After these parameters were added, the geometrical features of the wing were input. The wing can be defined in different sections in order to be possible to define tapered, swept and geometrically or aerodynamically twisted wings. For each section, span, chord, leading edge (L.E) offset (do not confuse with the previously referred offset from the main referential), dihedral, twist, airfoil and panel parameters were introduced. Table 3.4 shows the wing parameters for the original UAS30.

The definition of the V-Tail is very similar to the one of the main wing. The offset coordinates for the UAS30 tail introduced were x = 1350 mm and z= 622 mm. In this case, the airfoil used was the NACA0010 and, in order to define a V-tail, only one section with

the full span of the tail and the correct dihedral was inserted. The input values in these parameters are shown in Table 3.5.

Table 3.4: Original UAS30 main wing parameters definition.

Section	y [mm]	Chord [mm]	L.E offset [mm]	Γ [deg]	α_t [deg]	Airfoil
1	0	703.2	4.39	1.9	0	AH79-100C
2	2145	360	90	0	-3	AH79-100C

Table 3.5: Original UAS30 V-tail parameters definition.

Section	y [mm]	Chord [mm]	L.E offset [mm]	Γ [deg]	α_t [deg]	Airfoil
1	0	330	-75	-38.7	0	NACA 0010
2	996	330	-75	0	0	NACA 0010

Besides the inertia, main wing and tail parameters, a body definition for the fuselage could also be made, but it is not advised, since the results of analysis performed to airplanes with defined bodies are way less precise [7]. Although a body geometry was not defined, it is still important to add the drag contributions of the components apart from the wing and tail. Fuselage and landing gear drag take a big share in performance degradation of the aircraft. To add these contributions to the overall airplane drag, XFLR5 offers the possibility to add the drag coefficients of the wanted components and their respective reference areas in order to include those within the overall drag account.

In order to perform an estimation of the drag contributions of the missing elements, the methodology present in reference [46] was followed. In the original equation present in the document for the determination of the zero lift drag coefficient of the wing-body combination, there are two terms: one relative to the wing contribution and another relative to the body contribution. The term relative to the wing contribution was not considered in this methodology since XFLR5 already takes that into account. The term relative to the body contribution can be seen in Equation 3.11 where C_{f_B} is the turbulent flat plate skin friction coefficient of the body, l_B the length of the body, d the equivalent diameter of the body, $(S_S)_e$ the wetted area of the body, S_{ref} the wing area, R_{WB} the wing-body correlation factor, S_B is the body maximum frontal area and C_{D_b} the base drag coefficient based on the maximum frontal area, given by Equation 3.12, where $\frac{d_b}{d}$ is the ratio of base diameter to equivalent diameter and $\left(C_{D_f}\right)_b$ is the zero lift drag of the body exclusive of the base.

$$(C_{D_0})_B = C_{f_B}\left[1 + \frac{60}{(l_B/d)^3} + 0.0025\frac{l_B}{d}\right]\frac{(S_S)_e}{S_{ref}}R_{WB} + C_{D_b}\frac{S_B}{S_{ref}} \quad (3.11)$$

$$C_{D_b} = \frac{0.029\left(\frac{d_b}{d}\right)^3}{\sqrt{\left(C_{D_f}\right)_b}} \quad (3.12)$$

The geometrical parameters of the fuselage were extracted from the CAD file of the original UAS30 and the determination of the wetted area of the body was performed recurring to reference [47]. The values of the parameters used to compute the zero lift drag coefficient of the body can be seen in Table 3.6.

Table 3.6: Parameters utilized to estimate the drag contribution of the UAS30 body and their respective values.

Parameter	**Value**
l_B [m]	1.53
d [m]	0.27
C_{f_B}	0.00269
$(S_S)_e$ [m²]	1
R_{WB}	1.7
d_b [m]	0.155
S_B [m²]	0.05
$C_{D_{f_b}}$	0.07254
C_{D_b}	0.02024
$(C_{D_0})_B$	0.003042

For the determination of the incremental drag coefficient due to landing gears, reference [46] gives the expression represented in Equation 3.13 where S_G is the reference area used for landing gear drag coefficients (usually $b_{wheel} \times D_{wheel}$ where b_{wheel} is the wheel width and D_{wheel} is the wheel diameter) and $C_{D_{G_{C_L=0}}}$ is the zero lift drag coefficient of the landing gear based on S_G.

$$\Delta C_D = \frac{S_G}{S_{ref}} \left(C_{D_{G_{C_L=0}}} \right) \quad (3.13)$$

The $C_{D_{G_{C_L=0}}}$ values were taken from empirical data present in [46] and they vary according to the type of landing gear configuration (if it is retractable or nonretractable, if the wheels have fairings or not, type of struts, etc.). The UAS30 landing gear has a tricycle arrangement (with a main gear and a nose gear) without wheel fairings. The data used for computing the landing gear drag coefficient can be seen in Table 3.7.

With the drag coefficient contributions from the fuselage and landing gear estimated, they were input in the XFLR5 airplane analysis along with their corresponding areas so that the software could compute the drag caused by them. Since the wing drag estimated by XFLR5 is also a little optimistic, 10% of the minimum drag coefficient of the airplane was also added as an extra drag coefficient. Other inputs required in the airplane analysis were the polar type, the analysis methods, the inertia properties, reference dimensions and density and viscosity of the air. Type 2 polar (fixed lift) was selected. In this type of polar, XFLR5 adjusts the freestream speed so that the lift generated by the airplane is always equal to its weight, simulating level flight for every speed condition. The analysis method was held as horseshoe vortex (as advised in [7] for this kind of analysis, *i.e*, airplanes whose wings present dihedral and sweep), the inertia was considered as the one defined earlier by the

mass points and the aerodynamic data were the one considered at sea level, by ISA.

Table 3.7: Parameters utilized to estimate the drag contribution of the UAS30 landing gear and their respective values.

Parameter	Value
b_{wheel} [m]	0.047
D_{wheel} [m]	0.152
S_G [m^2]	0.0072
$C_{D_{G_{C_{L=0}}}}$ (Main gear)	0.565
ΔC_D (Main gear)	0.00173
$C_{D_{G_{C_{L=0}}}}$ (Wheels)	0.18
ΔC_D (Wheels)	0.00165
$C_{D_{G_{C_{L=0}}}}$ (Nose gear)	0.45
ΔC_D (Nose gear)	0.00138
ΔC_D (Full gear)	0.00477

With all the parameters defined for the analysis, the following step was to select the angles of attack of interest. In this case, in order to have a comprehension of the whole operation a big range of angles of attack was selected so that every operation condition is depicted ($-15^\circ \leq \alpha \leq 25^\circ$).

3.7 Span and Chord Selection

After having the reference analysis of the UAS30 with the new airfoil, the influence of changing some geometrical parameters of the wing was then studied in order to improve even further the airplane performance. The first two parameters to be changed were the span and the chord. These parameters have a major influence in the performance of the wing and had to be carefully selected since changing them, also, changes parameters such as the aspect ratio and the wing loading, parameters that are critical for the proper operation and performance of the aircraft.

The first parameter to be changed and analyzed was the span. Going back to the span and chord limitation study, the limiting values of the span that would not affect the requirements imposed by the tail volume coefficient were utilized. For the lower limit, the study has given a value of 3.43 m, while for the upper limit a value of 6.14 m has been defined. With these values, a set of possible spans was defined. In this case, it was decided that six different span values would be considered. The considered span values for analysis were: 3.43 m, 3.972 m, 4.514 m, 5.056 m, 5.598 m and 6.14 m.

With the values of possible spans to be considered, airplanes for each span value were created in XFLR5. All the features besides the span were kept equal to the UAS30 with the new airfoil, *i.e*, the tail, the wing mean aerodynamic chord, airfoil, offset, taper, dihedral and wing incidence were kept unaltered. The drag contributions added in the previous section were also recalculated for each span value since the reference area changed with the span.

Having the airplanes created for each span value, airplane analyses were performed in order to check the influence of each span in the overall performance. Comparing the performance parameters between the different span values allowed to evaluate the impact of the span on the overall performance of the aircraft. The span value that provided the best results was selected.

After the best span value according to the mission characteristics being selected, it was then possible to select a new mean aerodynamic chord value recurring to a similar methodology. The first step was to check once again the chord and span limitation study (see Section 4.1) and to see what are the minimum and maximum allowed values for the mean aerodynamic chord considering the new selected span.

With those two limit values, the analyzed mean aerodynamic chord values were: 0.535 m, 0.556 m, 0.577 m, 0.598 m, 0.619 m and 0.64 m.

Having the set of six different MAC, airplanes were created in XFLR5 for each value. In the same way that the airplanes for the different span values were created, those airplanes for each MAC value had to retain the original geometrical features apart from the airfoil (FEMS1017 was used), the new span and the root and tip chords that were selected in order to keep the original UAS30 wing taper ratio.

Analysis of each airplane were performed and the results compared. The MAC that allowed about the same stall speed with flaps and the best maximum speed while not significantly degrading the maximum $\frac{L}{D}$ was selected.

3.8 Taper Ratio, Twist, Sweep, Dihedral and Incidence Angle Selection

With the main geometrical parameters of the wing defined, *i.e*, airfoil, span and mean aerodynamic chord, the next and final step of the design of the new UAS30 wing was to vary the remaining wing design parameters in order to further improve performance or to obtain better performance, stability and safe stall qualities.

The original UAS30 provided the starting points for the referred parameters. Thus, in order to perform a final selection of chord, sweep, twist and dihedral along the span, those starting points were varied so that values that provided satisfactory compromises between performance, stability and safety were found.

The first parameter to be selected was the chord distribution along the span. When selecting this parameter, typically there are two aspects that must be considered: the objective of elliptic lift distribution and the prevention of tip stall. Although, in this specific study, another aspect had to be taken into account: the minimum chords which ensures sufficient thickness so that the original UAS30 spar can be used.

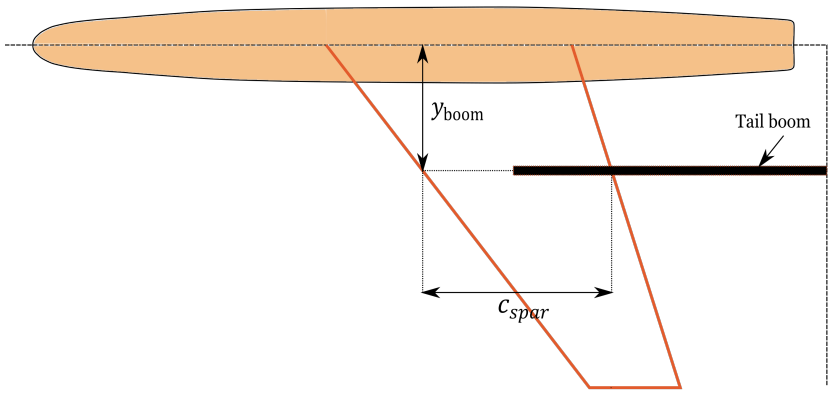

Figure 3.2: Spar limited wing chord parameters.

In order to obtain the minimum chord values which would allow the use of the original UAS30 spar, the first step was to determine the thickness of the wing sections where the spar will be present. To do that, the chord values of both the root and the section where the tail booms cross the wing were considered and their corresponding thicknesses were computed through the relative thickness of the original airfoil. Figure 3.2 helps understanding the parameters utilized in obtaining these values. The chord corresponding to the wing section where the tail booms cross (spar limit) was computed through Equation 3.14. This equation uses the difference of chords between the root and the tip of the wing in order to obtain the chord of any section along the span, in this case the section where the tail booms crosses the wing, y_{boom}. The obtained chord value was 0.578 m.

$$c_{spar} = c_r - \frac{y_{boom}(c_r - c_t)}{b/2} \quad (3.14)$$

With the chords of the root and section where the boom crosses the wing, the following step was to determine the thicknesses of those sections. The thickness values were calculated using Equation 3.15. The obtained values were: $t_{root} = 69.88$ mm and $t_{spar} = 57.52$ mm. The corresponding minimum chords were calculated rearranging Equation 3.15 and considering the relative thickness of the new airfoil and the calculated original absolute thickness values. The obtained minimum chord values for the root and boom interface section were respectively 687 mm and 565 mm.

$$t = (t/c)_{original}\, c_{original} \quad (3.15)$$

Having the minimum chord values that were possible to have in the two specific wing sections, four taper ratio values were considered: 0.25, 0.5, 0.75 and 1. Keeping the MAC

constant, the root, tip and boom interface chords provided by each taper ratio were calculated. The results can be seen in Table 3.8. Since only the taper values of 0.25 and 0.5 provided chord values that would satisfy the chord restrictions. they were the only two values passing to the analysis stage.

As stated in Section 2.1, tapered wings, *i.e*, wings whose ratio between the tip chord and the root chord is about 0.5 (see Section 1.2), are those capable of achieving lift distributions close to the elliptical, which is desirable. Despite the advantages in performance of tapered wings in the reduction of induced drag, their tendency to produce tip stall is a condition that should not be ignored in order to ensure flight safety. As so, the ideal taper ratio to utilize is the one that can approach the elliptical lift distribution or that provides good performance but without inducing tip stall.

Since both taper ratio and washout are typically used for the same purpose (approaching the elliptical lift distribution) they were selected together. A good relation between the two parameters can bring the best compromise between tip stall avoidance and induced drag reduction. As so, various possible combinations of the two parameters were analyzed and the combination that brought the most desirable results was selected. The washout angles considered were -1° and -2°, plus the -3° present in the original UAS30. The taper/washout combination that showed the most advantageous compromise between performance and lift distribution qualities was selected.

Table 3.8: Chord values corresponding to the considered taper ratio values.

λ	c_r **[mm]**	c_t **[mm]**	c_{spar} **[mm]**
0.25	764.355	191.089	566.747
0.5	687.919	343.960	569.355
0.75	607.353	455.515	555.013
1	535.049	535.049	535.049

The sweep, dihedral and incidence of the wing were the last parameters to be selected. In order to select the final sweep value, five different initial values were considered. Each value corresponded to a zero sweep about a given reference. The considered references for zero sweep were the leading edge, the quarter chord, the half chord, 75% of the chord and the trailing edge. In order to obtain the L.E offset values to input in XFLR5, Equation 3.16 was used. In this equation $\%_{ref}$ is the reference of zero sweep in terms of the chord. The sweep values about the quarter chord obtained using these references were: -2.18°, 0°, 2.18°, 4.36° and 6.52°.

$$x_{L.Eoffset} = \%_{ref}(c_r - c_t) \quad (3.16)$$

Having the sweep values that would be considered, the first step was to create an airplane for each sweep value. With each airplane created, the incidence angles were selected so that the C_L for C_m = 0 (trim condition) would correspond to the $C_{L_{design}}$ of 0.33 (see

Section 3.3). Then, and knowing that the sweep changes the wing center of gravity and the airplane neutral point, the following step was to evaluate the static margin range provided by each sweep value. Since the only values that presented static margins near or within the margin range were 0° and 2.18°, with static margins of respectively 9.7% and 14.6%, the other sweep angles were not considered for further analysis.

The dihedral value was selected together with the sweep. Since both affect lateral stability, the two values were selected aiming a good compromise between good stabilization of the lateral modes, having in mind that too much dihedral effect (mainly produced by the dihedral angle of the wing, although sweep also contributes to its effect) could produce dutch roll instabilities, which are unwanted. The dihedrals tested to each swept wing were: 0°, 0.5°, 1°, 1.5° and 2°.

After the parametric analyses were completed, the significant data were compared in order to obtain the best compromise of aerodynamic performance and stability of the UAS30 with the new wing design.

3.9 Stability Analysis

Besides the performance analysis of the airplane, it was also important to analyze its stability, since without stability, no matter how good a theoretical performance an airplane shows, it will not fly. The first step to ensure the longitudinal static stability of the airplane is to look at the graph that relates the pitching moment coefficient with the angle of attack and with the lift coefficient. As referred in Section 2.1, in the C_m *vs* C_L graph, there are two conditions that must be ensured. One of those conditions is a negative slope $\left(\frac{dC_m}{dC_L} < 0\right)$. The other condition is that the C_m for $C_L = 0$ must be positive. These two conditions allow the airplane to return to its equilibrium position after perturbations that throw its nose down or up. These conditions are highly influenced by the center of gravity position, and it is crucial to check this parameter for all the possible inertial conditions of the airplane. In this case, the only parameter that will change during the operation of the airplane is the fuel mass since the payload will not be a "droppable" load. So, to check the longitudinal static stability of the UAS30 it was necessary to perform an analysis of the airplane with full load and without any fuel.

With the static longitudinal stability prerequisites ensured, a dynamic stability analysis in XFLR5 could be made. In this type of analysis the flight modes for both longitudinal and lateral stability were calculated. Analyzing these modes allows the comprehension of how and how fast the airplane returns to its stable position after being disturbed.

XFLR5 allows the visualization of animations for each mode. In these animations it is possible to see the airplane's behavior for each mode in a given simulation time. XFLR5 also allows the visualization of the root locus and time response views for each mode.

Stability analyses to both the original UAS30 and the UAS30 with the new wing design were performed.

3.10 Final Performance Comparison

With all the parameters selected throughout the previous sections, it was then time to quantify the improvement that the changes in airfoil, chord, span, taper ratio, sweep, dihedral and incidence provide to the UAS30. A comparison between the original UAS30, the UAS30 with the new set of wings and the last one equipped with flaps was made in terms of performance, and the results allowed to evaluate the amount of improvement that the new wing design can provide to the UAS30 regarding the operational requirements.

The performance comparison of the two versions of the UAS30 was performed in two different stages:

1. Aerodynamic comparison;
2. Propulsive system modeling;
3. Performance estimation and comparison.

3.10.1 Aerodynamic Performance

In order to perform the first stage, the first step was to obtain the aerodynamic graphs of the airplane equipped with flaps. These graphs include the C_L/C_D *vs* V and T_r *vs* V. For that, different airplanes were created in XFLR5, each one using the FEMS1017 airfoil with a different deflection angle. The deflection angles considered were the same as in Section 3.5. Having the different airplanes created, XFLR5 airplane analysis were performed to each one of them following the same methodology as in Section 3.6. For each graph, an envelope containing the outer perimeter of the overlapping curves, for each flap deflection, was plotted. That envelope is the considered curve of the flapped airplane for all graphs.

3.10.2 Propulsive System Modeling

To make it possible to estimate the flight performance of the airplanes equipped with the different wings and then compare them, the first step was to create a model of the propulsive system of the UAS30. This was performed by modeling the engine, thus simulating its torque, throttle and output power for each rotational velocity. Then, recurring to Prop Selector software and the pitch and diameter data of the propeller to use, a relation between the speed and thrust provided by the propulsive (T_a) system was obtained.

The engine used in the UAS30 is the Desert Aircraft's DA-50 [48], but since not all the needed data to perform the modeling of this engine couldn't be found, it was decided to use the Corvid-50 [49] data, since it is a similar engine, for obtaining the P_o *vs* N curve. This engine is based on the DA-50 and has more available specifications. For that reason, it was considered a good alternative. The engine data used in this section can be seen in Table 3.9 and the remaining specifications can be found in Appendix A.2.

Table 3.9: Corvid-50 Data utilized in engine modeling.

Parameter	**Value**
N_{min} [rpm]	2000
N_{max} [rpm]	7000
P_{min} [W]	600
P_{max} [W]	2800

Having the data concerning the minimum and maximum values of engine rotational speed (N) and output power (P_o), the first step was to calculate the torque (Q) corresponding to each condition. This value can be computed from Equation 3.17, being that the rotational speed must be expressed in [rad/s] and the power in [W]. The torque is expressed in [N·m].

$$Q = \frac{P}{N} \quad (3.17)$$

There were two different approaches that were possible to take in order to model the power *vs* rotational speed: one was assuming constant torque with angular speed, while the other was assuming that the torque variation was linear with the angular speed. In this case, it was decided to assume the variation of torque, since it could provide more realistic results in the intermediate region of the range of power values.

In order to obtain a linear relation between the angular speed of the engine and the torque, the straight line equation obtained with two points was used. Equation 3.18 allows the calculation of any torque value within the interval defined by the torque corresponding to the engine's minimum and maximum angular speeds.

$$Q = \frac{Q_{max} - Q_{min}}{N_{max} - N_{min}} (N - N_{min}) + Q_{min} \quad (3.18)$$

Having the torque value for a given angular speed, it was then possible to compute the corresponding output power recurring once again to Equation 3.17.

Although the CORVID-50 was utilized to plot the P_o *vs* N, the power and maximum angular speed of the DA-50 were considered as the limit values for the next stage. These values

can be seen in Table 3.10. More information on the engine specifications can be found in Appendix A.1.

With the modeling of the engine performed, the next step was to use Prop Selector to find the available thrust values for each air speed value, for each considered propeller. The considered propellers were the ones recommended by the engine manufacturer and some higher pitch propellers available in [50]. These propellers were:

- 2-blade: 22x10", 23x10", 24x8", 22x12", 24x10", 23x12";
- 3-blade: 21x12", 22x14", 22x15", 22x16".

Table 3.10: DA-50 Data utilized in T_a *vs* V curve determination.

Parameter	Value
N_{min} [rpm]	1200
N_{max} [rpm]	7500
P [W]	3730

The interface of Prop Selector can be seen in Figure 3.3. For each propeller, the respective number of blades, diameter and pitch were inserted. The objective was for each airspeed value, to vary the RPM value so that the power absorbed would match the output power of the engine. When these values matched, the thrust value was stored. This procedure was performed for each propeller to airspeed values starting in 1 m/s and finishing in the maximum speed that would still allowed to match the RPM with the correct power without exceeding either the engine N_{max} or P_{max}. Note that the obtained T_a represents the values of thrust for only one throttle position.

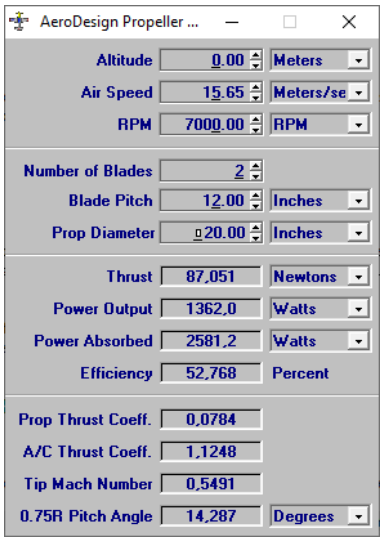

Figure 3.3: Prop Selector interface.

With the curves of available thrust *vs* speed for each propeller, the next step was to select the most advantageous propeller for the desired operation.

3.10.3 Performance Estimation and Comparison

Having the desired propeller selected, the T_a *vs* V curve of that propeller was considered from then on. For obtaining the aircrafts' performance, both the required thrust values of the aircraft and those of the available propeller thrust were also converted to power using Equation 3.19. This way it was possible to graphically determine V_{max}, V_{stall}, RC and γ parameters for each airplane.

$$P = TV \quad (3.19)$$

In order to determine the range and endurance values for a range of speeds, the propeller efficiency for those speeds had to be estimated and Equations 2.11-2.12 used. For that, the available thrust and the output power values previously determined from the propulsion system modeling were used. The propeller efficiency for the speed values considered in the T_a *vs* V model determination were calculated using Equation 3.20.

$$\eta_p = \frac{T_a \times V}{P_o} \quad (3.20)$$

Besides the propeller efficiency, also the SFC was necessary for the determination of the range and endurance. Once again, since the DA-50 doesn't have much data available, the CORVID-50 SFC was used. In the available datasheet there are different curves concerning the throttle position. In this case, as a way of simplifying being conservative, the SFC value was considered to be the one at 20 $\%$ of the throttle, at 3500 RPM (the highest SFC value) and constant for all speeds. The value is 2.72×10^{-6} N/W·s.

With the necessary engine and aerodynamic data determined (C_L/C_D *vs* V for range and $C_L^{\frac{3}{2}}/C_D$ *vs* V for endurance), the curves of range and endurance in terms of speed for the UAS30 with the new wing, with and without flaps, were plotted. The same methodology was applied to the original UAS30.

Chapter 4

Results/Discussion

4.1 Span and Chord Limit Values

After following the steps mentioned in Section 3.2 and plotting the functions F1, F2, F3 and F4, the span and chord limits for the new UAS30 wing can be seen in Figure 4.1. The values of the intersection points are (0.582; 5.44), (0.73; 3.43), (0.46; 6.14) and (0.58; 3.865). This means that the possible values for MAC are limited between 0.46 m and 0.73 m and for span are limited between 3.43 m and 6.14 m. The orange mark in Figure 4.1 is the region of possible solutions.

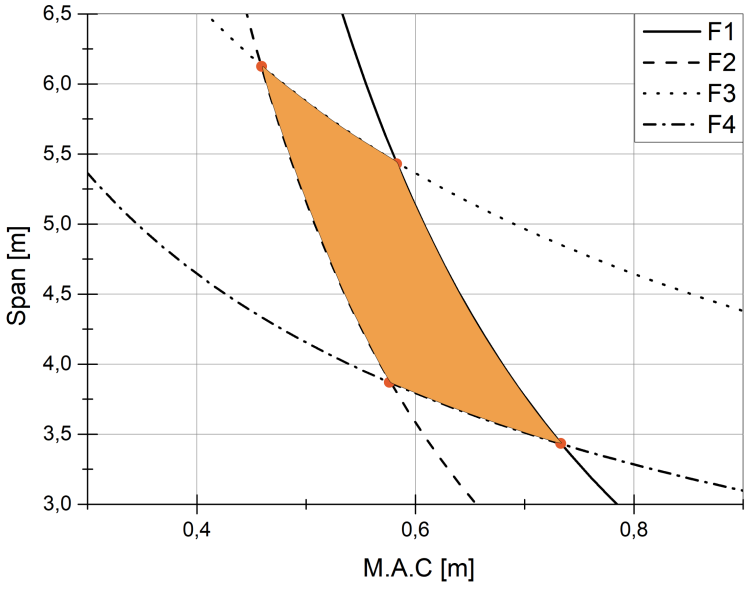

Figure 4.1: UAS30 possible span and chord values region.

4.2 UAS30 New Wings Final Airfoil

4.2.1 Reference Airfoil Selection

After analyzing the sample of airfoils through XFLR5 and running the scripts referred in Subsection 3.3.3, the 15 airfoils with the highest score can be seen in Table 4.1 along their geometrical features. Their partial and final scores can be seen in Table 4.3 and the

parameter values which provided those scores can be seen in Table 4.4. These airfoils correspond to the ones which the analysis results were more adequate regarding the considered weighted score method. The geometrical features of the original airfoil can be seen in Table 4.2.

Table 4.1: Pre-selected airfoils geometrical features.

Airfoil Name	**Thickness** (%)	**at** (%)	**Camber** (%)	**at** (%)
LOCKHEED C-141 BL761.11	10.51	40.84	1.80	48.55
LOCKHEED C-5A BL576	11.10	39.84	1.41	66.57
LOCKHEED C-141 BL610.61	10.76	39.44	1.54	50.75
RUTAN CANARD	11.63	40.14	2.08	42.04
LOCKHEED C-141 BL958.89	10	40.24	2.32	46.14
LOCKHEED C-5A BL488.2	11.5	39.94	1.22	70.47
LOCKHEED C-5A BL758.6	11.05	40.44	1.35	60.56
LOCKHEED C-5A BL1256	10.78	40.14	1.43	29.43
AH21	8.98	35.03	2.26	55.55
LOCKHEED L-188 TIP	12	39.34	2.66	52.45
RAE(NPL) 5212	11.95	37.14	1.83	68.17
GIII BL387	8.54	35.04	1.58	25.03
LOCKHEED C-5A BL0	13.12	41.04	0.74	83.38
S3024	9.85	31.04	3.53	42.85
BOEING 737 OUTBOARD	10.80	41.24	1.58	21.62

In terms of geometrical features, the relative thicknesses of the referred airfoils average a value of 10.84 %, the camber values average a value of 1.82 %. These values were considered expected since moderate thicknesses and low cambers are typically characteristic of low drag and lift coefficients airfoils, which is in agreement with the considered parameters of the WSM.

Table 4.2: Original UAS30 airfoil geometrical features.

Airfoil Name	**Thickness** (%)	**at** (%)	**Camber** (%)	**at** (%)
AH79-100C	9.94	30.83	6.70	49.15

Table 4.3: WSM scores summary table

	Scores										
Airfoil / Parameter	C_{l_0}	$C_{l_{max}}$	α_{stall}	$C_{d_{min}}$	C_l of $C_{d_{min}}$	$(C_l/C_d)_{max}$	C_l of $(C_l/C_d)_{max}$	$\left(C_l^{3/2}/C_d\right)_{max}$	C_l of $\left(C_l^{3/2}/C_d\right)_{max}$	C_m	Final Score
LOCKHEED C-141 BL761.11	3.8491	2.0582	4	3.6387	3.7308	2.1375	3.6779	1.3575	2.9981	3.0913	3.3898678
LOCKHEED C-5A BL576	3.7841	2.1882	4	3.7335	3.177	2.0794	3.8023	1.2622	2.905	3.0913	3.3772231
LOCKHEED C-141 BL610.61	3.7608	1.9518	4	3.7068	3.5721	1.8972	3.8215	1.3721	2.8521	3.1896	3.3770999
RUTAN CANARD	3.7879	2.3271	4	3.3544	3.9277	2.1814	3.5163	1.3977	3.9784	3.2879	3.3584461
LOCKHEED C-141 BL958.89	3.9707	2.402	4	3.4847	3.5842	2.1078	3.5186	1.5943	2.1812	2.9031	3.3525283
LOCKHEED C-5A BL488.2	3.7565	2.0496	4	3.7808	3.1246	1.9043	3.828	1.2145	2.7527	3.1194	3.3514222
LOCKHEED C-5A BL758.6	3.7829	2.0827	4	3.7009	3.177	1.9276	3.8055	1.246	2.8905	3.1166	3.3485126
LOCKHEED C-5A BL1256	3.7065	2.1873	4	3.3189	3.9176	1.533	3.8456	1.3086	2.8231	3.3862	3.3482795
AH21	3.9188	1.9518	3.1429	3.689	3.8563	2.9606	3.4955	1.8811	3.9555	2.6138	3.3368873
LOCKHEED L-188 TIP	3.9443	2.2631	4	3.464	3.6537	3.0033	3.1507	2.3112	3.3456	2.7528	3.3285632
RAE(NPL) 5212	3.9217	2.1971	4	3.6535	2.9736	1.7154	3.6478	1.2888	2.8323	2.9775	3.2857345
GIII BL387	3.5821	2.0588	3.5714	3.5202	3.6196	1.8168	3.661	1.3907	2.9167	3.6868	3.271618
LOCKHEED C-5A BL0	3.6015	1.8285	4	3.8401	2.8303	1.2146	4	1.0572	2.7372	3.3483	3.2709967
S3024	3.9316	1.9703	3.1429	3.6091	3.8794	3.0279	3.1447	2.4103	3.069	2.8567	3.2621651
BOEING 737 OUTBOARD	3.5975	1.8345	4	3.5617	3.2781	2.2879	3.4295	1.5278	3.5764	3.6222	3.2524111

Table 4.4: WSM parameter values summary table

	Parameter Values									
Airfoil / Parameter	C_{l_0}	$C_{l_{max}}$	α_{stall}	$C_{d_{min}}$	C_l of $C_{d_{min}}$	$(C_l/C_d)_{max}$	C_l of $(C_l/C_d)_{max}$	$\left(C_l^{3/2}/C_d\right)_{max}$	C_l of $\left(C_l^{3/2}/C_d\right)_{max}$	C_m
LOCKHEED C-141 BL761.11	0.2627	1.3624	15	0.00452	0.2627	88.23741007	0.4906	65.48779689	0.946	-0.0647
LOCKHEED C-5A BL576	0.2339	1.4032	15	0.0042	0.1263	86.34387352	0.4369	61.60745518	0.9826	-0.0647
LOCKHEED C-141 BL610.61	0.2236	1.329	15	0.00429	0.2236	80.41275797	0.4286	66.08181016	1.0034	-0.0577
RUTAN CANARD	0.2356	1.4468	15	0.00548	0.3488	89.664	0.5604	67.12235302	0.5604	-0.0507
LOCKHEED C-141 BL958.89	0.3434	1.4703	15	0.00504	0.4334	87.2698908	0.5594	75.12667838	1.2673	-0.0781
LOCKHEED C-5A BL488.2	0.2217	1.3597	15	0.00404	0.1134	80.64393939	0.4258	59.66494511	1.0425	-0.0627
LOCKHEED C-5A BL758.6	0.2334	1.3701	15	0.00431	0.1263	81.40186916	0.4355	60.94922049	0.9883	-0.0629
LOCKHEED C-5A BL1256	0.1995	1.4029	15	0.0056	0.3087	68.55737705	0.4182	63.49577258	1.0148	-0.0437
AH21	0.3664	1.329	13	0.00435	0.3664	115.030303	0.5694	86.80025385	0.5694	-0.0987
LOCKHEED L-188 TIP	0.3551	1.4267	15	0.00511	0.2437	116.4181524	0.7183	104.3059032	0.8093	-0.0888
RAE(NPL) 5212	0.2949	1.406	15	0.00447	0.0762	74.49704142	0.5036	62.69093419	1.0112	-0.0728
GIII BL387	0.1444	1.3626	14	0.00492	0.2353	77.796875	0.4979	66.8405094	0.978	-0.0223
LOCKHEED C-5A BL0	0.153	1.2903	15	0.00384	0.0409	58.19536424	0.3515	53.26283176	1.0486	-0.0464
S3024	0.3607	1.3348	13	0.00462	0.3607	117.2195122	0.7209	108.3375355	0.9181	-0.0814
BOEING 737 OUTBOARD	0.1512	1.2922	15	0.00478	0.1512	93.13084112	0.5979	72.41760587	0.7185	-0.0269

The C_l/C_d value considered for the comparison of the 15 pre-selected airfoils was 60. The airfoils with the highest C_{l_2}/C_{l_1} ratios were the LOCKHEED C-141 BL610.61, the S3024 and the AH21, with the respective values of 3.95, 3.88 and 3.79. In comparison, the original UAS30 airfoil obtained a ratio value of 2.85, way below the ”winners”. In Figure 4.2, the C_l/C_d *vs* C_l curves of the four airfoils can be seen. Comparing these curves, it is well evident that, although the original UAS30 airfoil has a noticeably higher value of $(C_l/C_d)_{max}$ than the other airfoils, the high magnitude of this parameter is not well-located, existing only for high C_l values. This translates in extremely good performances over a small range of conditions and poor performances at any lift coefficient outside that peak. On the other hand, the remaining airfoils have lower $(C_l/C_d)_{max}$ values, but the curve is noticeably wider over a wider range number of C_l values, which generally translates in good performances also for a wider range of operation conditions. This feature characterizes a more balanced and versatile airfoil, what is beneficial for the new wing of the UAS30, since it can provide good performances not only at lower lift coefficients, but also at lift coefficients that are many times higher. This covers a large range of speed and load conditions.

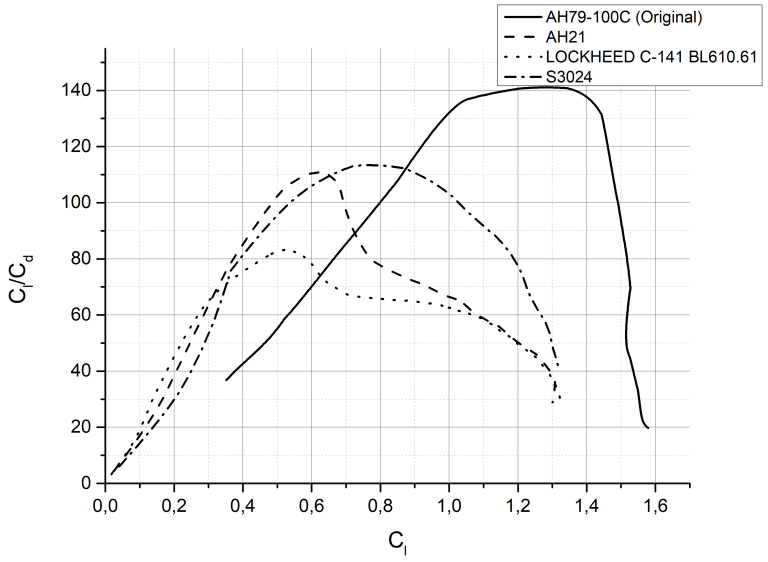

Figure 4.2: C_l/C_d *vs* C_l curves of the in-comparison airfoils: $Re\sqrt{C_L} = 5.12 \times 10^5$.

Having defined the top three airfoils in what concerns to the lift to drag ratio *vs* C_l, the airplanes utilizing them were then created. The minimum mean aerodynamic chord values of the wings corresponding to each airfoil such that the existing spar can be used are: 0.55 m for the original wing, 0.608 m for the AH21, 0.506 m for the LOCKHEED C-141 BL610.61 and 0.554 m for the S3024. Since this stage concerned only the airfoil and not other geometrical parameters, the limits of chord and span obtained previously were not considered.

With the analysis performed for each one of the wings, the graphs referred in Subsection 3.3.4 were observed. The graph that relates the required thrust with the speed can be seen in Figure 4.3. The arbitrary value chosen for T_a was 15 N. Considering this value,

the highest speeds for each airfoil are respectively: 24.94 m/s for the AH79-100C original wing, 34.74 m/s for the AH21, 40.83 m/s for the LOCKHEED C-141 BL610.61, and 33.22 m/s for the S3024. The minimum speeds (determined by considering the $C_{L_{max}}$ values) are, in the same order, 11 m/s, 11.32 m/s, 12.1 m/s and 11.7 m/s. With these values it is possible to conclude that the original UAS30 wing does manage to achieve the lowest speeds, which can be beneficial in terms of stall conditions, although the other airfoils can achieve minimum speeds relatively close to it. It is on the fast side of the speeds that the differences are clearer. The AH79-100C airfoil is way below the other airfoils, which means that it is impossible for this airfoil to achieve nearly as fast speeds as the other airfoils for a given constant thrust. On the other hand, the LOCKHEED C-141 BL610.61 is the airfoil that, besides having the highest minimum speed, which can be solved by using an adequate flap, is the airfoil which can achieve the higher speeds for the arbitrated thrust. This translates in an airplane that in addition to being able to fly with higher performances at higher speeds, does not totally compromise the operation at lower speeds.

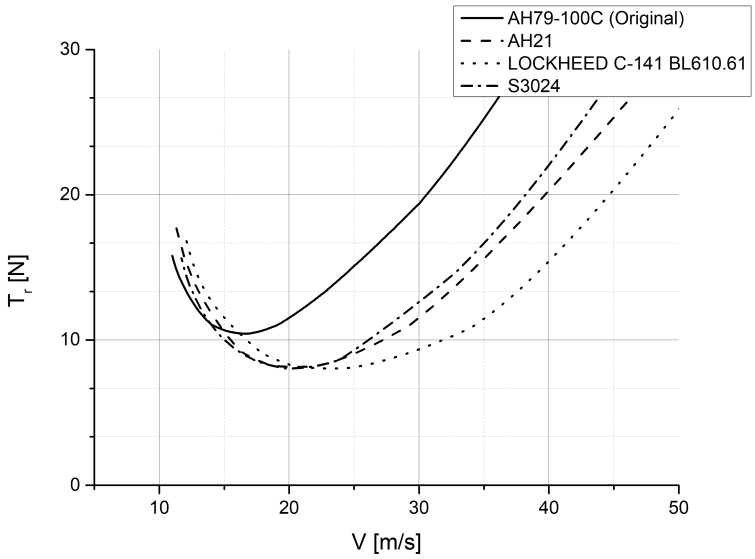

Figure 4.3: T_r *vs* V curves of the airplanes using the in-comparison airfoils.

The graph that relates the airplanes' aerodynamic efficiency with the speed is represented in Figure 4.4. Observing the graph it is possible to conclude that the AH79-100C has an higher C_L/C_D value than the other airfoils over a really small region of speeds, after that, all the remaining airfoils begin to have noticeably higher aerodynamic efficiency for the whole range of speeds and by a large margin. This, once more, depicts the lack of performance of the UAS30 original wings at higher speeds. The airplane exhibiting the most advantageous curve is the one equipped with the LOCKHEED C-141 BL610.61. This airfoil, despite having a slightly worse performance than the others in the lower speeds region, rapidly recovers and stays well above any other curve.

With the methodology applied to select the airfoil for the UAS30 new wings, it was concluded that the LOCKHEED C-141 BL610.61 was the solution, among the considered ones,

that could allow the best performance for the design requirements of the UAS30 new wings. It is the airfoil that is capable to produce the fastest aircraft among the compared ones and, as so, it was considered the best solution to hold as the reference airfoil. The geometry of the airfoil can be seen in Figure 4.5.

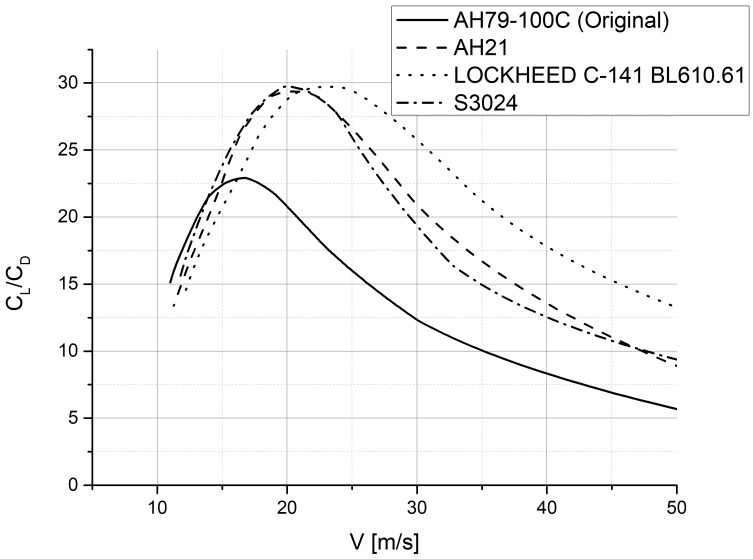

Figure 4.4: C_L/C_D *vs* V curves of the airplanes using the in-comparison airfoils.

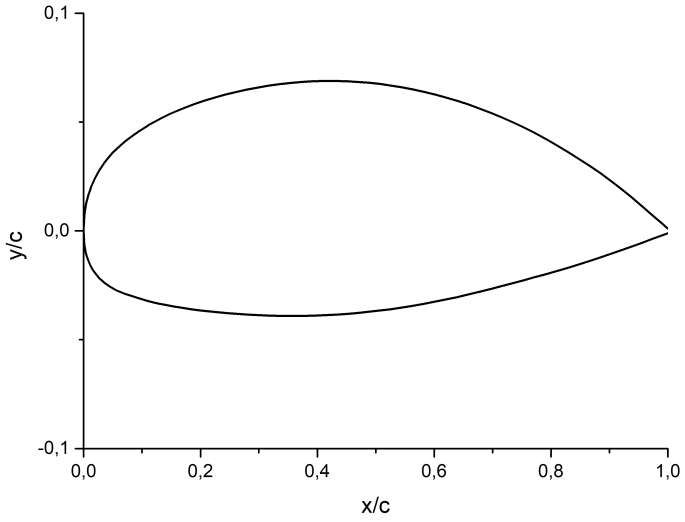

Figure 4.5: LOCKHEED C-141 BL610.61 airfoil geometry.

4.2.2 Airfoil Improvement

After applying the methodology referred in Section 3.4, a new airfoil (FEMS1017) was obtained. A comparison between the geometries of the obtained and the reference airfoil (LOCKHEED BL610.61) can be made by observing Figure 4.6, and the summary of their

geometrical specifications is presented in Table 4.5. The differences between the two geometries are quite evident: On the upper surface the FEMS1017 is moderately thicker between sensibly 5% and 40% of the chord, having a similar thickness to the LOCKHEED BL610.61 for the remaining percentages of the chord. On the lower surface, the new airfoil is considerably thinner between 15% and 90% of the chord. All in all, the thickness of the FEMS1017 exhibits a decrease of 5.48% (from 10.76 to 10.17) and the camber an increase of 35.7% (from 1.56 to 2.09).

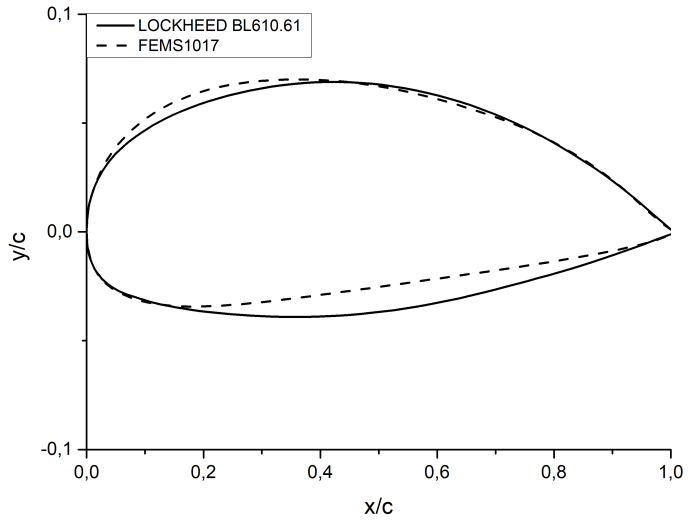

Figure 4.6: LOCKHEED BL610.61 and FEMS1017 geometries comparison.

The transition curves of both airfoils can be seen in Figure 4.7. In the upper surface it is clear that the FEMS1017 airfoil has, for the whole range of values of C_l, further aft transitions than the LOCKHEED BL610.61. Additionally, the slope of the xtr/c *vs* C_l curve of the FEMS1017 is also less steep for the most part of C_l values, having only a steeper slope in the regions of C_l values between 0.1 and 0.2 and between 0.55 and 0.75. The differences between the transition curves for the lower surfaces are also evident. The laminar boundary layer of the LOCKHEED BL610.61 is more extensive in the range of C_l values between 0.1 and 0.3, being the FEMS1017 laminar boundary layer more extensive for the remaining upper values of C_l.

Table 4.5: LOCKHEED BL610.61 and FEMS1017 airfoil geometrical features.

Airfoil Name	**Thickness (%)**	**at (%)**	**Camber (%)**	**at (%)**
LOCKHEED BL610.61	10.76	39.44	1.54	50.75
FEMS1017	10.17	28.60	2.09	47

Figure 4.9 shows the drag polars of both airfoils. As it is possible to see, the polar of the FEMS1017 presents the most advantageous shape for almost the full range of C_l values, where the curve is clearly moved to the left, exhibiting lower values of C_d for the same values of C_l. The only range where that does not happen is between the C_l values of 0.1 and 0.28, where in the transition curves for the lower surface it has been concluded that

the LOCKHEED BL610.61 also had a more desirable shape, proving the clear relation between the transition curves and the drag polar shape. Nevertheless, the new wings of UAS30 are not expected to reach cruise speeds with C_l values lower than 0.28. The values of $C_{d_{min}}$ are also very close in both airfoils and the C_l values where it occurs are sensibly 0.2 for the LOCKHEED BL610.61 and 0.28 for the FEMS1017, becoming closer to the calculated $C_{L_{design}}$ of 0.33.

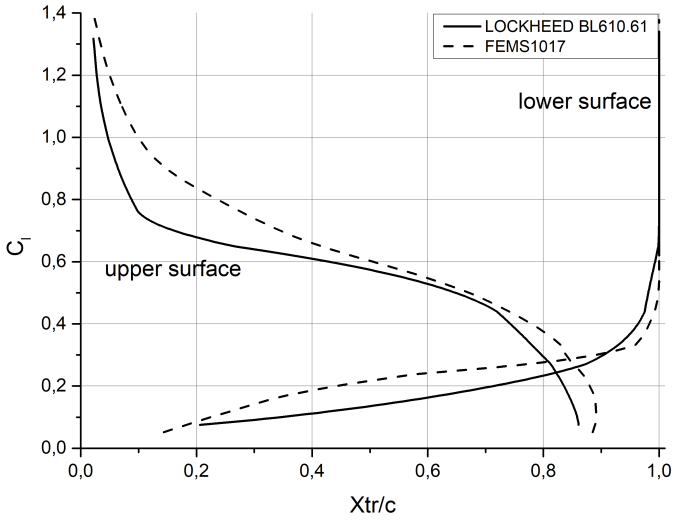

Figure 4.7: LOCKHEED BL610.61 and FEMS1017 transition curves: $Re\sqrt{C_L} = 5.12 \times 10^5$.

Other important graph to refer is the one showing the C_l *vs* α curves of the two airfoils. This graph can be seen in Figure 4.8. Observing the curves, it is possible to conclude that the FEMS1017 airfoil presents an absolute improvement: Not only it reaches higher C_l values, increasing the $C_{l_{max}}$ value from 1.32 to 1.39, meaning an improvement of 5.3%, but it also presents higher values of lift coefficients for the same angles of attack and an increase of 17.6% in the lift coefficient for zero angle of attack (0.22 to 0.26). The stall also shows to be less abrupt in the FEMS1017.

Finally, the last graph to look at is the one that relates the aerodynamic efficiency of the airfoil with the lift coefficient. Figure 4.10 shows the curves of the two airfoils. The FEMS1017 exhibits a clear improvement in practically the whole range of operations of the airfoils except in the C_l values region between 0.1 and 0.27 where the two airfoils have similar curves, with the LOCKHEED BL610.61 being slightly better. From 0.27 onwards, the performance of the FEMS1017 is overwhelmingly higher, exhibiting a maximum increase in the aerodynamic efficiency of 21.2% comparing to the LOCKHEED BL610.10 at C_l=0.8, where the discrepancy is more pronounced. The value of $(C_l/C_d)_{max}$ has also increased slightly from 83.27 to 86.22, with the plus that this parameter, in the FEMS1017 covers a wider range of C_l values. In the C_{l_2}/C_{l_1} for a C_l/C_d value of 60, that defines the overall score of the airfoil according to what was in the previous reference airfoil selection stage, we get 4.68 for the FEMS1017 and 3.95 for the LOCKHEED C-141 BL610.61, mean-

ing an improvement of 18.4% for the new airfoil. This gives a clear picture of the increase in performance of the new airfoil when compared to the reference one.

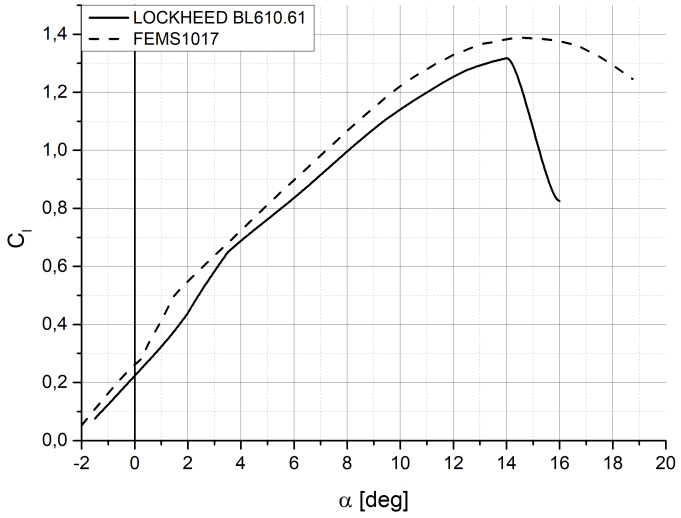

Figure 4.8: LOCKHEED BL610.61 and FEMS1017 C_l *vs* α curves: $Re\sqrt{C_L} = 5.12 \times 10^5$.

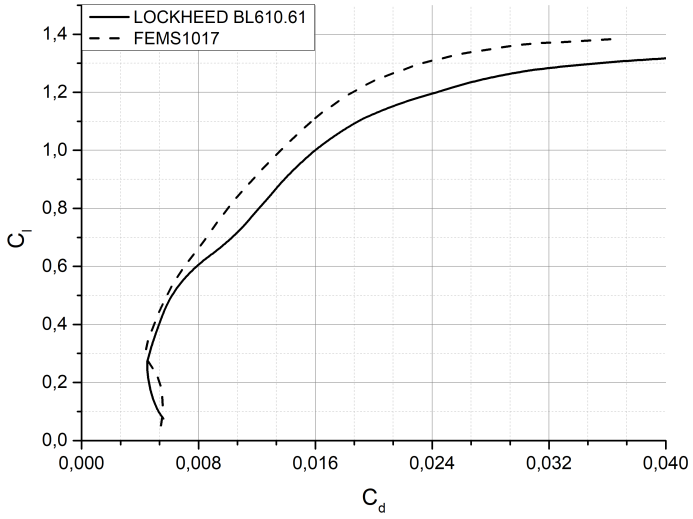

Figure 4.9: LOCKHEED BL610.61 and FEMS1017 drag polars: $Re\sqrt{C_L} = 5.12 \times 10^5$.

With this set of results presented, it is possible to state that the improvement of the LOCKHEED BL610.61 through the manipulation of the transition curves has proven to be successful, since it generated an airfoil with better features than the reference one for almost its whole range of operation without practically sacrificing any point of the airfoil performance. Although the thickness of the new airfoil is lower, which could be negative in terms of structure weight addition, it does not entail problems since it is still slightly thicker than the UAS30 original airfoil (AH 79-100C), meaning that the original spar can still be used without involving a wing structure weight increase.

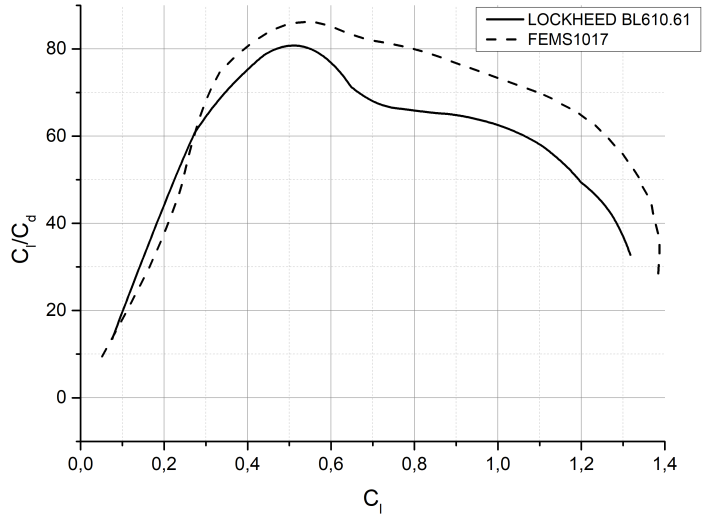

Figure 4.10: LOCKHEED BL610.61 and FEMS1017 $^{C_l}/_{C_d}$ *vs* C_l curves: $Re\sqrt{C_L} = 5.12 \times 10^5$.

4.3 Cruise Flap Implementation Study

For the selection of the x/c position of the hinge of the flap, the studied percentages of the chord were: 70%, 75%, 80% and 85%. To check the $C_{l_{max}}$ improvement for each x/c position of the flap hinge, the maximum deflection angle that would still provide an increase of maximum lift coefficient was determined, and its equivalent $C_{l_{max}}$ was the one considered for comparison. The flap deflection angles chosen to be analyzed concerning the other parameters to study were: -4° ,-2°, 2°, 4° and 8°. Note that negative angles mean upward deflections while positive angles mean downward deflections. With the referred angles analyzed for each hinge x/c location, the three different graphs were compared and the results can be seen in Figure 4.11 along with their respective improvement percentages in comparison with the unflapped FEMS1017 airfoil.

The first parameter analyzed regarding the x/c position of the hinge influence was $C_{l_{max}}$. The flap deflection angles that provide the maximum increase in lift coefficient for each x/c position of the hinge are: 46° for 70%, 44° for 75%, 46° for 80% and 38° for 85%. The comparison between the corresponding $C_{l_{max}}$ provided by these deflection angles can be seen in Figure 4.11a. Observing the graph, it is possible to conclude that the achieved $C_{l_{max}}$ is higher the lower the chord percentage corresponding to the x/c position of the hinge. With the flap hinge located at 70% of the chord, the $C_{l_{max}}$ obtained is close to 1.9, located at 75% is sensibly 1.85, at 80% is 1.81 and at 85% the value is 1.75. These values correspond to percentages of improvement in relation to the maximum lift coefficient of the clean airfoil of respectively 36.4%, 32.9%, 30.4% and 25.7%, which means that all the studied x/c positions for the flap hinge, even the ones whose results are not as significant, show clear improvements in terms of maximum lift coefficient in relation to the unflapped FEMS1017 airfoil.

In the maximum aerodynamic efficiency *vs* x/c position of the hinge graph, present in Figure 4.11b, the position that provides the best result is also 70% with a value of $(C_l/C_d)_{max}$ of 121.8, which translates into an increase of 41.3% when compared with the value of the clean airfoil. The least advantageous position is at 85% of the chord, presenting a value of $(C_l/C_d)_{max}$ of 112.7 (increase of 30.7%) which, once again, still ensures a good improvement.

The results of the comparison of the C_{l_2}/C_{l_1} ratio for the various x/c positions, presented in Figure 4.11c shows that for 85% of the chord position, the performance of the flap is higher than for the other positions. For this condition, the value of this parameter is 5.23, meaning an improvement of 11.66% when compared to the value of 4.68 provided by the clean airfoil. The worst x/c position for the hinge with respect to this parameter is at 70% of the chord, showing an improvement of only 4.7% of the unflapped airfoil value, being the other two positions, once again, between the performances of these two, with values of 4.97 for 75% and 5.1% for 80%. The corresponding improvement percentages are respectively 6.24% and 8.82% of the value of the FEMS1017 clean airfoil value.

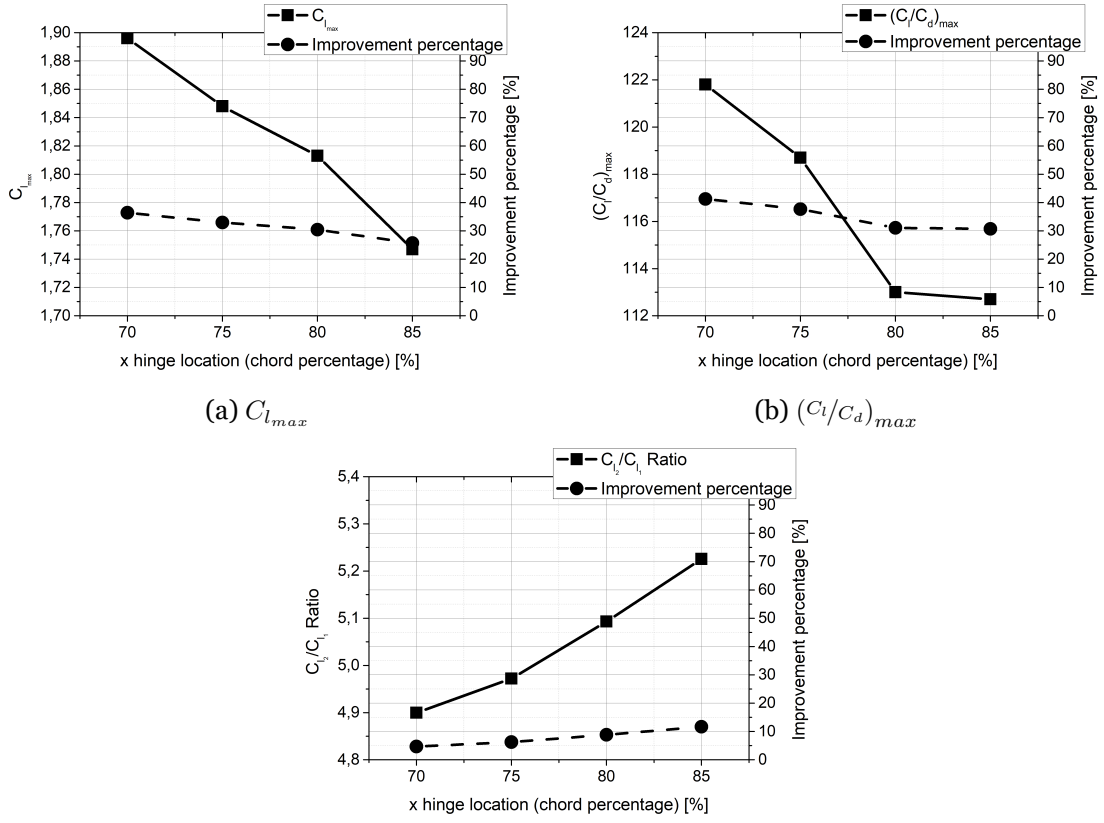

(a) $C_{l_{max}}$

(b) $(C_l/C_d)_{max}$

(c) C_{l_2}/C_{l_1}

Figure 4.11: Flap hinge x/c position study for various δ values: $Re\sqrt{C_L} = 5.12 \times 10^5$.

After the comparison between the performance indicators of the analyzed flap deflection angles in the considered x/c hinge positions, it can be concluded that having the flap hinge positioned at 70% of the chord provides better results than the other positions concerning the $C_{l_{max}}$ and the $(C_l/C_d)_{max}$ parameters. On the other hand, the position of the hinge that

shows the best behavior when it comes to the C_{l_2}/C_{l_1} ratio is at 85% of the chord. Now, if all parameters had the same importance, the most obvious chord percentage to position the flap hinge would be 75%, however, as it has been regular during airfoil comparisons in this dissertation, the greatest importance is given to the overall performance of the airfoil for its whole operation. Thus, and since the C_{l_2}/C_{l_1} ratio has been used as the way to quantify that quality, and since for this position the other parameters also show good improvements in comparison with the clean airfoil, it has been decided that the most advantageous position for the hinge would be at 85% of the chord. A good way to visualize how much wider the envelope corresponding to the hinge position at 85% of the chord is relative to the others is through the graphs present in Figure 4.12. Considering a C_l/C_d of 60, it is clear that this x/c = 85% position produces a much wider envelope than the other positions, not significantly harming the $(C_l/C_d)_{max}$ parameter.

With the value of the position for the flap hinge selected, the flapped airfoils were defined for in depth analysis. The deflection angles selected to analyze were: -6°, -4°. -2°, 2°, 4°, 6°, 8°, 10° and 12°. Having all the flapped airfoils stored, the XFoil direct analyses were performed.

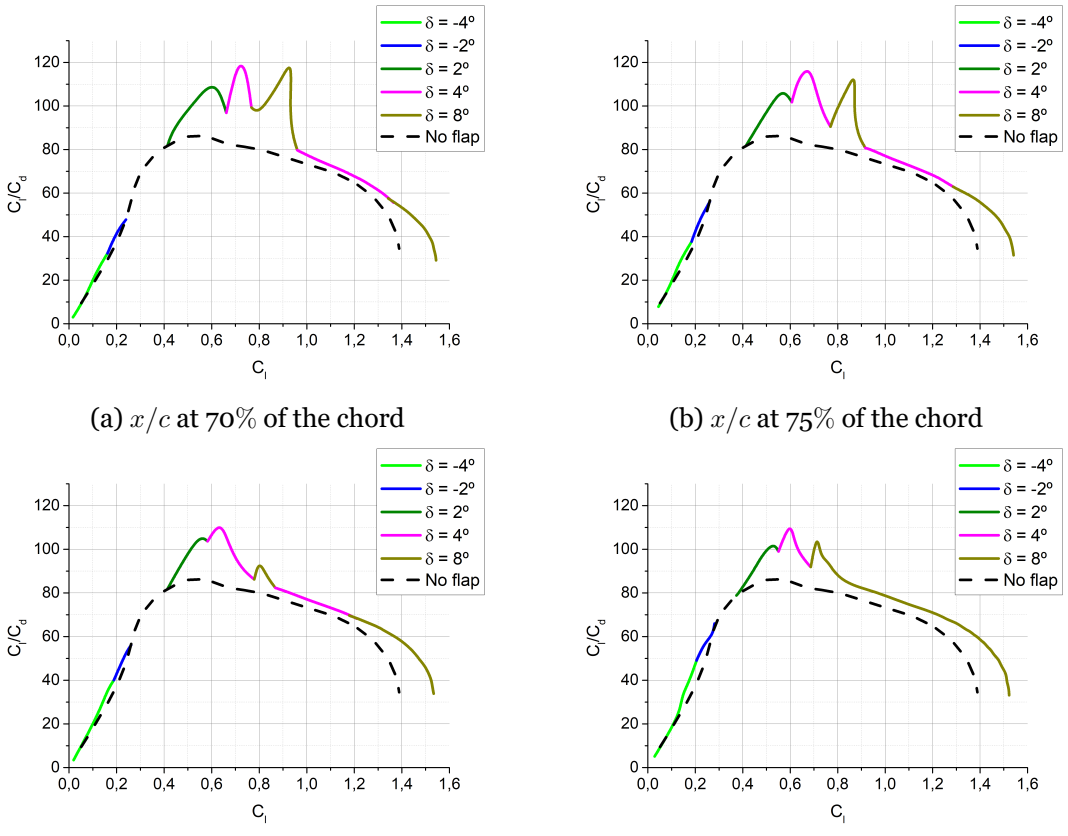

(a) x/c at 70% of the chord

(b) x/c at 75% of the chord

(c) x/c at 80% of the chord

(d) x/c at 85% of the chord

Figure 4.12: C_l/C_d *vs* C_l envelope for various flap hinge x/c position values: $Re\sqrt{C_L} = 5.12 \times 10^5$.

The resulting C_l *vs* α curves for the various flap deflection angles can be seen in Figure 4.13. In this graph it is possible to verify the direct relation between the deflection angle and the $C_{l_{max}}$ value. The higher the angle, the higher the maximum lift coefficient. Also,

it is possible to observe that by increasing the deflection angle, there is a decrease in the α_{stall} value. The higher value of $C_{l_{max}}$ is obtained with a deflection of $\delta = 38°$, achieving a value of 1.75, corresponding to an α_{stall} of 8.5°.

In Figure 4.14, the curves of the C_l *vs* C_d for the various flap deflection angles are shown. As it is possible to observe, the negative deflections provide decreases in drag coefficient in the lower C_l region, while the positive deflections provide decrease in drag coefficient for higher values of C_l. Figure 4.15 shows the C_l *vs* C_d envelope for the flapped airfoil along with the clean C_l *vs* C_d curve for comparison. By the observation of this graph, it is clear that the flap implementation can provide a drag coefficient reduction for almost the whole range of lift coefficients of the airfoil, except in the region of C_l near 0.33 where no deflection proves to be the most advantageous, which is expected since the improving of the airfoil was performed having that region as the reference $C_{l_{design}}$.

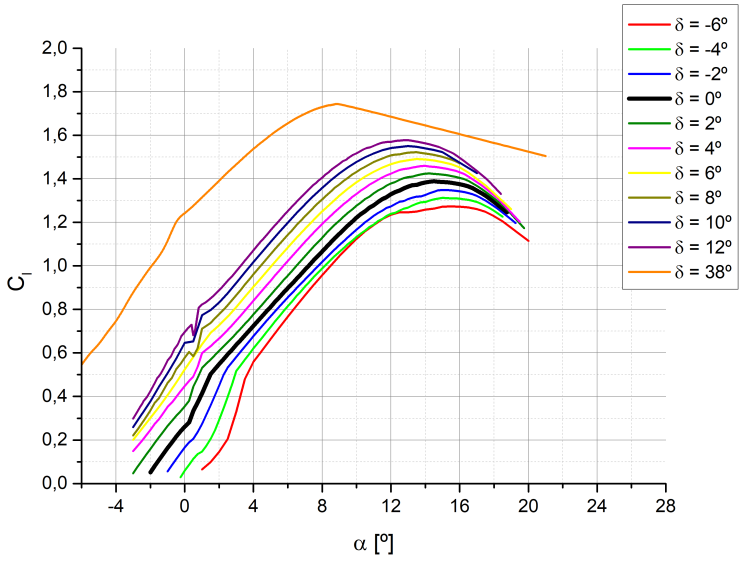

Figure 4.13: C_l *vs* α curves for various flap deflection angles: $Re\sqrt{C_L} = 5.12 \times 10^5$.

The curves of C_l/C_d *vs* C_l for the different flap deflections are shown in Figure 4.16, and the corresponding envelope is shown in Figure 4.17. In these graphs it is possible to observe an improvement in the overall efficiency of the airfoil for the whole range of C_l values. In the lower region of lift coefficients the improvement is not very expressive until the C_l value reaches around 0.4, where the application of the flap begins to improve significantly the C_l/C_d values. The C_{l_2}/C_{l_1} for a C_l/C_d of 60 for the flapped airfoil, in this conditions is 5.3 meaning an increase in this parameter of 13.27% relative to the unflapped FEMS1017 airfoil value (4.68). The value of maximum aerodynamic efficiency also presents an increase from 86.22 to 112.7 (30.7%), occurring at the lift coefficient value of 0.6 for a flap deflection of 4°.

The results of the cruise flap implementation study for the UAS30 show that it can have a beneficial influence in the performance of the FEMS1017 airfoil and consequently of the UAS30 new wings, as long as it is used in such a way that the correct deflection angles can

be applied for the exact corresponding C_l range (see Figures 4.15-4.17). This is because otherwise the performance can be severely affected, since each deflection angle of the flap shows improvements only for a limited lift coefficient range, having severe performance deterioration for the remaining values of C_l (see Figures 4.13-4.16), harming the performance of the airfoil and, subsequently, of the airplane.

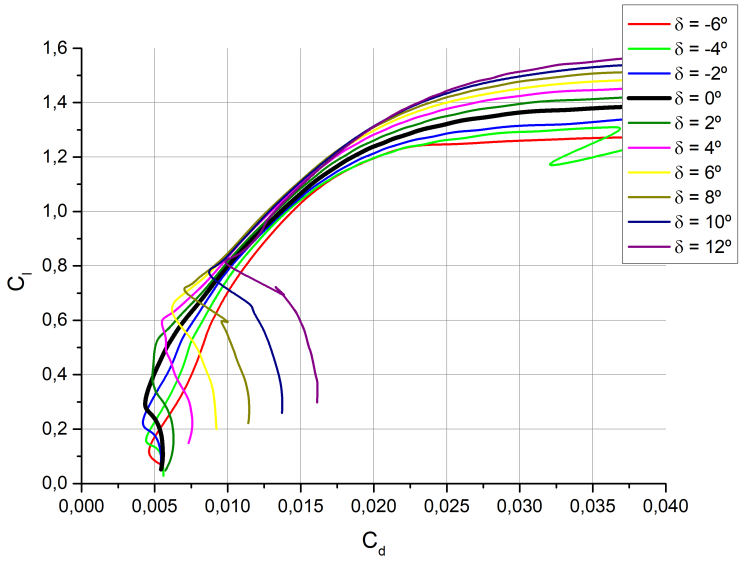

Figure 4.14: C_l *vs* C_d curves for various flap deflection angles: $Re\sqrt{C_L} = 5.12 \times 10^5$.

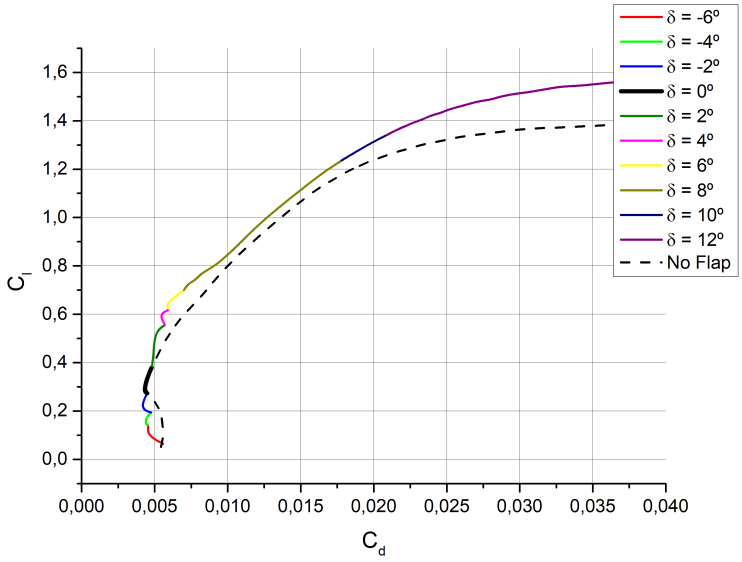

Figure 4.15: C_l *vs* C_d envelope of the flapped FEMS1017: $Re\sqrt{C_L} = 5.12 \times 10^5$.

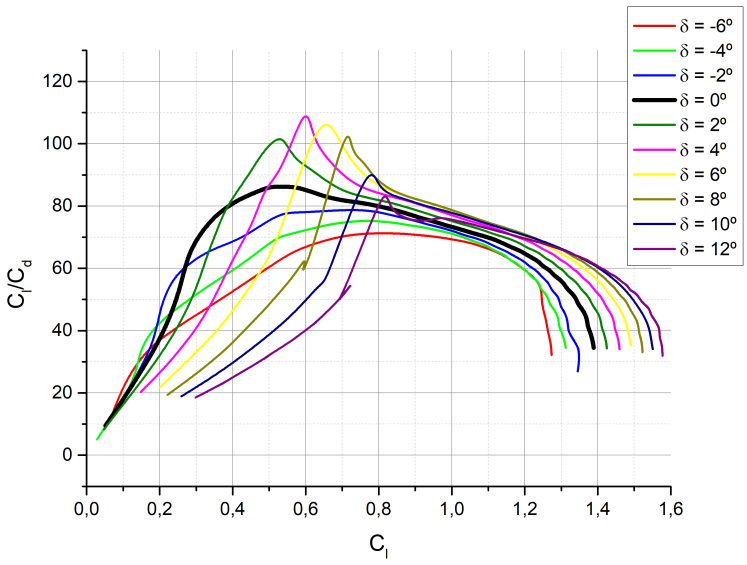

Figure 4.16: $^{C_l}/_{C_d}$ *vs* C_l curves for various flap deflection angles: $Re\sqrt{C_L} = 5.12 \times 10^5$.

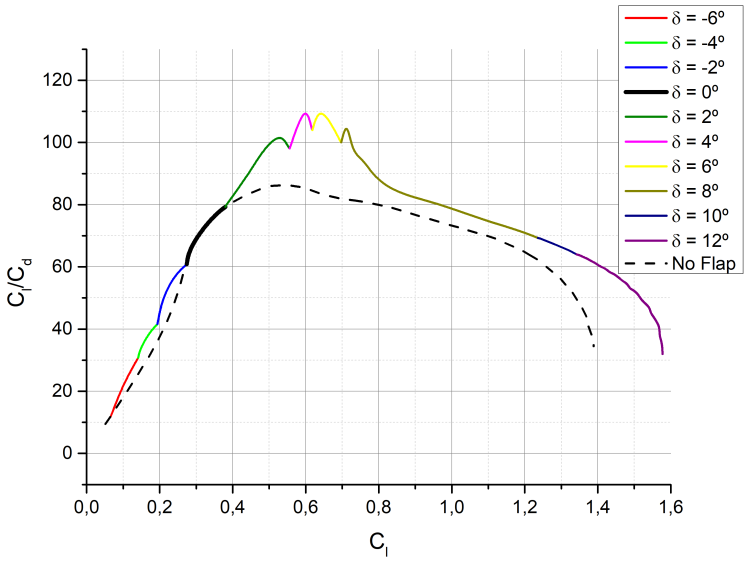

Figure 4.17: $^{C_l}/_{C_d}$ *vs* C_l envelope of the flapped FEMS1017: $Re\sqrt{C_L} = 5.12 \times 10^5$.

4.4 Initial Aerodynamic Estimation

In terms of performance, the resulting graphs of the airplane analysis performed for the original UAS30 and the UAS30 with the new airfoil, can be seen in Figures 4.18-4.19. It is important to mention that the flaps were not considered for the following sections, up until Section 4.8.

In the graph present in Figure 4.18 it is possible to observe the curves of the aerodynamic efficiency of both airplanes related to its speed values. Up to a speed of approximately 18 m/s, the original UAS30 exhibits slightly higher values of aerodynamic efficiency but,

beyond that point, the performance of the UAS30 with the new airfoil is better in an expressive way. For the objectives of the dissertation this is advantageous, since the main goal is to have an airplane that can fly efficiently at higher speeds.

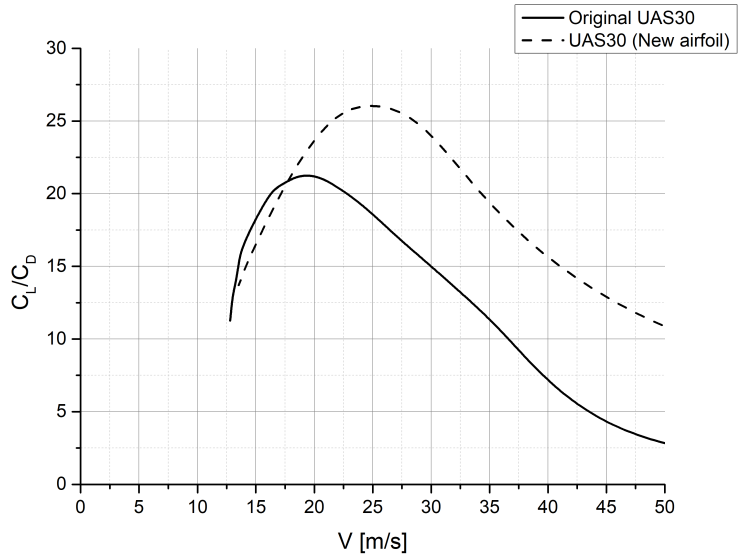

Figure 4.18: C_L/C_D *vs* V curves of the original UAS30 and the UAS30 with the new airfoil.

When it comes to the graph that relates the required thrust with the speed shown in Figure 4.19, it is also quite evident that the UAS30 with the new airfoil exhibits the most advantageous curve. Until approximately 17.74 m/s, the original UAS30 requires slightly less thrust for a given speed when compared to the UAS30 with the new airfoil, but beyond that speed the required thrust for any given speed is clearly lower, which is also positive in an airplane whose goal is, once again, to being able to cruise faster. Considering the arbitrary value of constant available thrust of, for instance, 20 N, the maximum speed of the original UAS30 is 26.88 m/s and for the airplane with the new airfoil it is 37.47 m/s. The stall speeds are 12.8 m/s for the original UAS30 and 13.6 m/s for the UAS30 using the new airfoil. The increase of 6.25% in the stall speed is a downside of the new airfoil, since the lower the minimum speed, the safer the operation at take-off and landing. Nevertheless, since flaps usage has proven to be advantageous in Section 4.3, this downside could be minimized or even eliminated by their implementation. On the other hand, the increase of nearly 39.4% in top speed is a really significant improvement in the aircraft performance.

With performance in depth analyses performed to the original UAS30 and the UAS30 with the new airfoil, it was then possible to have a reference point for further improvement. The results of this subsection also allows to conclude that, only by changing the airfoil, the performance of the UAS30 regarding the dissertation objectives had already improved significantly.

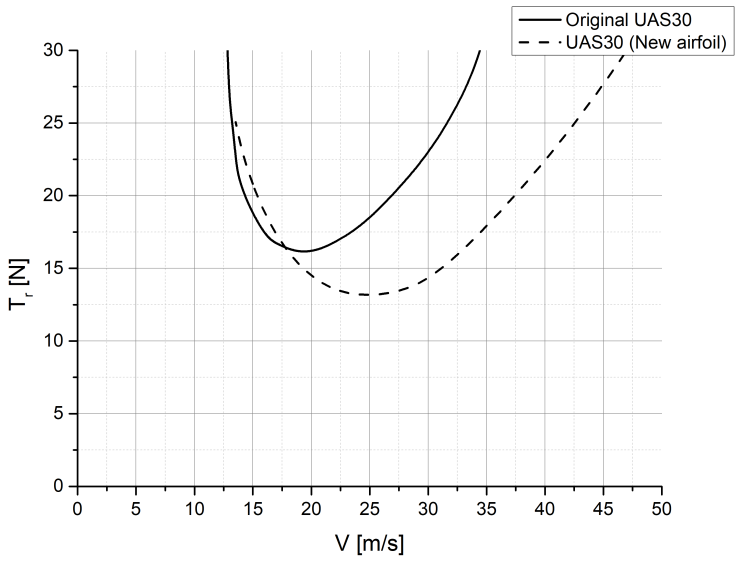

Figure 4.19: T_r *vs* V curves of the original UAS30 and the UAS30 with the new airfoil.

4.5 New Wing Span and Chord Final Values

With the analysis concerning the different span values performed, the resulting graphs can be seen in Figures 4.20 - 4.21. Figure 4.20 contains the graph concerning the aerodynamic efficiency curves for each span value. Observing those curves, it is easy to understand a direct relation between the span value and the $(C_L/C_D)_{max}$: The higher the span, the higher the value of the maximum aerodynamic efficiency. This is due to the increase in aspect ratio by increasing the span without changing the mean aerodynamic chord, that helps decreasing the tip vortex effect in the drag coefficient of the airplane. Considering an arbitrary fixed value of C_L/C_D (20 per example) and computing a C_{L_2}/C_{L_1} ratio for each curve, it is easily visible that the higher the span, the higher this ratio would be. That also shows how increasing the span can improve the performance of the UAS30.

In the graph where are represented the T_r *vs* V curves for each span value, visible in Figure 4.21, a relation between the span increase and the required thrust in function of speed is also observable: As the span increases, the required thrust shows decreases in the low speed region and increases in the high speed region of the envelope. This is due to the decrease in the wing loading as the span increases. The stall speed of the original UAS30 is also represented for comparison. Regarding the stall speeds that the different spans provide, it is possible to conclude that the lower spans harm significantly this parameter.

After observing the two graphs, it is possible to conclude that higher span values provide better performances for higher C_L values and lower speeds, while shorter spans benefit the operation at lower C_L values and higher speeds. It is important to have in mind that the design lift coefficient is relatively low, and that the main goal of this work is to design a wing that would allow an improvement specially at higher speeds. For that order

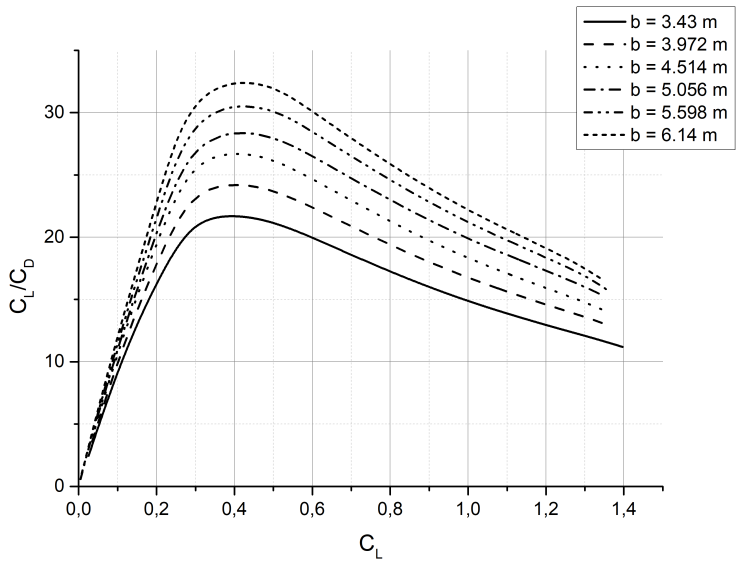

Figure 4.20: C_L/C_D *vs* C_L curves for various span values.

of ideas, it would be more intuitive to chose the smallest span possible. Despite that, it is important to keep a performance at low speeds that does not compromise the safe operation of the UAS30. In addition to that, too low span values also decrease the aerodynamic efficiency of the airplane, parameter that is extremely important regarding range maximization, which is one of the focus of this work. For those reasons, the span of 4.514 m was the one selected because it was considered the best compromise between higher speed performance, lower speed safety and overall aerodynamic efficiency.

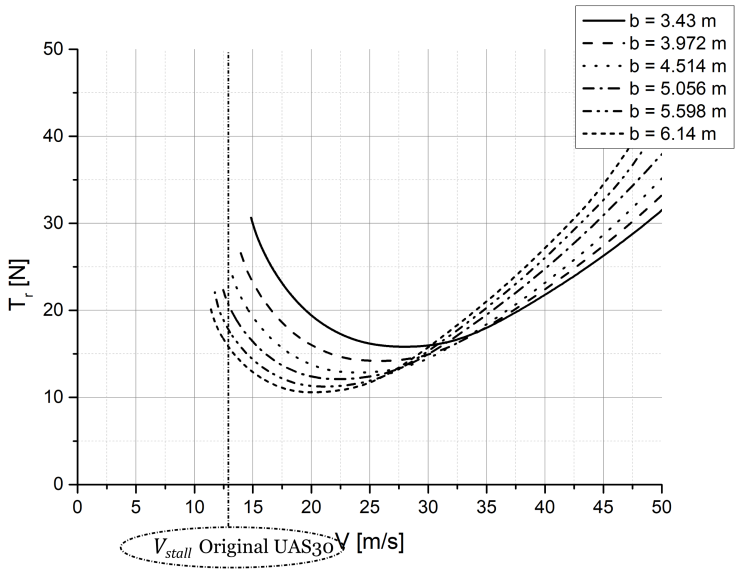

Figure 4.21: T_r *vs* V curves for various span values.

In Figures 4.22 - 4.23 it is possible to compare the graphs of the aerodynamic efficiency in terms of lift coefficient and of the required thrust *vs* speed for the original UAS30 span and the new span of 4.514m. Looking at the graph of Figure 4.22 it is clear that there is an

improvement in aerodynamic efficiency in the whole C_L range, the $(C_L/C_D)_{max}$ value also shows an increase of 2.84%, going from 26 in the original UAS30 to 26.74 using the new span value.

With these results it is possible to claim that the new span performance is more desirable than the one provided by the original span since in addition to providing a better aerodynamic efficiency for the whole range of operations, the new span value also allows a better performance at low speeds without excessively harming the performance at higher speeds.

The graph present in Figure 4.23 does not show such a clear advantage in using the new span. In this case, it is visible that the new span value shows an improvement at lower speeds while the original UAS30 span proves to have an advantageous curve sensibly from a speed of 27 m/s. The stall speed provided by the original span is 13.5 m/s, while the new span allows achieving a V_{stall} of 13.1 m/s. Considering a constant available thrust of 20 N, the airplane with the span of 4.514 m shows a maximum speed of 36.8 m/s, translated in a reduction of 1.79% compared to the 37.47 m/s achieved using the original span. Although, through this graph, this choice seems to be a step backwards with regards to the objectives of the work, it was a choice whose aim was to minimize the low speed performance losses brought by the new airfoil compared to the original and, even so, not to harm excessively the high cruise speed objective.

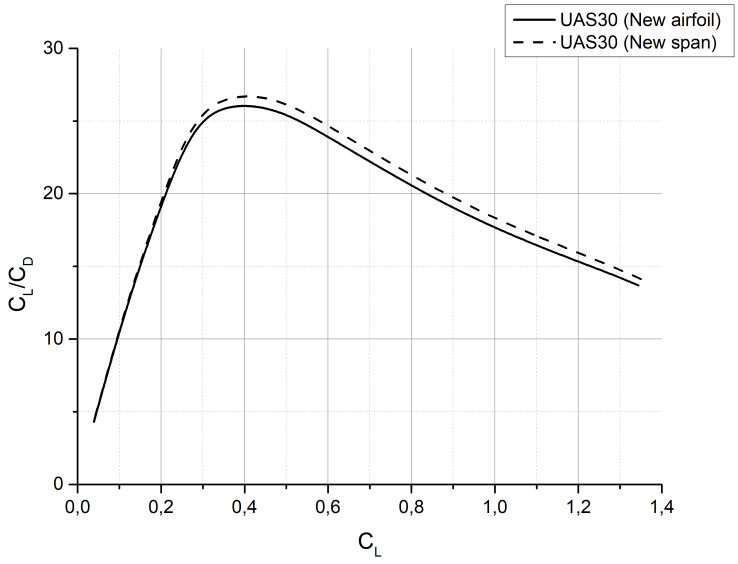

Figure 4.22: C_L/C_D *vs* C_L curves for the original span of the UAS30 (b = 4.29m) and for the span of 4.514m.

With the new span for the UAS30 selected, the study to find out the most advantageous mean aerodynamic chord value could be carried out using the methodology present in Section 3.7. The analysis resulting graphs can be seen in Figures 4.24-4.25.

Looking at Figure 4.24 it is possible to see the C_L/C_D *vs* C_L curves for the different MAC values. Observing these curves it is visible that the aerodynamic efficiency provided by

the different MAC values is basically identical until a C_L of sensibly 0.25 and, from then on, a relation between the aerodynamic efficiency and the MAC value is visible: the higher the mean aerodynamic chord value, the worse the aerodynamic efficiency of the airplane. Regarding this, a MAC of 0.535 m is preferable.

The graph containing the curves of the required thrust *vs* the speed for the airplanes with different MAC values can be consulted in Figure 4.25. Observing this graph, it is also visible that the changes between the curves of the airplanes with different MAC values are not as pronounced as the changes noticed when comparing the airplanes with different span values. In this case, the curves are identical up to about 22 m/s. After that value, the airplanes with smaller MAC prove to be advantageous, presenting lower required thrust for the same speeds. For this reason, the best MAC value to use is 0.535 m. The overall advantage of using smaller mean aerodynamic chord values, in this case, is due to the increase in the wing loading, meaning less wetted area and parasite drag.

With the study for new span and chord values for the UAS30 completed, the new values obtained for these parameters are 4.514 m for the span and 0.535 m for the mean aerodynamic chord. A comparison between the UAS30 with the new airfoil and the UAS30 with the new span and mean aerodynamic chord values in terms of aerodynamic efficiency *vs* lift coefficient and required thrust *vs* speed can be seen in Figures 4.26-4.27.

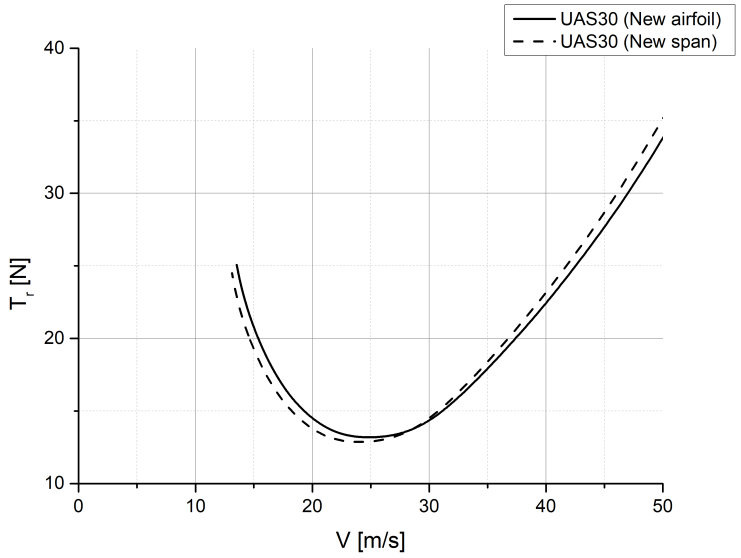

Figure 4.23: T_r *vs* V curves for the original span of the UAS30 (b = 4.29 m) and for the selected new wing span of 4.514 m.

Observing the C_L/C_D *vs* C_L graph (Figure 4.26) it is possible to conclude that the new span and mean aerodynamic chord dimensions, in terms of aerodynamic efficiency qualities, bring only advantages. The curve of the UAS30 with the new span and MAC is identical to the one of the UAS30 only with the new airfoil up to a C_L value of around 0.25 and from that point on, the curve of the UAS30 with the changed span and MAC improves to become practically parallel on top of the curve of the UAS30 with the new airfoil. This means that

an improvement in terms of aerodynamic efficiency for the lift coefficient values from 0.25 on was achieved without harming in any way the C_L values below that. In terms of $(C_L/C_D)_{max}$, the new span and chord values provide an increase of 3.15% in the UAS30 (from 26 to 26.82), without significantly moving the equivalent lift coefficient too far away from the design C_L of 0.33.

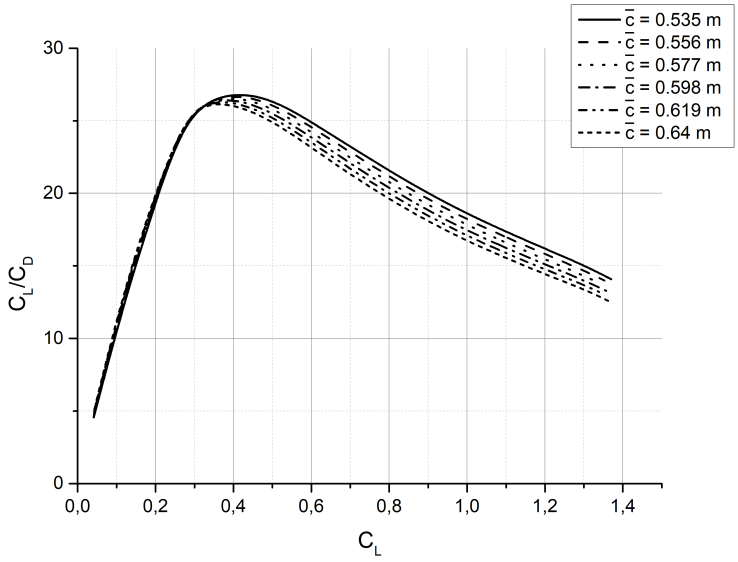

Figure 4.24: C_L/C_D *vs* C_L curves for various mean aerodynamic chord values.

Through the graph present in Figure 4.27 it is also noticeable that the new span and chord values provide enhancements in terms of required thrust *vs* speed. Comparing the two shown curves, it is possible to notice the improvement of the performance up to around 30 m/s. From that speed to approximately 32.6 m/s, the two curves almost coincide and from then on, the curve of the UAS30 with the new airfoil exhibits an almost negligible advantage. Considering an available thrust of 20 N the UAS30 only with the new airfoil presents a maximum speed of 37.47 m/s, while the UAS30 with the new span and chord values shows a maximum speed of 37.4 m/s. In terms of stall speeds, the airplane with only the new airfoil has a value of 13.5 m/s and the airplane with the new span and chord a value of 13.2 m/s. This means an improvement in the minimum speed of 2.2% and a worsen of only 0.18 % in terms of maximum speed, which can be considered as insignificant since the decrease of only 0.07 m/s in the maximum speed parameter has not the same influence in the performance and operation of the UAS30 as the decrease in minimum speed of 0.3 m/s.

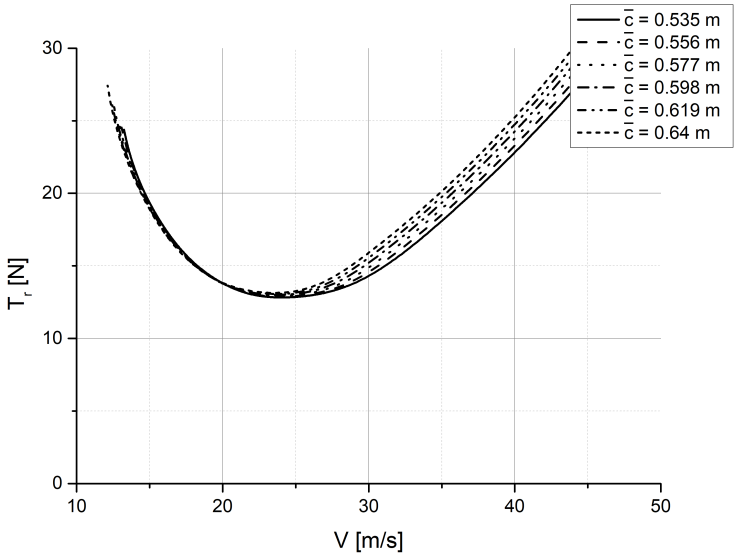

Figure 4.25: T_r *vs* V curves for various mean aerodynamic chord values.

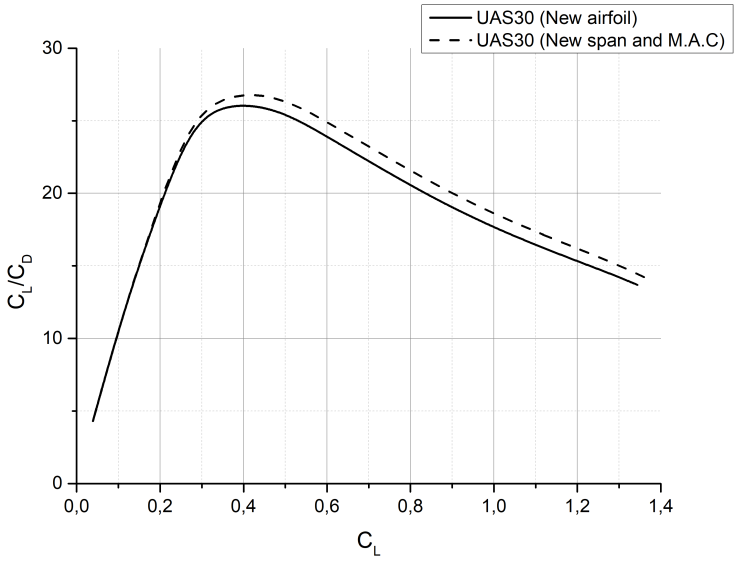

Figure 4.26: $^{C_L}/_{C_D}$ *vs* C_L curves of UAS30 with new airfoil wing together with the new span and MAC change.

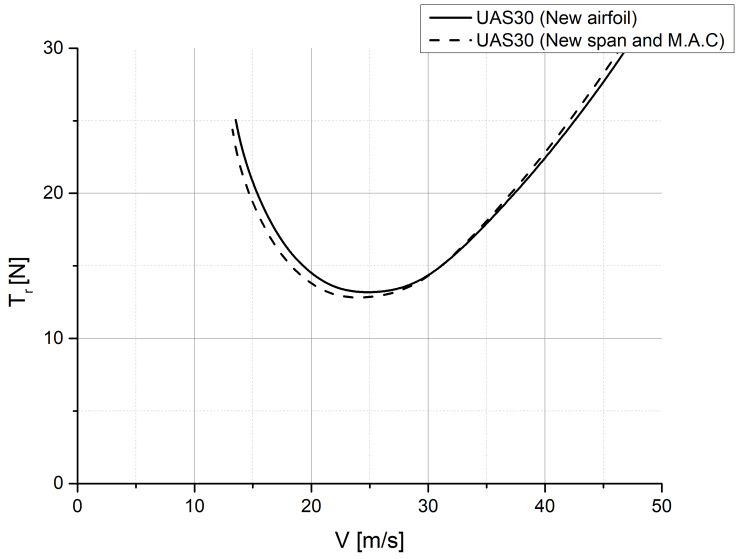

Figure 4.27: T_r *vs* V curves of UAS30 with new airfoil wing together with the new span and MAC change.

4.6 Taper Ratio, Sweep Angle, Dihedral and Incidence of the New Wing

The results of applying the methodology described in Section 3.8 can be consulted in the graphs of Figures 4.28-4.30. Figure 4.28 shows the comparison between the lift coefficient along the span for two taper values and four washout wing designs. As it is possible to observe, the taper of 0.25 provides a distribution with clear excess of lift coefficient near the tip of the wing, which can cause tip stall. The distribution for this taper value is also far from the elliptic. As for the lift coefficient distributions provided by taper ratios of 0.5 with the different washout values, it is visible that the higher values of lift coefficient moved away from the tip, providing a safer operation near stall conditions. It is possible to observe that the higher the absolute value of the washout, the preferable the shape of the lift distribution along the span is regarding tip stall avoiding.

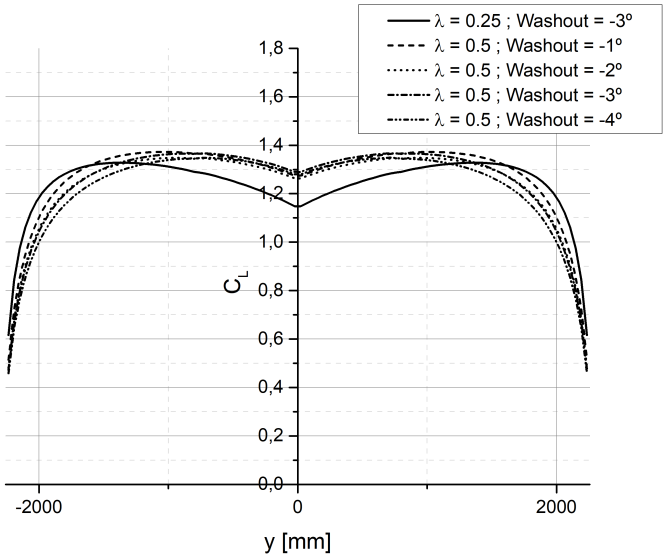

Figure 4.28: Lift coefficient distribution along the span.

In terms of performance, in the graph that contains the curves of aerodynamic efficiency in terms of C_L (Figure 4.29) it is possible to observe that the taper ratio of 0.25 provides better efficiency for C_L values from 0.5 onwards, despite presenting a lower value of maximum aerodynamic efficiency than the taper ratio of 0.5 for any washout value. For a taper ratio of 0.5, it is possible to conclude that the higher the absolute value of the washout, the worse the aerodynamic efficiency curve is. Although this relation is possible to notice, it is also acceptable to claim that for washout values of -1°, -2° and -3° the difference it is not that significant, as for a washout of -4° the difference is already more significant.

The graph containing the required thrust *vs* speed curves of the different taper ratio and washout designs (Figure 4.30) shows that the taper ratio of 0.25 with the washout of -3° provides an advantage regarding speeds from sensibly 27.5 m/s onwards regarding the required thrust. The curves provided by the different washout values for the taper ratio of

0.5 are, once again, pretty similar, being the curves slightly more advantageous the lower the absolute value of the twist. The graphs present in Figures 4.29-4.30 may seem to contradict themselves, since the most advantageous regions regarding the lift coefficients do not directly behave the same way when translated into speeds. This is because keeping the same MAC, which differs in definition with the mean geometrical chord, the wing areas can be different. Thus, the airplane with the taper ratio of 0.25 has the same MAC, but a higher wing loading. Whereby, it exhibits a higher C_L for any speed when compared to the plane with a taper of 0.5. Hence, the C_L/C_D of the airplane with the taper of 0.25 is higher than the airplane with the taper of 0.5 even for low C_L speeds. On the other hand, at low speeds, above the C_L corresponding to the $(C_L/C_D)_{max}$, when the aerodynamic efficiency is dropping with the C_L, the airplane with the taper of 0.5 is able to achieve better C_L/C_D due to having a lower lift coefficient for the same speed.

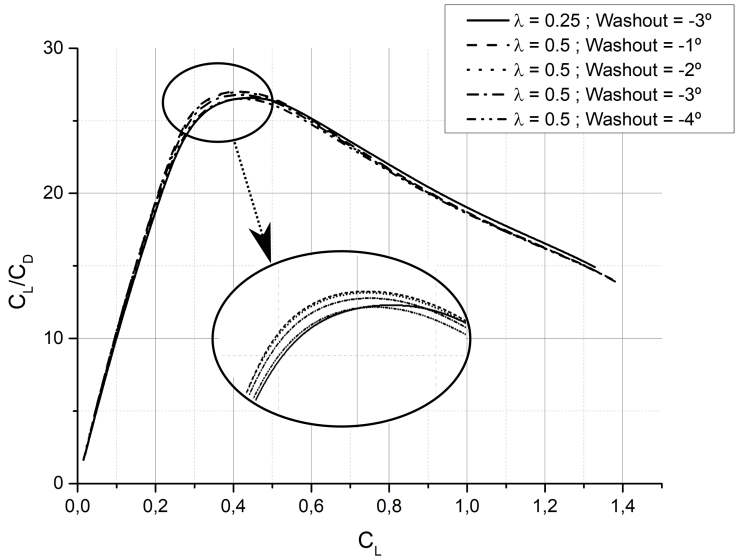

Figure 4.29: C_L/C_D *vs* C_L curves for the different taper ratio and washout values.

Having observed the graphs, it was decided that the taper ratio to keep was 0,5 and the washout -3°. The taper ratio of 0,25, despite being the best option regarding performance, presented a very undesirable lift coefficient distribution along the span, causing this taper value to be excluded. The washout of -3° was selected among the possible options because it was the value that provided the best lift coefficient distribution without harming significantly the aerodynamic performance of the airplane, unlike the -4° that despite providing the best lift coefficient distribution for the selected taper value, most significantly affects the performance of the airplane.

In terms of sweep and dihedral, the considered important outputs of the analysis performed can be seen in Figures 4.31-4.35. Since neither the sweep angle or dihedral seemed to influence significantly the aerodynamic performance, only stability parameters were concerned.

With regards to longitudinal static stability, looking at Figure 4.31, it is possible to observe

that both the sweep angle and the dihedral showed to have direct influence in the shape of the C_m *vs* α curve. Remembering that the wing incidences were adjusted so that each sweep value provided a zero pitching moment coefficient for the $C_{L_{design}}$, the sweep angle of 2.18° provides a more desirable α value (0.9°) for the zero pitching moment coefficient since it's closer to 0°, the fuselage angle that produces less drag. Despite that, the 0° sweep also provides a satisfactory α value for C_m = 0 of 1.4°. The higher sweep also provides a more stable airplane in terms of longitudinal static stability since it exhibits a steeper slope. It is also possible to conclude that the higher the dihedral value, the better behaved the airplane regarding longitudinal static stability.

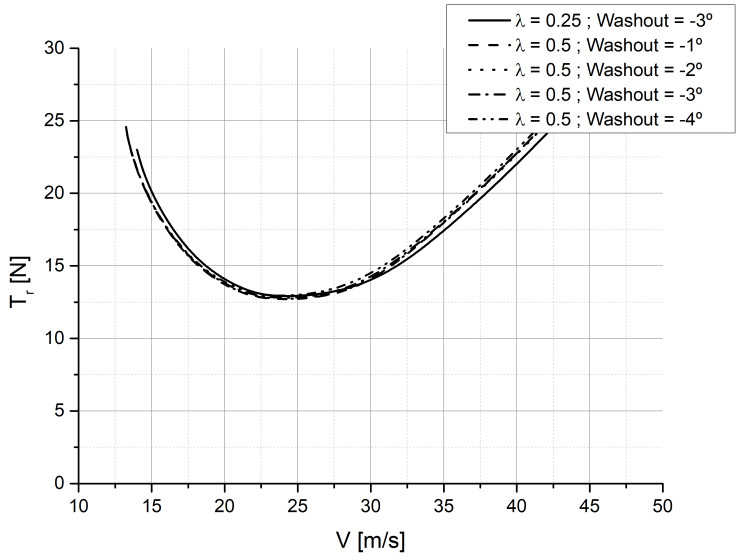

Figure 4.30: T_r *vs* V curves for the different taper ratio and washout values.

Figure 4.32 shows the root locus view for the roll subsidence mode of the airplanes with the different sweep and dihedral values. Observing the graph, it is possible to conclude that the damping of the referred mode is greater the lower the sweep angle, and that for the same sweep value, the damping is greater the higher the dihedral angle value.

Regarding the dutch roll mode, the root locus view can be seen in Figure 4.33. Observing the graph it is possible to conclude that in terms of damping, neither the sweep angle or the dihedral provide much difference regarding this mode. All in all, higher sweep provides lower natural frequency for this mode, and the higher the dihedral angle, the higher the frequency. A better way to understand the influence of the dihedral in the dutch roll is trough Figure 4.34. Observing this graph it is possible to see that the amplitude of the roll rate is higher the lower the considered dihedral angle, which is an undesirable feature since it can induce the mode to become uncontrollable. In this case, it is possible to conclude that for the sweep of 2.18°, increasing the dihedral until a value of 1.5° can be positive since it decreases the amplitude without delaying the convergence. The dihedral of 2° for this sweep value already provides an unwanted delay. For the sweep of 0° this also proves to be true, but with less expression.

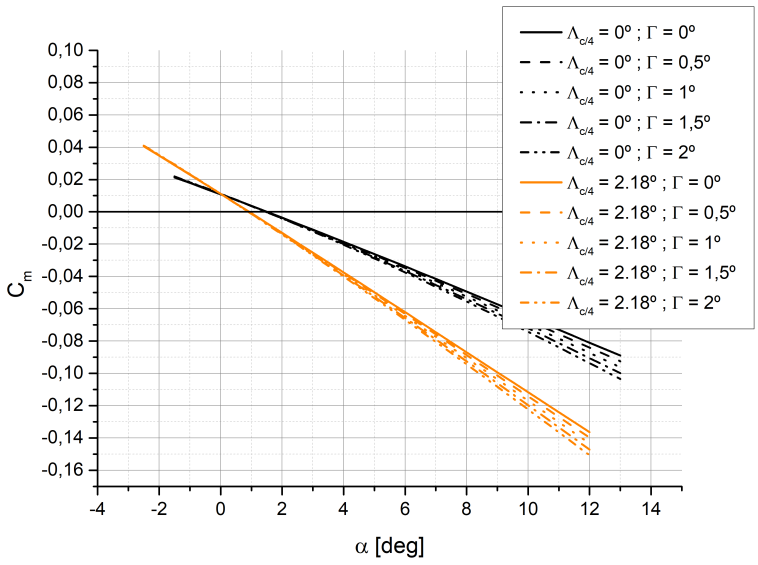

Figure 4.31: C_m *vs* α curves for the different sweep angle values.

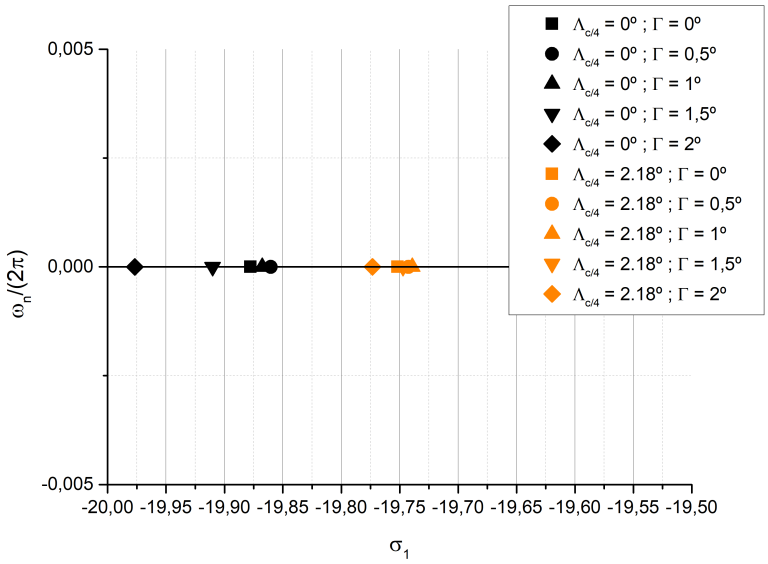

Figure 4.32: Roll subsidence mode roots for various sweep and dihedral values.

In Figure 4.35 it is possible to observe the root locus view concerning the spiral mode roots. Observing the figure it is possible to observe that for each sweep value, the higher the dihedral angle, the closer to 0 is the damping of the mode, which is desirable since less undamped the mode is. Between the two values it is possible to observe that for the same dihedral values, the sweep of 0° provides better results.

With all the results analyzed, it was decided that for the new wings of the UAS30, the most advantageous combination of sweep and dihedral angles, among the analyzed ones, were a sweep of 2.18° and a dihedral of 1.5°. These values were the ones considered to provide the best compromise between the different stability modes. The sweep of 2.18° provided the most desirable C_m *vs* α curve since it provides the AoA for C_m = 0 closer to 0 and a

greater static stability. In the roll subsidence, the selected sweep value also provided the highest damping ratios. As for the dutch roll, a dihedral of 1.5° also proved to provide the most desirable behavior. The spiral mode could benefit from both the sweep of 0° and dihedral of 2°, but since these values would harm the other features, and considering that the spiral mode would continue unstable, as it happens with many conventional airplanes, these were not considered. A summary of all the parameters selected in this Section can be seen in Table 4.6.

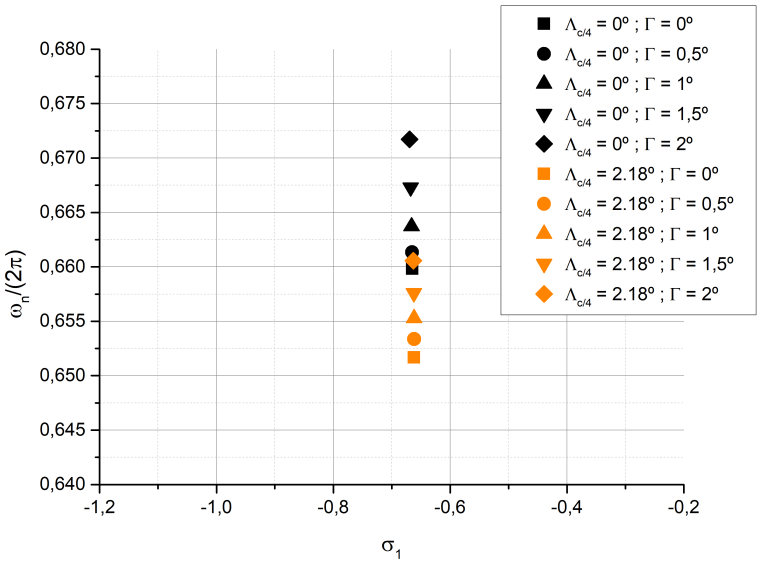

Figure 4.33: Dutch roll mode roots for various sweep and dihedral values.

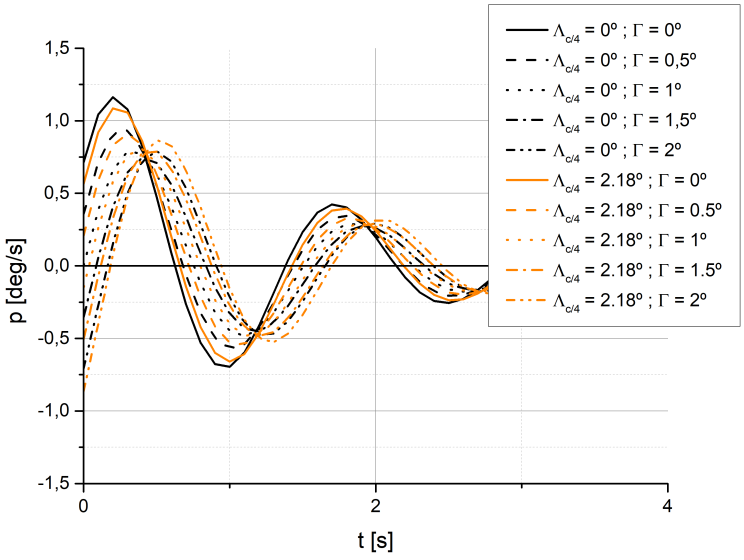

Figure 4.34: Time response of pitch roll rate for various sweep and dihedral values.

Table 4.6: New wing for the UAS30 design parameters.

Parameter	Value
Taper ratio (λ)	0.5
Wing twist [deg]	-3
Sweep angle based on the quarter chord ($\Lambda_{c/4}$) [deg]	2.18
Dihedral angle (Γ) [deg]	1.5
Incidence [deg]	2.08

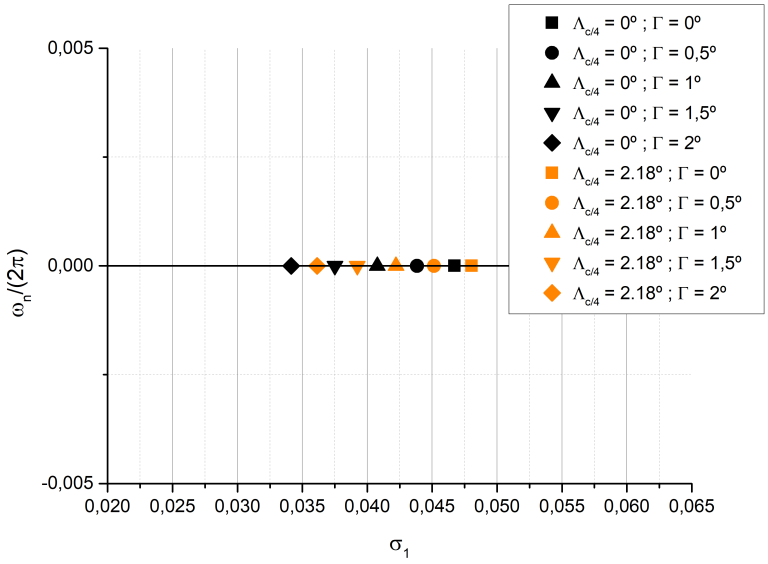

Figure 4.35: Spiral mode roots for various sweep and dihedral values.

4.7 Stability Analysis

In Figure 4.36 it is possible to observe the graph containing the curves of pitching moment coefficient *vs* lift coefficient for both airplanes. As stated previously, the most important two aspects to ensure in this graph are that the point at which C_L equals 0, the pitching moment coefficient is positive and that the slope of the curve is negative. Checking both curves, it is visible that the two airplanes own these features. Also, as it is also possible to visualize, both the airplanes without the fuel load present similar curves to the ones with full load, which means that in terms of longitudinal static stability, the fuel decrease during operation will not have a negative impact.

The neutral point of the original UAS30 is located at x = 0.278 m for both the full loaded and the fuel emptied airplanes, while the neutral point of the UAS30 with the new wing is located at x = 0.310 m also for both load conditions. These neutral points translate into static margins of respectively 9.3% and 9.66% for the original UAS30 and 14.6% and 14.8% for the UAS30 with the new wing, values which are within the typical ones.

In terms of the dynamic stability analysis performed with XFLR5, the output of the root locus view for both airplanes can be seen in Figure 4.37. Observing the left figure concerning the longitudinal modes, it is possible to see the two symmetrical short period modes

and the two symmetrical phugoid modes. The short period modes for the original UAS30 show a slightly higher damping than for the UAS30 with the new wing, the phugoid modes show close behaviors concerning both the natural frequency and the damping ratio. All the longitudinal roots have negative values of damping rations, which means that for the two airplanes, all the four longitudinal modes are dynamically stable. Observing the figure on the right for the root locus of the lateral modes, it is visible that the two airplanes have similar roots, being that the airplane with the new wing has a slightly higher damping regarding the roll subsidence mode, while the original UAS30 shows also a slightly higher damping with regard to the dutch roll modes. The spiral mode has a positive damping ratio for both the airplanes, meaning that the mode is unstable. This is typical from this mode (as seen in Section 2.1) and does not represent a problem, since because of the low magnitude of the mode, the pilot can easily correct its instability.

In terms of the time response view, it is possible to see the results of both longitudinal and lateral stability modes for both versions of the UAS30 in Figures 4.38-4.42. Observing all the represented graphs it is possible to state that, for both the airplanes, the stability of all modes, except for the spiral divergent, are confirmed. Note that the phugoid mode is much better damped in the original UAS30 than in the UAS30 with the new wing, despite the mode being stable for both the airplanes. Regarding the spiral divergent mode, it is also noticeable the lower magnitude of the divergence of the mode for the UAS30 with the new wing, which is positive since less corrections the pilot must do in order to keep a straight trajectory.

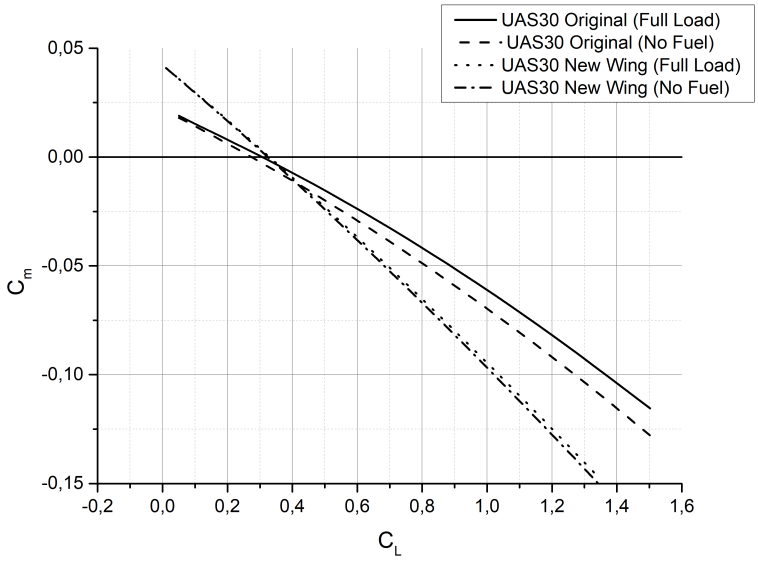

Figure 4.36: C_m *vs* C_L curves of the original UAS30 and the UAS30 with the new airfoil.

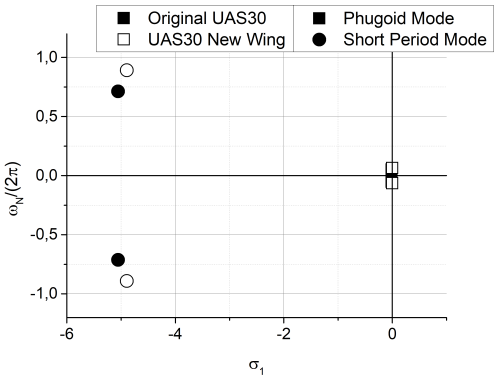

(a) Longitudinal modes.

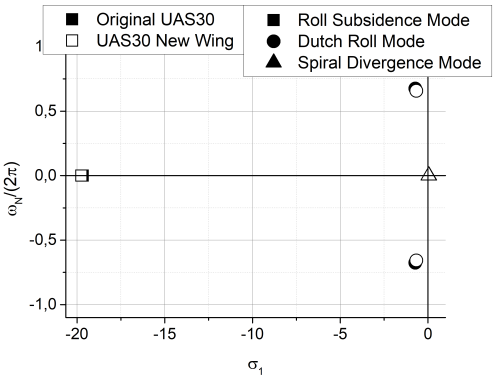

(b) Lateral modes.

Figure 4.37: Root locus views for longitudinal and lateral stability of the original UAS30 and the UAS30 with the new airfoil.

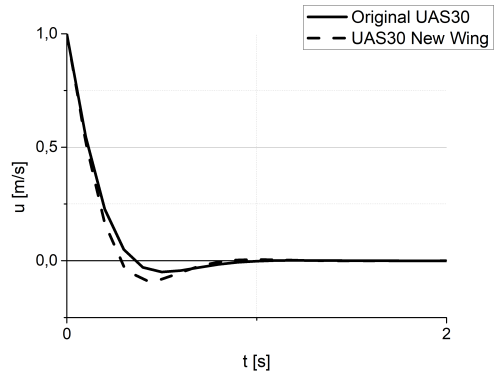

(a) Fluctuation in horizontal speed *vs* time.

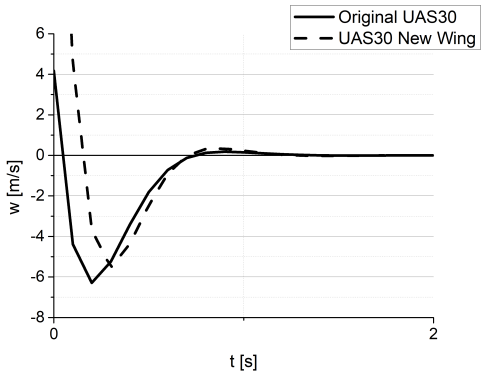

(b) Fluctuation in vertical speed *vs* time.

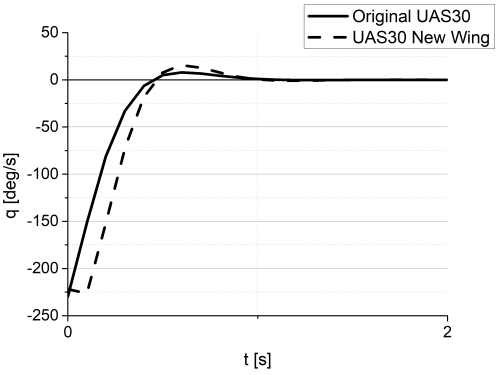

(c) Pitch rate *vs* time.

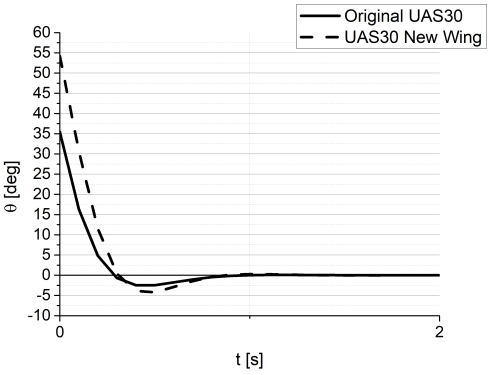

(d) Pitch angle *vs* time.

Figure 4.38: Time response views of the short period modes of the original UAS30 and the UAS30 with the new airfoil.

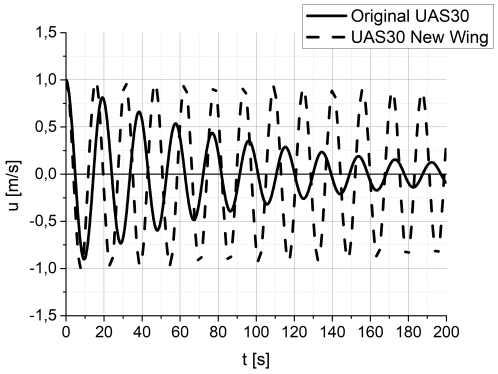

(a) Fluctuation in horizontal speed *vs* time.

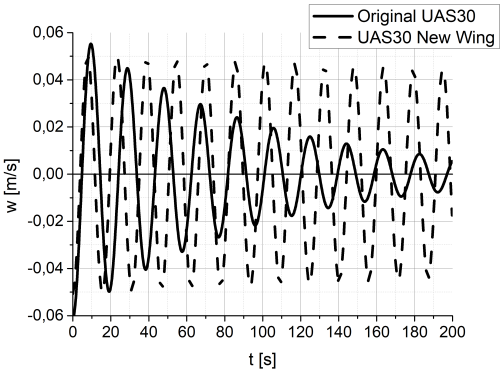

(b) Fluctuation in vertical speed *vs* time.

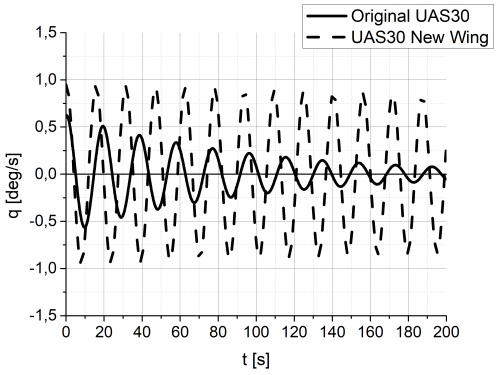

(c) Pitch rate *vs* time.

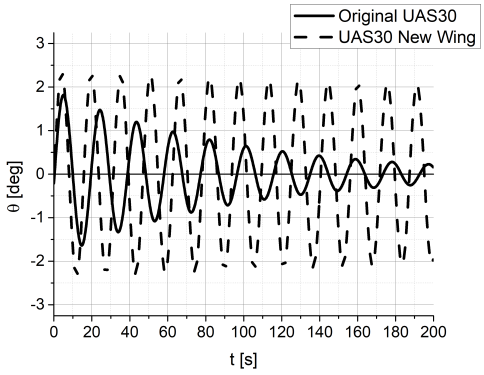

(d) Pitch angle *vs* time.

Figure 4.39: Time response views of the phugoid modes of the original UAS30 and the UAS30 with the new airfoil.

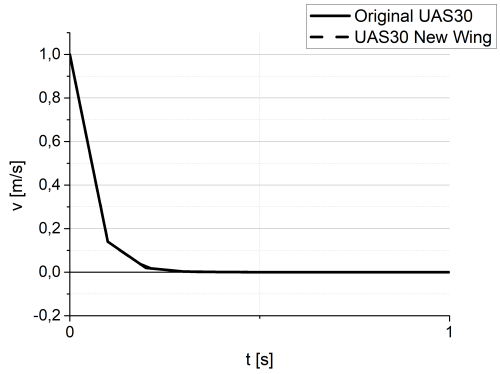

(a) Fluctuation in lateral speed *vs* time.

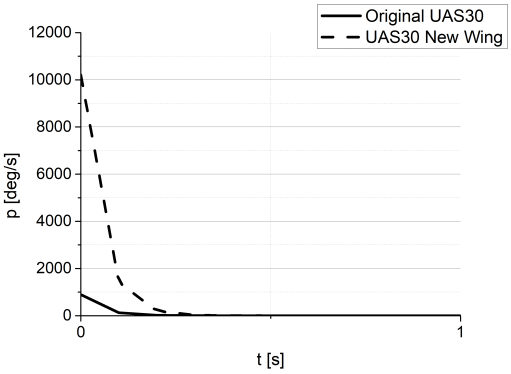

(b) Roll rate *vs* time.

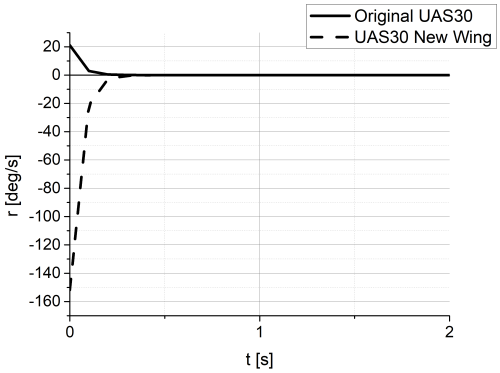

(c) Yaw rate *vs* time.

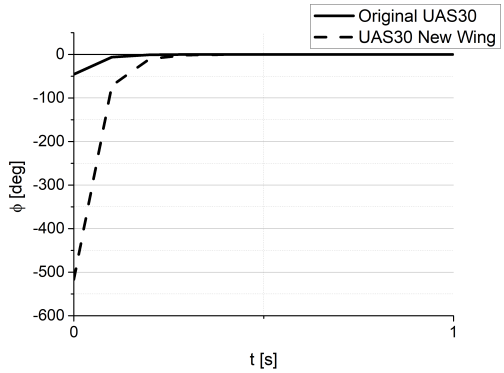

(d) Roll angle *vs* time.

Figure 4.40: Time response views of the roll subsidence modes of the original UAS30 and the UAS30 with the new airfoil.

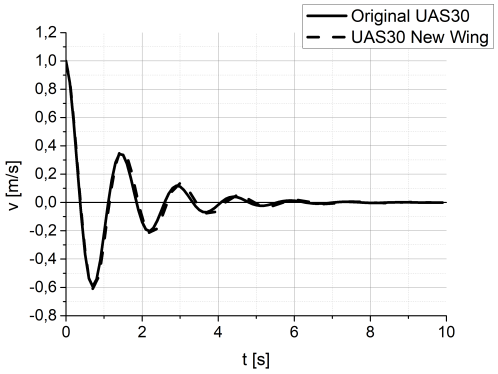

(a) Fluctuation in lateral speed *vs* time.

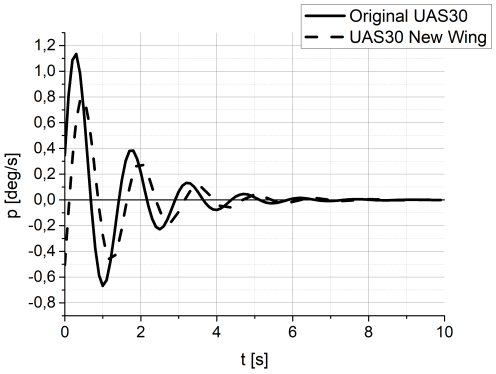

(b) Roll rate *vs* time.

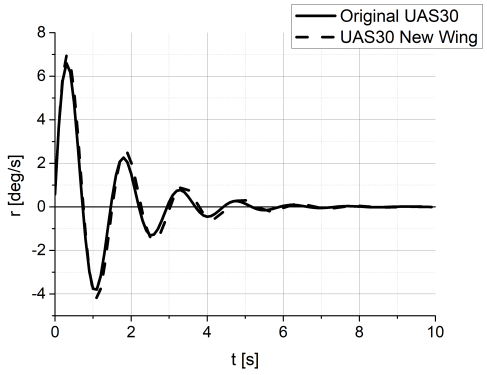

(c) Yaw rate *vs* time.

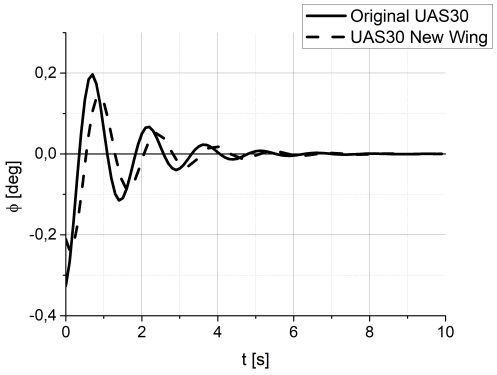

(d) Roll angle *vs* time.

Figure 4.41: Time response views of the dutch roll modes of the original UAS30 and the UAS30 with the new airfoil.

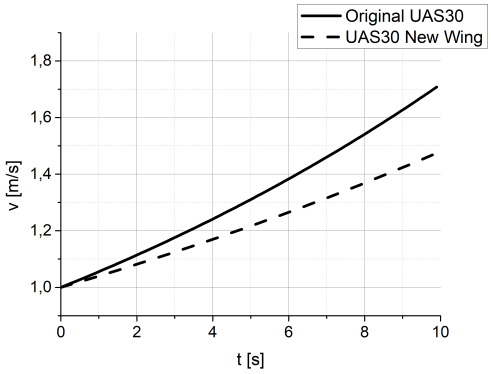

(a) Fluctuation in lateral speed *vs* time.

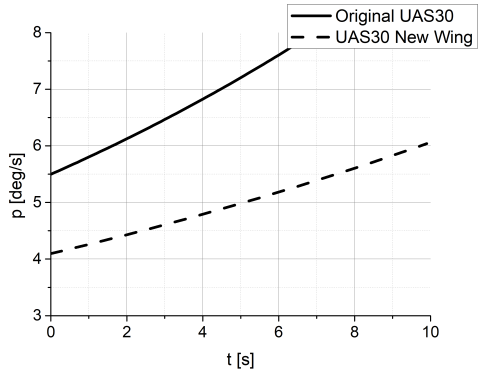

(b) Roll rate *vs* time.

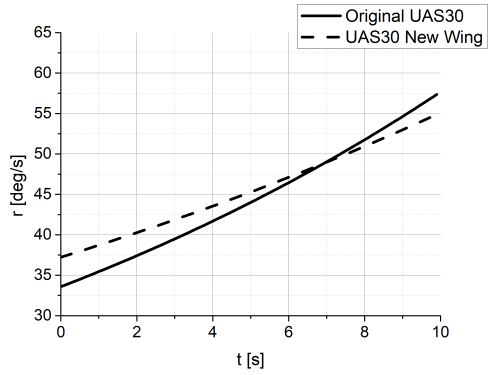

(c) Yaw rate *vs* time.

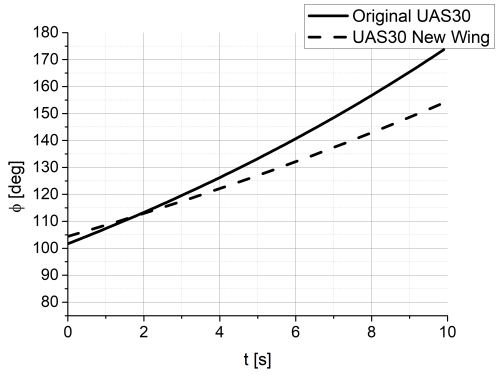

(d) Roll angle *vs* time.

Figure 4.42: Time response views of the spiral divergent modes of the original UAS30 and the UAS30 with the new airfoil.

4.8 Final Performance Estimation

4.8.1 Aerodynamic Performance

The C_L/C_D *vs* V curves output from the different airplane analyses can be seen in Figure 4.43. Observing first the curves corresponding to the UAS30 with the original wing against the UAS30 with the new wing without flaps, it is possible to see that the improvements provided by the new wing regarding aerodynamic efficiency are clear for almost the whole range of speeds, exhibiting only a slight worsening between the speeds of about 13.5 m/s and 16.25 m/s. The $(C_L/C_D)_{max}$ parameter shows an expressive increase of 26.19 %, going from 21.27 to 26.84. Regarding the C_L/C_D value for the speed corresponding to the design lift coefficient, 27 m/s, the improvement is even more pronounced, going from 16.87 to 26.2, meaning an increase of 55.3 %.

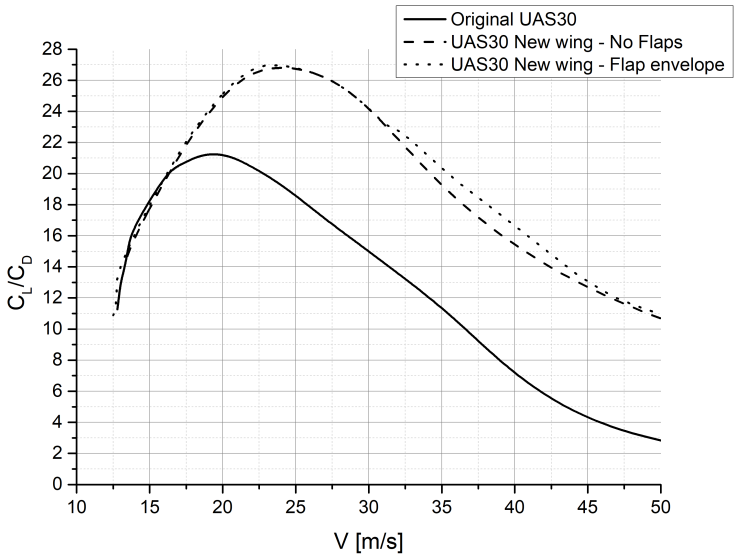

Figure 4.43: C_L/C_D *vs* V curves for the UAS30 equipped with the original wing and the new wing, with and without flaps.

Observing the curve related to the new wing with flaps, it is possible to see that it can also bring improvements to the new wing of the UAS30. Firstly, in terms of $(C_L/C_D)_{max}$, it exhibits a value of 26.94, that, despite being slight, it is still an increase. The C_L/C_D for the design conditions does not undergo any type of change. Where flaps prove to be most beneficial is for speeds above 32.5 m/s. The flaps also allow to achieve lower speeds.

In Figure 4.44 it is possible to observe the graph containing the curves of required thrust *vs* speed for the three different airplanes. Through the graph, it is visible that the new wings, once again, provide an overpowering improvement regarding required thrust for practically the whole range of speeds, except regarding the stall speed. When it comes to this parameter, the UAS30 original presents a value of 12.8 m/s, while the version with the new wing design presents a value of 13.4 m/s, translating into a worsening of 4.7%.

Considering a fixed thrust of 20 N, the UAS30 with the original wing would achieve a maximum speed of 26.89 m/s while the new wing without flaps would achieve a maximum speed of 37.15 m/s (an improvement of 38.16 %). Regarding the speed corresponding to the $C_{L_{design}}$ (27 m/s) the original wing requires a thrust of 17.19 N, while the new wing requires 13.1 N of thrust. This means a decrease of 23.79 %.

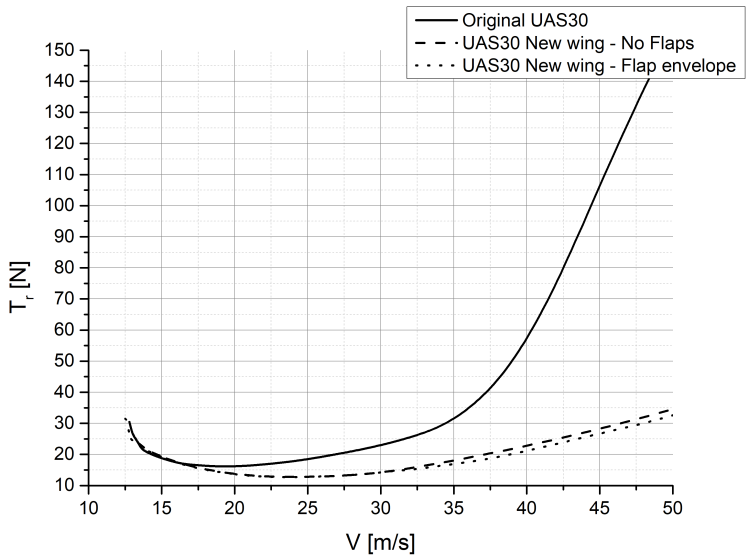

Figure 4.44: T_r *vs* V curves for the UAS30 equipped with the original wing and the new wing, with and without flaps.

Regarding the new wing with flaps, there are also improvements. The stall speed becomes 12.5 m/s (even better than the original UAS30). In terms of the maximum speed for a thrust of 20 N, the flaps allow the airplane to achieve a maximum speed of 39.07 m/s. These are improvements for both parameters. In terms of the required thrust for the speed of 27 m/s there are also no changes compared to the airplane using the new wing without flaps.

Although the main focus in terms of aerodynamics throughout the work has never been the $C_L^{\frac{3}{2}}/C_D$ parameter, it is still interesting to observe the differences in this parameter for the various airplanes. In Figure 4.45 it is possible to see the curves of this parameter *vs* speed for the three UAS30 with the distinct wings. As it is possible to observe, the new wing also shows to be more advantageous regarding this parameter for almost the whole range of speeds. This just does not happen for speeds between 13.5 m/s and 16.25 m/s, similar to what happens with the C_L/C_D parameter. The $\left(C_L^{\frac{3}{2}}/C_D\right)_{max}$ goes from 19.27 in the airplane using the original wing to 19.48 in the airplane with the new wing without flaps, meaning an increase of 1.1%, which is not very expressive. In the region of the design coefficient speed, the differences are more evident, with the airplane with the new wing exhibiting a value of 15.08 against the 9.95 provided by the original wing, meaning a clear improvement of 51.56 %.

The new wing with flaps also shows to provide advantages in the same regions as the other

discussed parameters. The $\left(C_L^{\frac{3}{2}}/C_D\right)_{max}$ has a value of 19.62, while the $C_L^{\frac{3}{2}}/C_D$ for 27 m/s exhibits a value of 15.08, the same as the airplane not using flaps. Between the speeds of approximately 31 m/s and 45 m/s is where the flaps show to be more advantageous regarding this parameter.

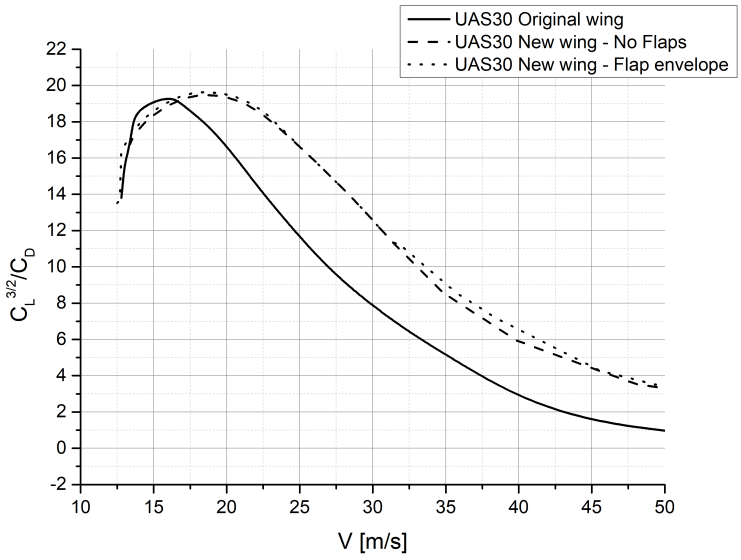

Figure 4.45: $C_L^{\frac{3}{2}}/C_D$ *vs* V curves for the UAS30 equipped with the original wing and the new wing, with and without flaps.

The corresponding deflection angles for the considered flap envelopes can be consulted in Appendix B.

4.8.2 Selected Propeller

After applying the methodology referred in Section 3.10, the graph containing the T_a *vs* V curves for the different recommended propellers, along with the T_r *vs* V curves of the different airplanes, can be seen in Figure 4.46. Observing the graph, it is possible to conclude that none of the considered propellers is able to provide the most advantageous thrust conditions for the three airplanes simultaneously. Regarding the UAS30 with the original wing, both the 23x12" and the 21x12" propellers allow it to achieve the higher maximum speeds, being the 21x12" propeller the one which provides the most advantageous thrust conditions for the whole range of speeds. For that reason, the latter was the selected for the UAS30 with the original wing.

For both versions of the UAS30 with the new wing (with and without flaps), the propeller which provides the most advantageous thrust conditions is the 22x15". This propeller was the selected because, in addition to being one of the two only propellers (along the 22x16") capable to provide thrust at higher range of speeds, allowing to utilize the potential of the UAS30 with the new wing to operate at higher speeds, it is also the one between the two

propellers which provides more thrust for the whole range of speeds. With that said, the 22x15" propeller was the one selected for the two versions of the UAS30 with the new wing.

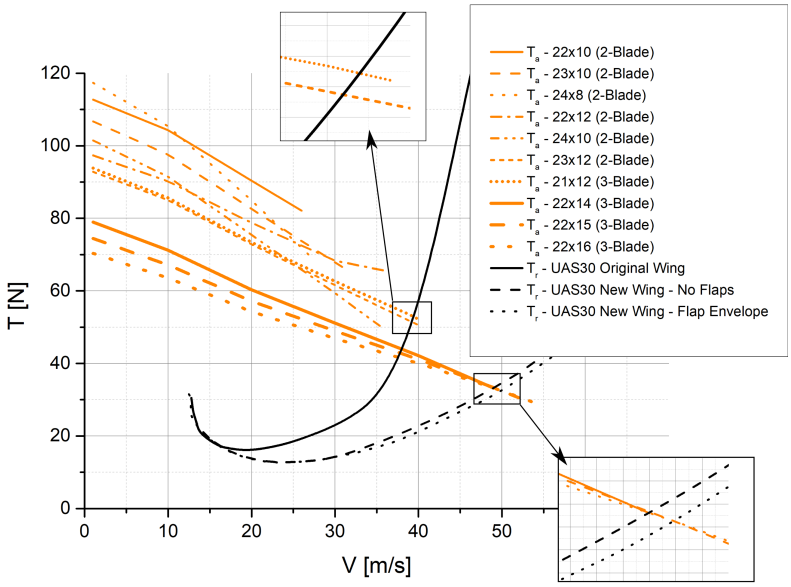

Figure 4.46: T_a *vs* V curves for the different tested propellers along the T_r *vs* V curves of the different airplanes.

4.8.3 Performance Comparison

In Figure 4.47 the graph containing the T_r *vs* V curves for the three versions of the UAS30, as well as the T_a *vs* V curves of the propulsive system, can be seen. Observing the graph it is possible to identify V_{max}, V_{stall} and $V_{\gamma_{max}}$ for the different airplanes.

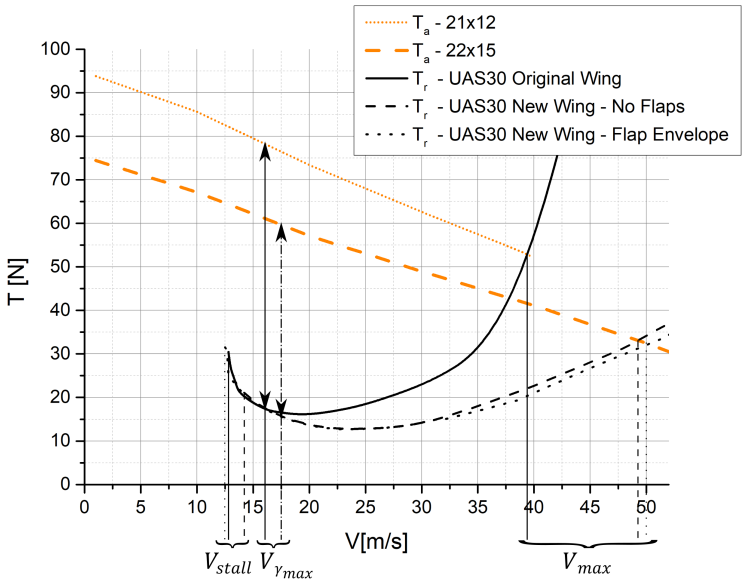

Figure 4.47: T_r *vs* V curves for the different airplanes along T_a curve *vs* V of the propulsive system.

With regards to V_{stall}, it is possible to see that the UAS30 with the new wing using flaps is the airplane that is able to achieve the lower value, with 12.5 m/s. The UAS30 with the original wing achieves a minimum speed of 12.8 m/s, while the UAS30 with the new wing without flaps achieves a value of 13.4 m/s, which means that although the new wings slightly harm the stall speed of the UAS30, this problem can be solved with the usage of flaps, allowing it to achieve a speed even lower than the one shown by the UAS30 with the original wing. The rate of climb corresponding to the stall speed of different planes are: 1.94 m/s with a climb angle of 8.7 ° for the UAS30 with the original wing; 1.55 m/s with a climb angle of 6.7 ° for the airplane with the new wing without flaps; 1.2 m/s with a climb angle of 5.5 ° for the UAS30 with a new wing and using flaps.

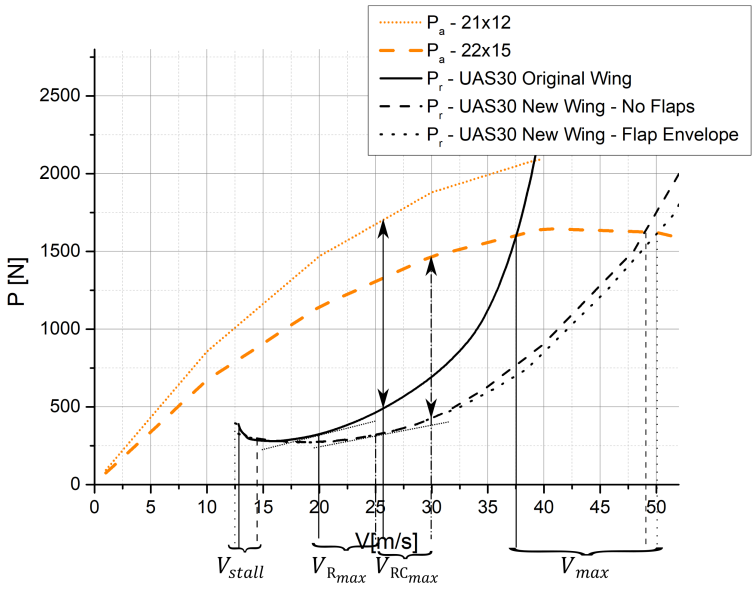

Figure 4.48: P_r *vs* V curves for the different airplanes along P_a curve *vs* V of the propulsive system.

Regarding V_{max}, the UAS30 with the original wing exhibits a value of 39.7 m/s, while the UAS30 with the new wing with and without flaps have values of 49.1 and 50 m/s respectively. This means that the new wings allow the UAS30 to fly 23.7% faster without flaps and 26% with flaps.

The $\gamma_{\max}$ of the UAS30 with the original wing, occurs at a speed of 16 m/s, having a value of 10.2 ° and corresponding to a rate of climb of 2.83 m/s. For the UAS30 with the new wing without flaps, this parameter occurs at 17.5 m/s and presents a value of 7.3 °. Its corresponding rate of climb presents a value of 2.3 m/s. With flaps, the $\gamma_{\max}$ occurs at the same speed, but increases up to a value of 7.4 ° with a rate of climb of 2.25 m/s.

Figure 4.48 contains the P_r *vs* V curves for the different airplanes along the P_a *vs* V curve of the propulsive system. Through this graph, in addition to the parameters already identified in Figure 4.47, it is possible to identify two new speeds for each plane: the $V_{R_{max}}$, corresponding to the speed of maximum range and the $V_{RC_{max}}$, the speed for the maximum rate of climb.

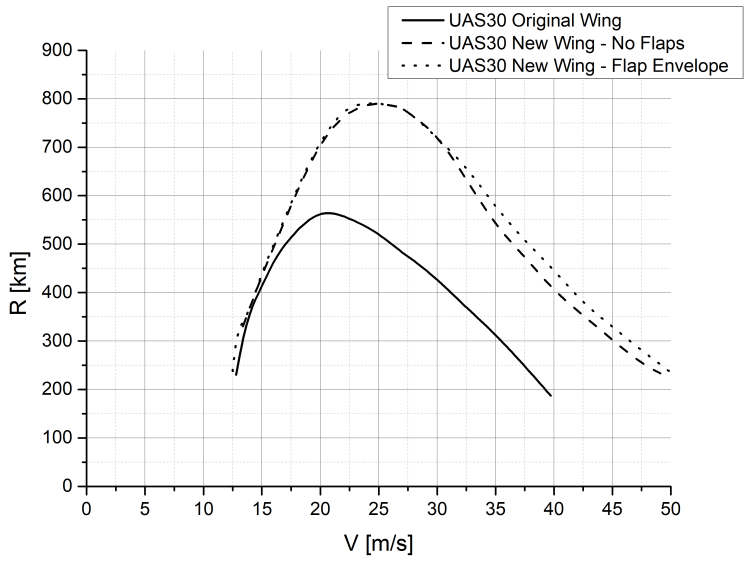

Figure 4.49: Range *vs* V curves for the different airplanes.

The $V_{R_{max}}$ is 20 m/s for the UAS30 with the original wing and 25 m/s for the airplane with the new wing with and without flaps. This means that the range of the UAS30 is maximized for higher speeds with the new wing than it is with the original wing, confirming the adequacy of the new wings for higher speeds.

Regarding the $V_{RC_{max}}$, it is located at 26 m/s for the UAS30 with the original wing with a value of 3.6 m/s, corresponding to a climb angle of 7.98°. For the airplane with the new wing, this parameter occurs at a speed of 30 m/s with and without flaps presenting a value of 3.03 m/s with a climb angle of 5.8°. Overall, the new wing provides lower values of rate of climb and climb angles than the original wing. This can be solved using a variable pitch propeller, which would provide higher thrust values for the whole range of speeds, meaning higher excessive thrust and thus higher rate of climb and climb angle values.

In Figure 4.49 the curves of the estimated range *vs* speed for the different airplanes are represented. Observing the graph it is possible to conclude that the newer versions of the UAS30 allow achieving substantially higher range values for the whole range of speeds. The usage of flaps also shows to improve the range, especially for the lower and higher values of speed, not altering this parameter near the design speed condition. In terms of this condition, *i.e*, at 27 m/s, while the original wing allows achieving 483.2 km, while the new wing, both with and without flaps, allows achieving 779.6 km, which means an expressive increase of 61.3 %. As maximum range values, the UAS30 with the original wing achieves a range of 561.7 km for a speed of 20 m/s, the new version achieves a range of 789.9 km at 25 m/s with and without flaps.

The endurance *vs* speed curves for the different airplanes can be seen in Figure 4.50. Observing the graph, it is also possible to see that the new wings provide an absolute improvement regarding endurance for the whole range of speeds, being more expressive at higher

speeds. At the speed of 27 m/s the original wing allows achieving 5.2 h of endurance, while the new wing allows achieving 8.2 h with and without flaps, meaning an increase of 73 %. The maximum endurance occurs for the airplane equipped with the original wing at 17.5 m/s and has a value of 8.5 h. For the UAS30 with the new wing without flaps, this condition occurs at 20 m/s with a value of 10 h. The airplane with flaps achieves 10.1 h of endurance for a speed of 20 m/s.

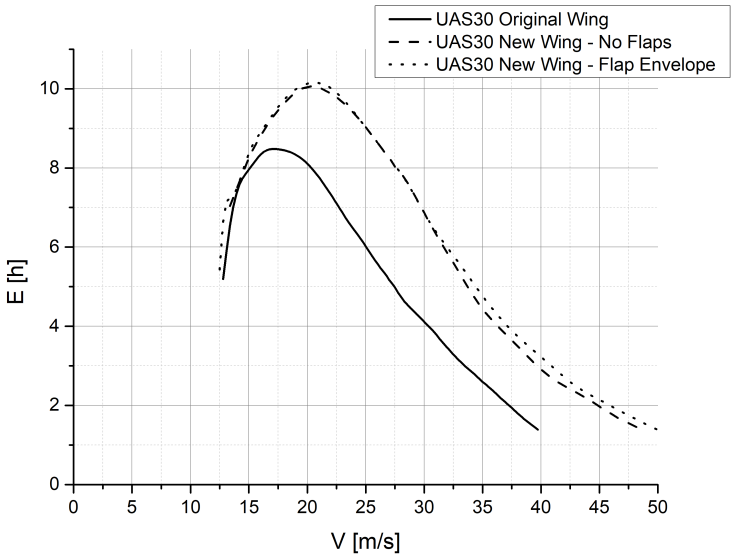

Figure 4.50: Endurance *vs* V curves for the different airplanes.

The η_p *vs* V curve for the propeller efficiency values for the determination of both range and endurance for the considered range of speeds can be consulted in Appendix A.3.

The characteristics of the UAS30 using the new wing design with and without flaps can be seen in Table 4.7. Also, a comparison between the original and the new wing design geometries, as well as a comparison of the two wing designs included in the UAS30 fuselage can be found in Appendix C.

Table 4.7: Characteristics of the UAS30 with the three different wing solutions.

Parameter	UAS30 Original Wing	UAS30 New Wing - No Flaps	UAS30 New Wing - Flaps
Wing			
Span [m]	4.29	4.514	4.514
Area [m^2]	2.28	2.33	2.33
Aspect Ratio	8.07	8.749	8.749
Taper Ratio	0.51	0.5	0.5
Incidence [deg]	1.893	2.08	2.08
Sweep Angle [deg]	-0.005	2.18	2.18
Root Airfoil	AH79-100C	FEMS1017	FEMS1017
Tip Airfoil	AH79-100C	FEMS1017	FEMS1017
Twist [deg]	-3	-3	-3
Propulsion			
Propeller [in x in]	21x12	22x15 (3 Blades)	22x15 (3 Blades)
Aerodynamics			
$C_{L_{max}}$	1.51	1.344	1.542
$^{L}/_{D_{max}}$	21.27	26.84	27
Performance			
Stall Speed [m/s]	12.8	13.4	12.5
Maximum Speed [m/s]	39.7	49.1	50
Maximum Rate of Climb [m/s]	3.6	3.03	3.03
Maximum Range [km]	561.7	789.9	789.9
Maximum Endurance [h]	8.5	10	10.1

Chapter 5

Conclusions and Future Work

5.1 Overview

This work had as primary goal the design of a wing that would allow the UAS30 platform to operate efficiently at higher cruise speeds than it already operated when using the original wing. For that, the fundamentals regarding wings design as well as overall aircraft design considerations had to be understood and applied to the specific objectives of the work. In order to achieve the proposed objective, the original UAS30 features were considered and the wing design parameters were changed aiming at the new requirements.

The first parameter to be changed was the airfoil. This parameter proved to be the most important factor in terms of the aerodynamic performance of the airplane. Changing only the airfoil to one that was more suitable for the design lift coefficient provided an increase of 22.3% in the maximum aerodynamic efficiency of the UAS30, as well as an increase of 39.4% in the maximum speed for an arbitrary available thrust of 20 N. These performance improvements alone would, by themselves, probably be enough to achieve the main objective of designing a wing that could provide higher performances and higher operational speeds to the UAS30.

In order to improve even further the performance of the airplane, other geometrical parameters of the wing were changed. The span, after the airfoil, was the parameter that proved to be more influential regarding the performance of the UAS30. Despite slightly sacrificing the high speed region performance, increasing the span allowed an improvement in the $(C_L/C_D)_{max}$ of the UAS30 by 2.84%, as well as a decrease in stall speed of 2.9%. Therefore, as a performance compromise between lower and higher speeds, the span of 4.514 m was the final choice. The MAC was more like a "fine tuning" of the wing performance, its influence in the performance of the airplane although effectively exists, did not prove to be as expressive as the airfoil or even the span. A value of 0.535 m was chosen for representing the best compromise between keeping a low stall speed and a high cruise speed.

In addition to performance, the stability and flight safety of the UAS30 were also concerned in this study. In order to account for these features, parameters like taper ratio, sweep angle, dihedral and twist were studied. The taper ratio and the washout proved to be the most important design parameters regarding the stall quality of the airplane. All in all, the higher the taper ratio and the more negative the washout the better stall qualities but also more pronounced the performance harming. Because of that, the val-

ues were chosen taking into account a compromise between safety and performance. The taper value was also limited by wing thickness requirements, not allowing the selection of a taper ratio below 0.5. The remaining parameters were chosen so that the stability of the UAS30 was also the best possible without harming its performance. The dihedral and sweep were the parameters that showed to influence more evidently the lateral stability. The sweep also showed to be important regarding longitudinal static stability.

The final performance estimation allowed to compare the new wing design solution with the original wing of the UAS30 regarding the wanted operation requirements. The new wing solution, without flaps, allows the UAS30 to achieve a maximum speed of 49.1 m/s. This speed, when compared with the 39.7 m/s obtained with the original wing, means an increase of 39.7% in possible cruise speeds. The new wing design also allowed to increase the maximum range from 561,7 km to 789.9 km (40.6% of improvement), as well as to increase the range for the whole range of speeds. These two parameters can confirm that the main objectives of this work, *i.e*, increasing the range and cruise speed of the UAS30 with the design of a new wing solution, were clearly achieved. In addition to that, it was also concluded that using flaps in the new wing design also allows the UAS30 to achieve lower stall speeds than the original wing (12.5 m/s against 12.8 m/s), as well as to achieve even higher speeds than the new wing design without flaps (50 m/s against 49.1 m/s). In addition to a clear improvement in the maximum speed and range, the endurance was also considerably improved, going from a maximum value of 8.5 h for the UAS30 with the original wing, to 10 h for the UAS30 with the new wing design, being that with flaps this parameter can go up to 10.1h. In terms of climb qualities, *i.e*, climb angles and rates of climb, the new wing design together with the selected propeller (22x15 - 3 Blades) present some disadvantages when compared with the original wing and the corresponding selected propeller (21x12). The RC_{max} drops from 3.6 m/s in the UAS30 with the original wing to 3.03 m/s in the UAS30 with the new wing design and the γ_{max} from 10.18° to 7.33°. This can be improved by using a variable pitch propeller in order to have greater power and excess thrust for the whole range of speeds.

5.2 Open Points and Future Work

The work carried throughout this dissertation, despite having been carried out such that the results could be as accurate as possible, has some limitations. The software used for the aerodynamic analysis of the airfoils, wings and airplanes and consequent parameter selection based on the results of those analysis, XFLR5, despite having already proven itself as a competent two dimensional flow predictor, regarding three dimensional wings has some inaccuracy in the wings wake prediction that do not allow to provide the most accurate results. Because of that, the results of the aerodynamic and stability analysis, despite having the necessary accuracy to be possible to state that the objectives of the work were achieved, must be considered with some margin of error. Because of that, in order to obtain more accurate estimates of the aerodynamic qualities of the airplane, more

accurate CFD methods or even experimental studies should be performed.

Although the compatibility with the original UAS30 was a critical factor throughout the whole work, it is necessary to check that the spar can support the loads produced by the new wing. The slightly larger span and consequent increase in the bending moment supported by the spar should be verified. The effective weight of the new wing was also not estimated. For those reasons, structural analysis of the wing should be performed before manufacturing it.

The final performance estimation performed to the three airplanes has a comparison purpose only. Its results, due to the not total accuracy of the aerodynamic data, as well as the simplifications made to the propulsive system features should not be considered as definitive. In order to obtain precise data on the performance of the UAS30 using the new wing solution, flight testing should be performed.

Finally, two different solutions were presented: one utilizing cruise flaps and other not utilizing it. Although the cruise flaps all in all provide improvements in the performance of the airplane, using the wing without flaps already provides good results regarding the mission requirements. A compromise between the cost in production and weight *vs* performance between the two solutions should be made and the best option should be selected.

Bibliography

[1] Agência Lusa, "Incêndios: ministros realçam apoio de "drones" à defesa da floresta e ambiente | TVI24," [Accessed 2020-02-24]. [Online]. Available: https://tvi24.iol.pt/politica/joao-pedro-matos-fernandes/incendios-ministros-realcam-apoio-de-drones-a-defesa-da-floresta-e-ambiente 1

[2] UOL, "Coronavírus: Drones desinfetam ruas no centro de Porto Alegre - 16/04/2020 - UOL Notícias," [Accessed 2020/10/12]. 1

[3] Revista de Imprensa, "Covid-19. Polícias vão vigiar praias com drones – Executive Digest," [Accessed 2020/11/09]. [Online]. Available: https://executivedigest.sapo.pt/covid-19-policias-vao-vigiar-praias-com-drones/ 1

[4] Agência Lusa, "Évora acolhe projeto de nova aeronave do CEiiA e de empresa brasileira – Observador," 2020, [Accessed 2020/11/10]. [Online]. Available: https://observador.pt/2020/09/25/evora-acolhe-projeto-de-nova-aeronave-do-ceiia-e-de-empresa-brasileira/ 2

[5] CEiiA, "CEiiA | Aeronautics - UAS30," [Accessed 2020-10-13]. [Online]. Available: https://www.ceiia.com/aero-uas30 3, 4

[6] D. Raymer, *Aircraft Design: A Conceptual Approach, Sixth Edition*. American Institute of Aeronautics and Astronautics, Inc., 2019. 4, 10, 13, 16, 17, 18, 19, 24, 25, 26, 28, 29

[7] A. Deperrois, "Guidelines for XFLR5: Analysis Of Foils and Wings Operating at Low Reynolds Numbers," pp. 1–72, 2013, accessed 2021-01-20]. [Online]. Available: https://xflr5.sourceforge.net/xflr5 4, 45, 46, 50, 59, 60

[8] M. H. Sadraey, *Aircraft Design: A Systems Engineering Approach*. John Wiley and Sons, 2012. 7, 11, 14, 25, 26, 27, 28, 29

[9] V. de Brederode, *Aerodinâmica Incompressível: Fundamentos*. IST Press, 2014. 7, 8, 10

[10] D. Ma, Y. Zhao, Y. Qiao, and G. Li, "Effects of relative thickness on aerodynamic characteristics of airfoil at a low Reynolds number," *Chinese J. Aeronaut.*, vol. 28, no. 4, pp. 1003–1015, 2015. 9, 10

[11] A. Toussaint, "Effect of changing the mean camber of an airfoil section," National Advisory Comittee for Aeronautics, Tech. Rep., 1924. 10

[12] Selig, Donovan, and Fraser, "Airfoils at Low Speeds," pp. 1–408, 1989. 10, 11

[13] P. B. S. Lissaman, "Low-Reynolds-Number Airfoils," *Annu. Rev. Fluid Mech.*, vol. 15, no. 1, pp. 223–239, jan 1983. 11

[14] M. Drela, "XFOIL: an analysis and design system for low Reynolds number airfoils." *Low Reynolds Number Aerodyn. Proc. Conf., Notre Dame, U.S.a., June 5-7, 1989*, pp. 1–12, 1989. 11, 45, 46

[15] J. D. J. Anderson, *Introduction to Flight - Seventh Edition*. McGraw-Hill Education, 2012. 14

[16] J. M. Selig, Donovan, and Fraser, *Airfoils at Low Speeds*. Stokely, H A, 1989. 15, 16

[17] P. V. Gamboa and M. A. R. Silvestre, "Airfoil optimization with transition curve as objective function," *Adapt. Model. Simul. 2013 - Proc. 6th Int. Conf. Adapt. Model. Simulation, ADMOS 2013*, no. June 2013, pp. 279–290, 2013. 15, 16, 55

[18] K. L. Cook, "The Silent Force Multiplier: The History and Role of UAVs in Warfare," in *IEEE Aerosp. Conf. Proc.* IEEE, 2007, pp. 1–7. 19, 20, 21, 22, 23, 37

[19] N. Ananthkrishnan, "Small-Perturbtion Analysis of Airplane Flight Dynamics," in *Collect. Tech. Pap. - AIAA Atmos. Flight Mech. Conf.*, vol. 1. Reston, Virigina: American Institute of Aeronautics and Astronautics, aug 2004, pp. 643–659. 19

[20] M. V. Cook, *Flight Dynamics Principles*. Elsevier Ltd, 2013. 20, 21

[21] S. Gudmundsson, *General Aviation Aircraft Design: Applied Methods and Procedures*. Elsevier Inc., 2013. 29, 56

[22] C. Cox, A. Gopalarathnam, and C. E. Hall, "Flight Test of Stable Automated Cruise Flap For an Adaptive Wing Aircraft," *J. Aircr.*, vol. 47, no. 4, pp. 1178–1188, jul 2010. 30

[23] G. Akovali, *Handbook of Composite Fabrication*. Smithers Rapra Technology, 2001. 30

[24] NPTEL, "Objectives_ template." [Online]. Available: https://nptel.ac.in/content/storage2/courses/101104010/lecture7/7_2.htm 30

[25] M. H. Sadraey, *Aircraft Performance - An Engineering Approach*. CRC Press, 2017. 31, 32, 33

[26] Official Journal of the European Union, "COMMISSION DELEGATED REGULATION (EU) 2019/945," mar 2019. [Online]. Available: https://eur-lex.europa.eu/eli/reg_del/2019/945/oj 35

[27] V. Prisacariu, "The History and the Evolution of UAV's From the Beginning Till the 70s," Tech. Rep. 35

[28] R. K. Barnhart, S. B. Hottman, D. M. Marshall, and E. Shappee, *Introduction to Unmanned Aircraft Systems*, 2012. 36

[29] F. Haynes, “Queen Bee - Radio-Controlled Target Aircraft of the 1930s | Naval Historical Society of Australia,” 2002. [Online]. Available: https://www.navyhistory.org.au/queen-bee-radio-controlled-target-aircraft-of-the-1930s/ 36

[30] NOVA, “Spies That Fly | DH.82B Queen Bee (UK) | PBS.” [Online]. Available: https://www.pbs.org/wgbh/nova/spiesfly/uavs_05.html 36

[31] J. Meilak, “The V1 Flying Bomb | MiGFlug.com Blog.” [Online]. Available: https://migflug.com/jetflights/the-v1-flying-bomb/ 36

[32] The Editors of Encyclopaedia Britannica, “V-1 missile | military technology | Britannica.” [Online]. Available: https://www.britannica.com/technology/V-1-missile 36

[33] A. Lüdeke, *Weapons of World War II : infantry weapons, unarmored vehicles, armored vehicles, artillery, special weapons, aircraft, ships*. Parragon, 2011. 36

[34] A. O. Outlet, “The History Unmanned Aerial Vehicles, Part 3: The Cold War - Aviation Oil Outlet.” [Online]. Available: https://aviationoiloutlet.com/blog/early-uavs-the-cold-war/ 36

[35] R. Austin, *Unmanned aircraft systems : UAVs design, development and deployment*. Wiley, 2010. 37, 39, 40

[36] G. Singhal, B. Bansod, and L. Mathew, “Unmanned Aerial Vehicle classification , Applications and challenges : A Review,” *Preprint*, no. November, 2018. 40

[37] P. V. Gamboa and M. A. Silvestre, “Airfoil optimization with transition curve as objective function,” *Adapt. Model. Simul. 2013 - Proc. 6th Int. Conf. Adapt. Model. Simulation, ADMOS 2013*, no. February, pp. 279–290, 2013. 45

[38] J. Morgado, R. Vizinho, M. A. Silvestre, and J. C. Páscoa, “XFOIL vs CFD Performance Predictions for High Lift Low Reynolds Number Airfoils,” *Aerosp. Sci. Technol.*, vol. 52, pp. 207–214, may 2016. 46

[39] B. R. Gyles, “Prop Selector,” [Accessed 2020-11-08]. [Online]. Available: http://www.hoppenbrouwer-home.nl/ikarus/software/propselector.htm 47

[40] E. P. Lesley and S. U. (Daniel Guggenheim Aero. Lab., “Propeller Tests to Determine the Effect of Number of Blades at Two Typical Solidities,” Tech. Rep., 1939. 47

[41] L. C. Dantas, L. E. Miranda, and J. Rodrigues, “Configurações e Dimensionamento da Empenagem.” 48, 49

[42] P. V. Gamboa and M. A. Silvestre, “Introdução ao Avião e Disciplinas de Projecto,” in *Apontamentos DAC*. Universidade da Beira Interior, 2012. 50

[43] UIUC Applied Aerodynamics Group, “UIUC Airfoil Data Site,” [Accessed 2020-03-30]. [Online]. Available: https://m-selig.ae.illinois.edu/ads/coord_database.html 51

[44] N. K. Hieu and H. T. Loc, “Airfoil Selection for Fixed Wing of Small Unmanned Aerial Vehicles,” *Lect. Notes Electr. Eng.*, vol. 371, pp. 881–890, 2016. 52, 53

[45] I. Rodriguez-Eguia, I. Errasti, U. Fernandez-Gamiz, J. M. Blanco, E. Zulueta, and A. Saenz-Aguirre, “A Parametric Study of Trailing Edge Flap Implementation on Three Different Airfoils Through an Artificial Neuronal Network,” *Symmetry (Basel).*, vol. 12, no. 5, p. 828, 2020. 56

[46] J. Roskam, “Roskam - Methods for Estimation Drag Polars of Subsonic Airplanes,” 1971. 59, 60

[47] E. Torenbeek, “Appendix A: Volumes, Surface and Wetted Areas,” in *Adv. Aircr. Des.* Oxford, UK: John Wiley & Sons, Ltd, may 2013, pp. 393–396. [Online]. Available: http://doi.wiley.com/10.1002/9781118568101.app1 60

[48] D. Aircraft, “DA-50 – Desert Aircraft.” [Online]. Available: https://www.desertaircraft.com/products/da-50r 67

[49] C. Engineering, “Corvid-50 Engine.” [Online]. Available: https://www.currawongeng.com/uav-engines/corvid-50/ 67, 124, 125

[50] A. International, “Biela Propellers.” [Online]. Available: https://www.aircraftinternational.com/Products/Propellers/BielaPropellers.aspx 68

[51] Toni Clark, “Desert Aircraft DA-50R,” [Accessed 2020-11-19. [Online]. Available: https://toni-clark-shop.com/Desert-Aircraft-DA-50R_1 123

Appendix A

Propulsive System

A.1 DA-50R Specifications

Figure A.1: DA-50R Engine [51].

Table A.1: DA-50R engine specifications [51].

Displacement	50 cc	
Bore X Stroke	42.6 x 35 mm	
Mass	1.47 kg	
Power Output	3.73 kW	
RPM Range	1200 RPM - 7500 RPM	
Propellers	2-Blade	22x10”, 23x10”, 24x8”, 22x12”, 24x10” , 23x12”
	3-Blade	21x12”

A.2 CORVID-50 Specifications

Figure A.2: Corvid-50 engine [49].

Table A.2: Corvid-50 engine specifications [49].

Displacement	50 cc
Mass	3.86 kg
Power Output	2.8 kW at 7000 RPM
Fuel Consumption	500 g/kW-hr at 6000 RPM & 40 % throttle

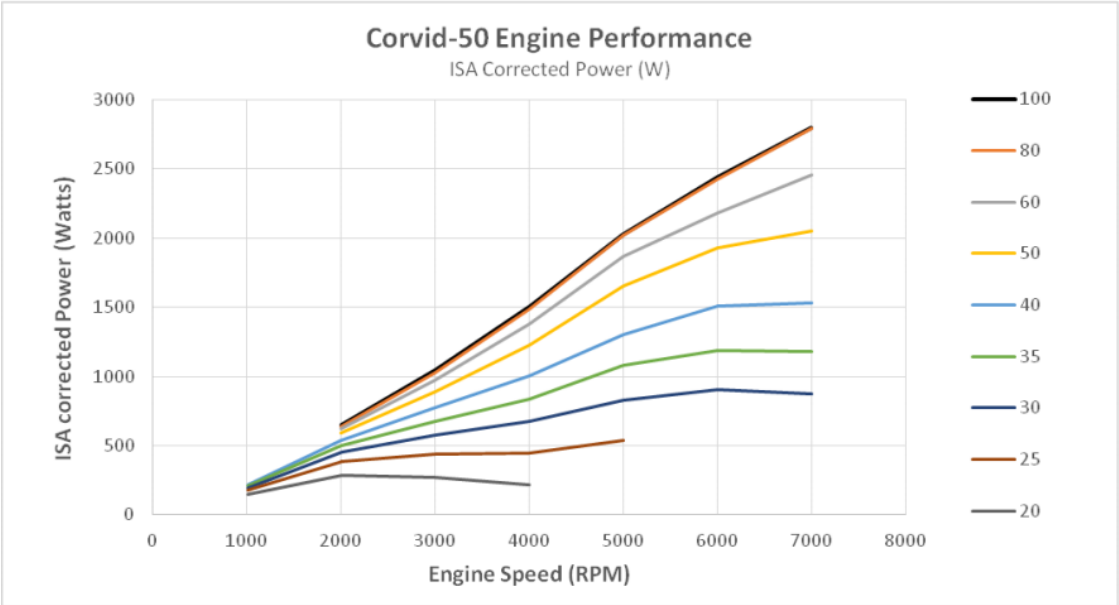

Figure A.3: P_o *vs* N curves of the Corvid-50 engine [49].

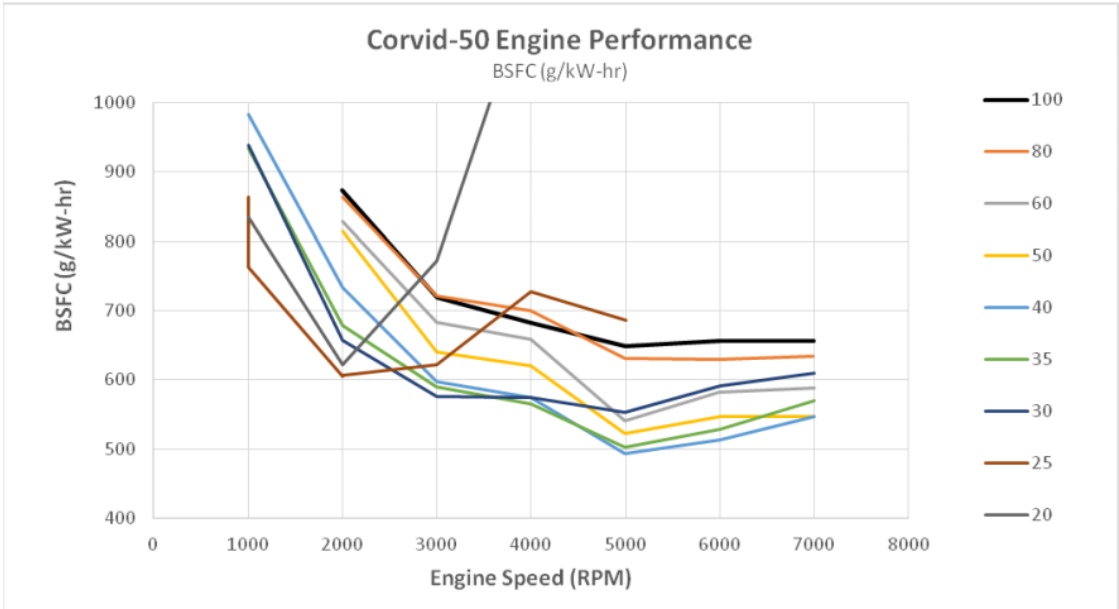

Figure A.4: SFC *vs* N curves of the Corvid-50 engine [49].

A.3 Propulsive System Model

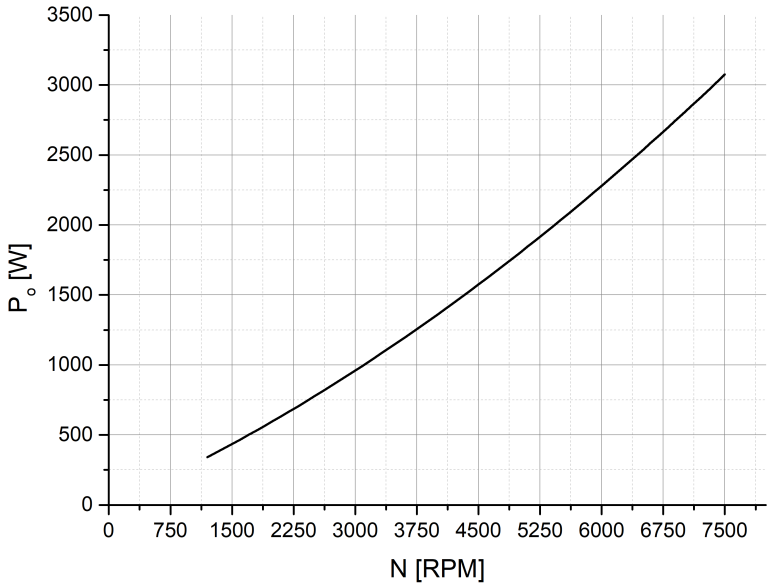

Figure A.5: P_o *vs* N curves of the obtained engine model.

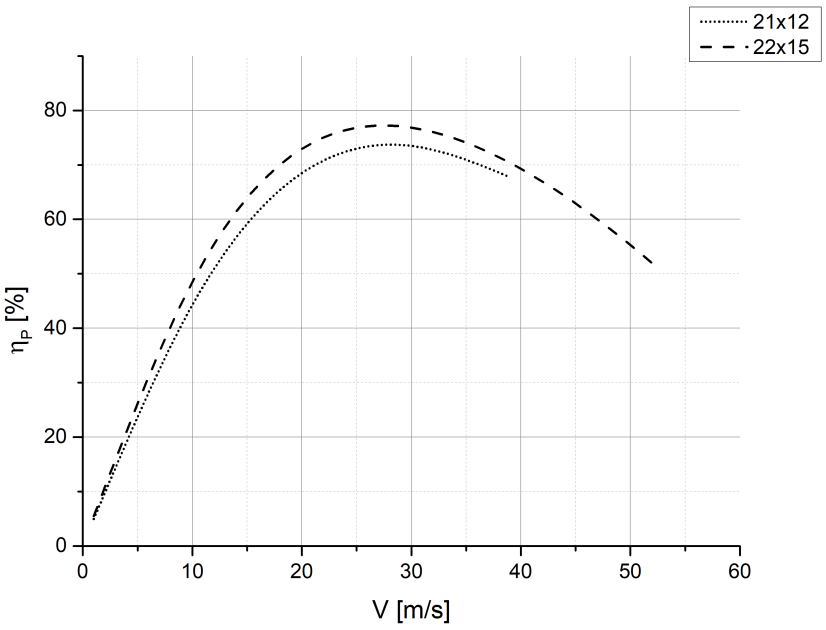

Figure A.6: η_P *vs* V curves of the propulsive system model for the two used propellers.

Appendix B

Flap Deflection Envelopes

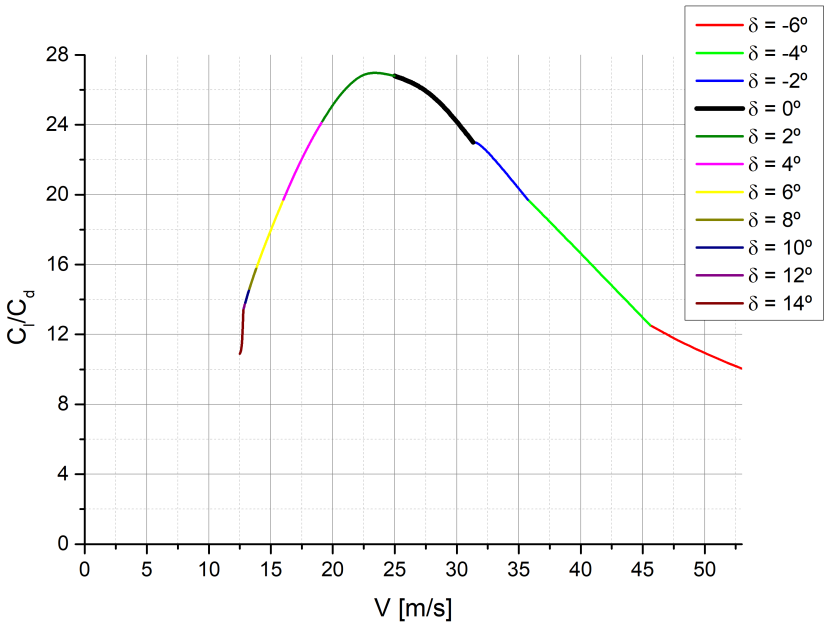

Figure B.1: C_L/C_D *vs* V flap deflection envelope.

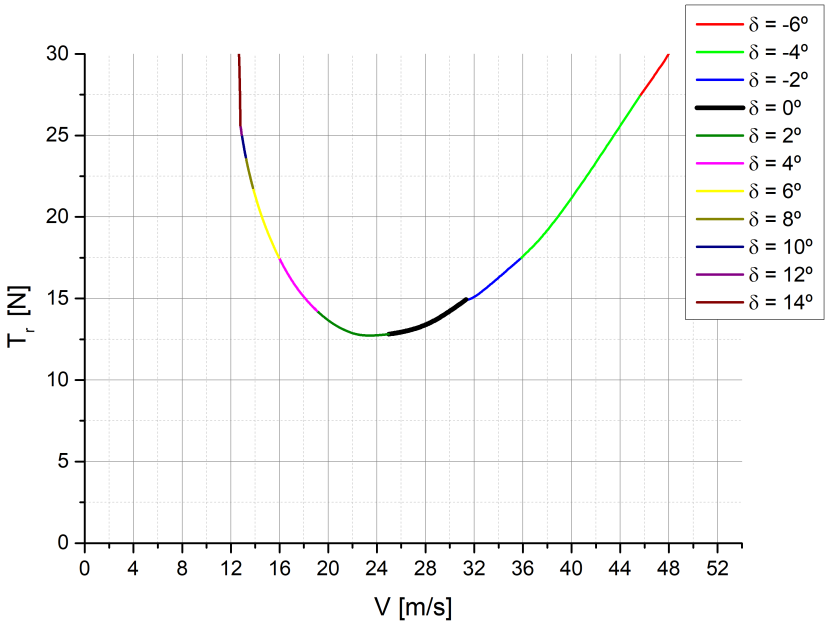

Figure B.2: T_r *vs* V flap deflection envelope.

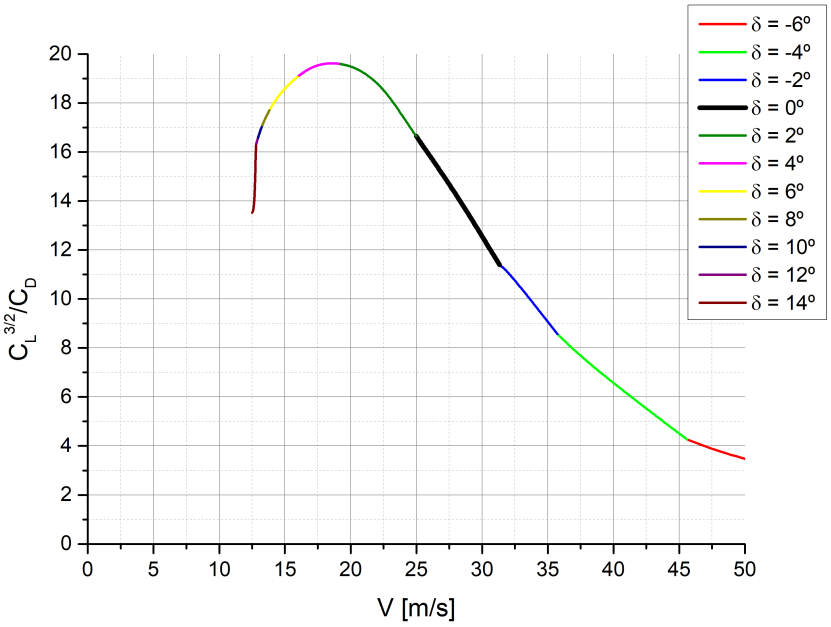

Figure B.3: ${C_L^{3/2}}/{C_D}$ *vs* V flap deflection envelope.

Appendix C

CAD Geometries

C.1 Wing Geometry

Figure C.1: New wing design geometry: Top view.

Figure C.2: New wing design geometry: Side view.

Figure C.3: New wing design geometry: Front view.

C.2 Installed Wing Comparison

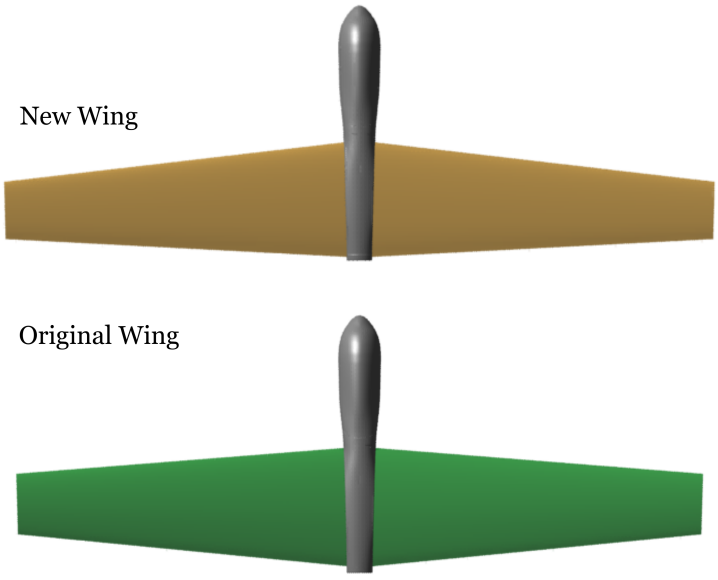

Figure C.4: Comparison of the two wing designs (UAS30 original and new) in the UAS30 fuselage: Top view.

New Wing

Original Wing

Figure C.5: Comparison of the two wing designs (UAS30 original and new) in the UAS30 fuselage: Side view.

New Wing

Original Wing

Figure C.6: Comparison of the two wing designs (UAS30 original and new) in the UAS30 fuselage: Front view.